Albert-Ludwigs-Universität Freiburg

Master Thesis

Vibrational instabilities caused by current-induced forces in molecular junctions: A semi-classical approach

Author:
Luisa Robin Grether

Supervisor:
Prof. Dr. Michael Thoss

In cooperation with:
Dr. Samuel Rudge

A thesis submitted in partial fulfillment of the requirements for the degree

Master of Science

Fakultät für Mathematik und Physik
Physikalisches Institut
Lehrstuhl für theoretische Physik kondensierter Materie
July 3, 2023 – reprinted April 3, 2026

universität freiburg

Abstract

In this thesis, we study electron transport through molecular junctions with both weak and strong electronic-vibrational coupling, utilizing the Born-Markov master equation, and the semi-classical theory of electronic friction to describe a low-frequency vibrational mode.

Using the Holstein model, which comprises a junction of one electronic level coupled to a harmonic vibrational mode, we determine in which parameter regimes the semi-classical method is applicable. We find that the semi-classical approach is accurate if the natural frequency of the vibrational mode is smaller than the coupling of the junction to the electrodes, and also if they are on the same order of magnitude, given that the electronic-vibrational coupling is small. We also find that the semi-classical method is usually less computationally expensive in these regimes, rendering this the optimal domain for its application.

Using the semi-classical method, we investigate the so-called *one-level two-mode model*, an extension of the Holstein model that adds a second high-frequency vibrational mode. The high-frequency vibration is treated quantum-mechanically alongside the electronic dynamics. For strong electronic-vibrational coupling of the high-frequency mode, we find that adding the second vibration exerts a strongly stabilizing effect on the low-frequency mode. This stabilization works because the electronic-vibrational coupling of the high-frequency mode is much greater than that of the low-frequency mode, which leads to a very uneven distribution of the energy dissipated in the junction, strongly favoring the excitation of the high-frequency mode. With increasing voltage, the stabilization becomes periodically weaker and stronger as new channels of electron transport through the junction become accessible, giving rise to negative differential excitation of the low-frequency mode. If the electronic-vibrational coupling of the high-frequency mode is weak, we find that the additional high-frequency method can either exert a stabilizing or destabilizing effect on the low-frequency vibration depending on its coupling. The observed stabilization is much weaker than in the strong-coupling regime, and only relevant in a small voltage range.

Acknowledgements

First and foremost, I want to thank my supervisor, *Michael Thoss*. Throughout my six years of studying physics in Freiburg, I had the opportunity to visit three of your lectures, and I enjoyed every one of them. I felt very honored when you invited me to write my Master thesis in your group, and I am delighted that I decided so.

Second, I want to thank *Samuel Rudge*. You introduced me to the topic of my thesis. You were the origin of most research pathways in this work. I am very thankful for all the comprehensive advice you gave me, all the fruitful discussions we had, and all your guidance through this one-year project. Without your never-ending support, this thesis would have never been accomplished.

Furthermore, I want to thank *Sebastian Stumper* and *Miriam Büttner*, who were the best office colleagues I could wish for, and were always helpful if I had any questions both in and outside of physics.

I also want to thank *Jakob Bätge* and *Martin Mäck* for providing me with the necessary caffeine to keep my concentration levels high. I want to thank *Christoph Kaspar*, *Rudolf Smorka*, and *Riley Preston* for all the assistance and advice you gave me whenever Sam was not available. And I want to thank the entire group for providing such an excellent working environment. You are all doing great research, and I am very proud to have been a part of it.

I further want to thank a few people who guided me along my studies. First, I want to thank *Prof. Fischer*. On my first day at the Uni Freiburg, while I was still at school, I visited your lecture on the university's open day. This was the moment I decided to study physics. Next, I want to thank *Prof. Buchleitner* and *Felix Thiel*, who guided me through my Bachelor thesis, and thus contributed a lot to my education as a scientist. And I want to thank my fellow students, *Marvin Schmoll*, *Fabian Lex*, and *Paul Weizel*, who began their studies together with me in 2017, have been a great support ever since, and enriched my period of study with plenty of humorous discussions.

Not least, I want to thank my family for your never-ending care and encouragement. Even after I moved to Freiburg, your incredible support has still been foundational to my success.

Many numerical data in this work have been obtained using the *bwForCluster Justus 2*. Therefore, I acknowledge support from the state of Baden-Württemberg through bwHPC and the Deutsche Forschungsgemeinschaft (DFG) through grant no INST 40/575-1 FUGG.

Throughout my six-year study period, I have received financial support under the German Federal Training Assistance Act (BAföG). Therefore, I kindly acknowledge the financial support from the *Bundesrepublik Deutschland*.

Contents

Units, symbols and acronyms

The following table lists the units, physical and mathematical symbols, and acronyms that are used in this thesis.

Symbol and definition	Explanation
Units	
eV	Electron volt, unit of energy.
s	Second, unit of time.
A	Ampere, unit of electric current.
K	Kelvin, unit of thermodynamic temperature.
Physical constants	
$h = 4.135\,667\,696 \cdot 10^{-15}\,\mathrm{eV} \cdot \mathrm{s}$	Planck constant.
$\hbar = \frac{h}{2\pi} = 6.582\,119\,569 \cdot 10^{-16}\,\mathrm{eV} \cdot \mathrm{s}$	Reduced Planck constant.
$\mathrm{e} = 1.602\,176\,634 \cdot 10^{-19}\,\mathrm{A} \cdot \mathrm{s}$	Electron charge.
$k_\mathrm{B} = 8.617\,333\,262 \cdot 10^{-5}\,\mathrm{eV/K}$	Boltzmann constant.
Mathematical constants	
$\mathrm{i} = \sqrt{-1}$	Imaginary unit.
$\pi = 3.141\,592\,653...$	Pi.
$e = 2.718\,281\,828...$	Euler's number.
Mathematical symbols	
$\mathrm{tr}\{A\}$	Trace of an operator A.
$\mathrm{tr}_{\mathrm{S/B}}\{A\}$	Partial trace of A over the nanosystem or the bath.
$[A, B] = AB - BA$	Commutator of two operators, A and B.
$\{A, B\} = AB + BA$	Anticommutator of two operators, A and B.
$\otimes$	Tensor product, also called Kronecker direct product.
δ_{ij}, $\delta(x)$	Kronecker delta, Dirac δ-function.
x^*	Complex conjugate of x.
$A^\dagger$	Hermitian conjugate of an operator A.
$\mathrm{Re}\{x\}$, $\mathrm{Im}\{x\}$	Real and imaginary part of a complex number x.
p.v. $\int$	Cauchy principal value integral.
Acronyms	
BMME	Born-Markov master equation.
HEOM	Hierarchical equations of motion.
NEGF	Non-equilibrium Green's function.
RLM	Resonant level model.
1L2M model	One-level two-mode model.

Chapter 1

Introduction

"I think there is a world market for about five computers."—This famous phrase is often attributed to former CEO of IBM, Thomas J. Watson [1, 2]. Although there have long been severe doubts about this attribution [3], and the quote may never have been pronounced in this way, it nevertheless conveys an important message: In the early days of the development of electronic calculation machines, today we call them computers, no one could have foreseen the enormous achievements that would be accomplished in just a few decades. Machines that once filled entire halls now fit comfortably in a pocket and, at the same time, have become orders of magnitude more powerful and energy efficient. Much of this development is due to the decades-long miniaturization of electronic components, most notably transistors, which is often expressed in the famous Moore's law, forecasting a doubling of the number of transistors in integrated circuits about every two years [4, 5]. But it was clear from the beginning that this miniaturization has natural limits, which have slowed the advancement of microprocessors in recent years. The transistors and conductors in state-of-the-art microprocessors are now only a few atoms wide. With the size of the conductors approaching the de Broglie wavelength of the electrons, the limits of classical physics have been reached; further miniaturization would inevitably require incorporating quantum effects [6].

For the leap into the quantum domain, von Hippel proposed the development of so-called *molecular electronics* as early as 1956 [7], and after Aviram and Ratner described a molecular rectifier circuit in their well-known 1974 paper [8], molecular electronics became a thriving field of research in physics and chemistry. The basic principle is to construct atomic or molecular structures whose intrinsic electromechanical properties mimic the functioning of classical components, such as diodes and transistors, by exploiting quantum effects such as interference and quantization.

Aviram and Ratner initially proposed a rectifier circuit based on an organic molecule that resembles the p-n junction of a solid-state diode, which was indeed realized experimentally in the late 1990s [9, 10]. In the meantime, several novel methods [11] were developed to manipulate single molecules and atoms, such as the scanning tunneling microscope [12], the atomic force microscope, and the mechanically controlled break junction technique, which was utilized for the realization of Aviram's and Ratner's rectifier. These allowed the experimental realization of single-molecule junctions [13, 14] and atomic chain junctions [15–17] for the first time. In the early 2000s, a variety of phenomena for such single-molecule junctions were theoretically described and experimentally observed, including conductance switching [18, 19], negative differential resistance [20], and the aforementioned rectification [9, 10, 21], which could be used

to mimic the operation of classical solid-state semiconductor components. In addition, entirely new mechanisms have been identified, such as electron spin for use as memory in spintronics [22], and several sensitive properties [23, 24], which could be exploited for measurement devices. Despite these advancements, the practical application of molecular electronic devices remains challenging. Effects such as electronic-vibrational coupling and mechanical instability of the molecules make the prediction and realization of entire circuits difficult.

In molecular junctions, an electric current can cause high excitation of nuclear vibrations via electronic-vibrational coupling, thereby leading to an instability of the junction. Mechanisms underlying the high vibrational excitation include both Joule heating [25] but also more intricate processes, such as the emergence of non-conservative forces [26] and negative friction [27] acting on the vibrations. Understanding these mechanisms is challenging because the theoretical description of charge transport through a molecular junction represents a highly non-trivial non-equilibrium many-body problem. A crucial challenge is the coupling of the molecular structure to macroscopic electrodes. A complete microscopic description of the whole system is thus no longer possible since the electrodes have too many degrees of freedom.

In weakly correlated systems, where transport through the junction effectively involves only a single charge carrier at a time, one can use scattering theory or alternatively non-equilibrium Green's functions (NEGFs) to describe the dynamics of the junction [28]. When electron-electron interactions become relevant, however, or additionally strong electronic-vibrational coupling is considered, with substantial energy transfers occurring between the charge carriers and the degrees of freedom inside the junction, the use of other methods is required [29, 30]. For the treatment of such strongly correlated transport problems with strong electronic-vibrational coupling, master equation approaches are the method of choice. These use statistical quantum mechanics by approximating the electrodes as heat baths and electron reservoirs, respectively, making the molecular nanosystem an open quantum system [31]. Various master equation approaches have been derived, including the approximate Born-Markov master equation (BMME) and the numerically exact hierarchical equations of motion (HEOM) [32, 33]. Such master equations are powerful tools as they allow the description of strongly correlated transport problems with strong electronic-vibrational coupling, and can accurately predict advanced effects such as damping through electron-hole pair creation.

Treating nanosystems that require a large vibrational basis with master equation approaches is very expensive, though. This is, however, precisely what is required to study vibrational instabilities. To circumvent this problem, semi-classical approaches can be used in some cases. Vibrational modes in molecular nanosystems are typically stretching and bending vibrations of single atoms, or pairs or groups of a few atoms. The reduced mass of the vibrating system is, therefore, usually several orders of magnitude large than the electron mass. This mass-scale separation often gives rise to a time-scale separation between the slow vibrational dynamics and the fast electron transport, which allows a semi-classical treatment of the slow vibrational degrees of freedom. A variety of different semi-classical methods can be found in literature, including Ehrenfest dynamics [34, 35], surface hopping [36], and quantum-classical Liouville equations [37]. In the following, we use the theory of electronic friction [30, 38–40]. Electronic friction is an advanced semi-classical approach because it takes into account not only an adiabatic mean force induced by the electron transport on the vibrations, but also two additional terms: a stochastic force and the eponymous electronic friction

force [39], which represent a first-order feedback of the vibrational dynamics to the electron flow. The derivation of electronic friction uses a partial Wigner transform with respect to the slow vibrational degrees of freedom applied to the reduced density matrix of the nanosystem [30, 37, 39]. Together with the aforementioned time-scale separation, an approximate classical Langevin equation follows for the dynamics of the vibrational modes, including the mentioned adiabatic mean force, electronic friction, and stochastic force. For the treatment of the remaining electronic degrees of freedom and, if necessary, additional high-frequency vibrational modes, the master equation approaches mentioned above can be used. Due to the semi-classical description of the slow vibrational modes, the dimensionality of the remaining quantum-mechanical degrees of freedom is substantially reduced, allowing the consideration of multiple vibrational modes.

In the following thesis, we will study vibrational instabilities in molecular junctions, focusing on how they are enhanced or reduced by the interplay of multiple molecular vibrational modes. To this end, we will derive the Born-Markov master equation and the corresponding semi-classical electronic friction for the molecular junction. While the use of the Born-Markov master equation comes with the restriction to weak coupling between the nanosystem and the electrodes, it does not otherwise impose any constraints on the coupling strengths within the nanosystem, and it is generally much less expensive to solve than the hierarchical equations of motion for the same model. Using the well-known Holstein model [41], which comprises a junction with one electronic level and one vibrational mode, we will investigate how accurate the semi-classical approach is, and for which parameters of the junction it is beneficial to use. After this, we will consider a novel system, a junction with one electronic level and two vibrational modes [27], which we call the one-level two-mode model (1L2M model). We specifically consider one high-frequency mode and one low-frequency mode. This requires the employment of a new technique, combining the semi-classical treatment of the low-frequency mode with a fully quantum description of the high-frequency mode alongside the electronic dynamics. Our central goal is to examine the transport characteristics of the one-level two-mode model and find out how the additional high-frequency mode affects the vibrational stability of the junction compared to the Holstein model.

The thesis is organized as follows. In Chapter 2, we define our model of a molecular junction and introduce all theoretical methods used. Specifically, we derive the Born-Markov master equation for the model in Sec. 2.2 and show a few purely quantum-mechanical example calculations in Sec. 2.3. In the following Sec. 2.4, we demonstrate the detailed derivation of the electronic friction and the Langevin equation for the slow vibrational degrees of freedom. In Chapter 3, we thoroughly investigate the Holstein model both using the purely quantum Born-Markov master equation as well as the semi-classical approach. Using this system, we illustrate our methodology and determine in which cases the approximations made by the Born-Markov master equation and the semi-classical electronic friction give physically meaningful results. Finally, in Chapter 4, we apply our acquired knowledge to the one-level two-mode model (1L2M model), with one low-frequency mode and one high-frequency mode. Throughout the study, we treat the low-frequency mode semi-classically and compare how its stability is affected by the interaction with the high-frequency mode compared to the Holstein model. In conclusion, Chapter 5 summarizes the entire work and provides an outlook for future research.

Chapter 2

Model and Methodology

In this chapter, we define our model of a molecular junction and outline all the theoretical methods that will be used to calculate the transport characteristics and vibrational dynamics of the junction. We begin in Sec. 2.1 by defining our model. In Sec. 2.2, we derive the Born-Markov master equation for it and discuss the validity of the underlying Born-Markov approximation. Then, we look at two well-known examples of a molecular junction in Sec. 2.3: the resonant level model and the Anderson impurity model. In Sec. 2.4, we present the derivation of the semi-classical electronic friction approach within our Born-Markov master equation framework, and we outline how we use the semi-classical method to calculate the transport characteristics of a molecular junction.

2.1 Model

In this thesis, we study the flow of an electric current through a molecular junction and its induced mechanical effects on the vibrational modes of the molecule. Fig. 2.1 shows a schematic representation of our model.

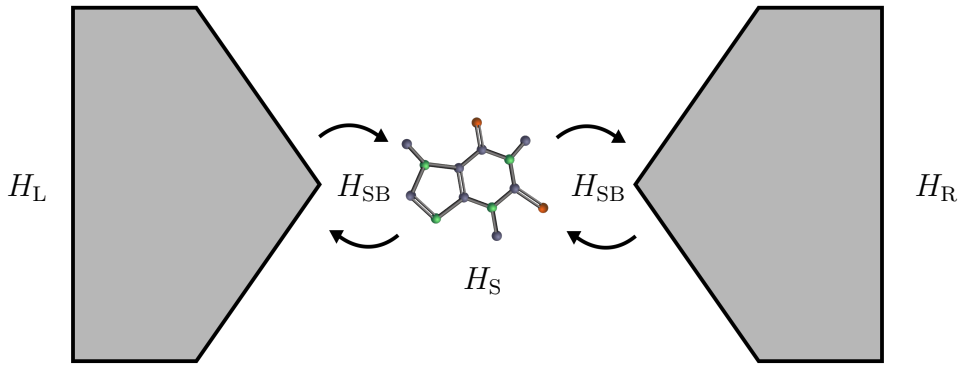

Figure 2.1: Schematic illustration of a molecular junction. The illustration of the caffeine molecule in the center is adapted from [42].

The center of our model is a molecule or a similar nanosystem, such as a chain of atoms, represented by the system Hamiltonian H_{S}. The nanosystem comprises molecular electronic orbitals, which we model as a series of *electronic levels*. When electron spin is neglected, each electronic level is a two-state system, with the two

states occupied or charged and unoccupied or neutral, respectively. Mathematically, we describe the electronic level by fermionic creation and annihilation operators, $d^\dagger$ and d, and the respective Fock basis states, charged $|1\rangle$ and neutral $|0\rangle$, with the following properties,

$$\begin{aligned} d^\dagger |0\rangle &= |1\rangle\,, & d\,|1\rangle &= |0\rangle\,, \\ d^\dagger d\,|1\rangle &= |1\rangle\,, & d^\dagger d\,|0\rangle &= 0. \end{aligned} \tag{2.1}$$

To incorporate electron spin, separate operators of the form $d_\uparrow^{(\dagger)}$ and $d_\downarrow^{(\dagger)}$ are used for the two spin orientations. We will discuss this in more detail later in Sec. 2.3.2. The degrees of freedom of the atomic nuclei and bonds are modeled in terms of their eigenmodes of vibration. Mathematically, we describe them by bosonic creation and annihilation operators, $a^\dagger$ and a, and the respective Fock basis states, $|n\rangle$ for $n \in \mathbb{N}$, with

$$\begin{aligned} a^\dagger |n\rangle &= \sqrt{n+1}\,|n+1\rangle\,, & a\,|n\rangle &= \sqrt{n}\,|n-1\rangle\,, \\ \underbrace{a^\dagger a}_{=:N}\,|n\rangle &= n\,|n\rangle\,, & |n\rangle &= \frac{1}{\sqrt{n!}}(a^\dagger)^n\,|0\rangle\,. \end{aligned} \tag{2.2}$$

For convenience, we may later also switch to the description using displacement and momentum operators, $\hat{x}$ and $\hat{p}$, given as

$$\hat{x} = \sqrt{\frac{\hbar}{2m\omega}}\left(a^\dagger + a\right), \qquad \hat{p} = \mathrm{i}\sqrt{\frac{\hbar m\omega}{2}}\left(a^\dagger - a\right), \tag{2.3}$$

where m and ω are the reduced mass and natural frequency of the eigenmode. We do not initially assume any particular form of the system Hamiltonian; any interactions between the electronic and vibrational degrees of freedom are possible,

$$H_\mathrm{S} = f(d_1^\dagger, d_1, ..., a_1^\dagger, a_1, ...). \tag{2.4}$$

To allow for the flow of an electric current through the nanosystem, it is coupled to a left and a right electrode represented by the Hamiltonians H_L and H_R. We model the electrodes as reservoirs of non-interacting electronic levels described by fermionic creation and annihilation operators, $c_k^\dagger$ and c_k,

$$H_\mathrm{L} = \sum_{k_\mathrm{L}} \varepsilon_{k_\mathrm{L}} c_{k_\mathrm{L}}^\dagger c_{k_\mathrm{L}}, \qquad H_\mathrm{R} = \sum_{k_\mathrm{R}} \varepsilon_{k_\mathrm{R}} c_{k_\mathrm{R}}^\dagger c_{k_\mathrm{R}}, \tag{2.5}$$

and the corresponding Fock basis states, with properties similar to Eq. (2.1),

$$\begin{aligned} c_{k_K}^\dagger\,|..., 0_{k_K}, ...\rangle &= |..., 1_{k_K}, ...\rangle\,, & c_{k_K}\,|..., 1_{k_K}, ...\rangle &= |..., 0_{k_K}, ...\rangle\,, \\ c_{k_K}^\dagger c_{k_K}\,|..., 1_{k_K}, ...\rangle &= |..., 1_{k_K}, ...\rangle\,, & c_{k_K}^\dagger c_{k_K}\,|..., 0_{k_K}, ...\rangle &= 0. \end{aligned}$$

We abbreviate the electrode Hamiltonians as one single bath Hamiltonian H_B,

$$H_\mathrm{B} = H_\mathrm{L} + H_\mathrm{R} = \sum_{K\in\{\mathrm{L},\mathrm{R}\}} \sum_{k_K} \varepsilon_{k_K} c_{k_K}^\dagger c_{k_K}. \tag{2.6}$$

The coupling, H_SB, between the electrodes and the nanosystem is modeled as bilinear electron exchange terms,

$$H_\mathrm{SB} = \sum_i \sum_{K\in\{\mathrm{L},\mathrm{R}\}} \sum_{k_K} \left(V_{i,k_K} c_{k_K}^\dagger d_i + V_{i,k_K}^* d_i^\dagger c_{k_K}\right). \tag{2.7}$$

In practice, we will usually not indicate the coupling strengths, V_{i,k_K}, but the electrode coupling functions, $\Gamma^K_{ij}(\omega)$, defined as

$$\Gamma^K_{ij}(\omega) = 2\pi \sum_{k_K} V_{i,k_K} V^*_{j,k_K} \delta(\varepsilon_{k_K} - \hbar\omega). \tag{2.8}$$

In principle, $\Gamma^K_{ij}(\omega)$ may vary for different ω, though from the end of Sec. 2.2.1, we will always work in the *wideband limit*, where $\Gamma^K_{ij}(\omega) = \Gamma^K_{ij}$ is independent of ω. For brevity, we group together all electrode terms that couple to the same nanosystem operator $d_i^{(\dagger)}$. Here, we have to pay attention to the anticommutation of the fermionic creation and annihilation operators,

$$\begin{aligned} H_{\mathrm{SB}} &= \sum_i \sum_{K\in\{\mathrm{L,R}\}} \sum_{k_K} \left(-V_{i,k_K} d_i c^\dagger_{k_K} + V^*_{i,k_K} d_i^\dagger c_{k_K} \right) \\ &= \sum_i \sum_\sigma \zeta^\sigma d_i^\sigma \underbrace{\sum_K \sum_{k_K} V^\sigma_{i,k_K} c^{\bar\sigma}_{k_K}}_{=:B_i^{\bar\sigma}} = \sum_i \sum_\sigma \zeta^\sigma d_i^\sigma B_i^{\bar\sigma}, \end{aligned} \tag{2.9}$$

$$\text{with} \quad \zeta = -1, \quad \zeta^\dagger = 1.$$

From Eq. (2.7), it is easy to see that H_{SB} has no diagonal elements in the combined Fock basis. Together with H_{S} and H_{B}, we now have the total Hamiltonian of our model,

$$H = H_{\mathrm{S}} + H_{\mathrm{B}} + H_{\mathrm{SB}}. \tag{2.10}$$

We assume the coupling between the electrodes and the nanosystem to be weak, such that the state of the electrodes is essentially unaffected by the interaction with the nanosystem. The electrodes can, therefore, be treated as heat baths and electron reservoirs held at local equilibrium with their respective constant temperatures, T_{L} and T_{R}, and fixed chemical potentials, μ_{L} and μ_{R}, respectively. With the respective number operators, $N_K = \sum_{k_K} c^\dagger_{k_K} c_{k_K}$, the bath density operator, ρ^0_{B}, is defined as a product of Gibbs states,

$$\rho^0_{\mathrm{B}} := \frac{e^{(H_{\mathrm{L}} - \mu_{\mathrm{L}} N_{\mathrm{L}})/k_{\mathrm{B}} T_{\mathrm{L}}}}{\mathrm{tr}_{\mathrm{B}} \left\{ e^{(H_{\mathrm{L}} - \mu_{\mathrm{L}} N_{\mathrm{L}})/k_{\mathrm{B}} T_{\mathrm{L}}} \right\}} \otimes \frac{e^{(H_{\mathrm{R}} - \mu_{\mathrm{R}} N_{\mathrm{R}})/k_{\mathrm{B}} T_{\mathrm{R}}}}{\mathrm{tr}_{\mathrm{B}} \left\{ e^{(H_{\mathrm{R}} - \mu_{\mathrm{R}} N_{\mathrm{R}})/k_{\mathrm{B}} T_{\mathrm{R}}} \right\}}, \tag{2.11}$$

where k_{B} is the Boltzmann constant. As both $H_{\mathrm{L/R}}$ and $N_{\mathrm{L/R}}$ are diagonal in the Fock basis defined above, the bath density operator is also diagonal in the Fock basis. By varying the chemical potentials, an external voltage, $\Phi = (\mu_{\mathrm{L}} - \mu_{\mathrm{R}})/\mathrm{e}$, can be applied to the model system to drive it out of equilibrium and excite a non-zero net electric current. In the following, we always apply a symmetrical potential difference between the electrodes, and we set the Fermi levels to zero, such that we always have

$$\mu_{\mathrm{L}} = \frac{\mathrm{e}\Phi}{2}, \qquad \mu_{\mathrm{R}} = -\frac{\mathrm{e}\Phi}{2}. \tag{2.12}$$

The sign of Φ is chosen so that $\Phi > 0$ naturally causes a flow of electrons from the left to the right electrode. As usual in this field of physics, we define the direction of current in the direction of electron flow. Hence, $\Phi > 0$ usually corresponds to a positive electric current.

Now that we have defined our model, in the next section, we will derive a master equation to describe its time evolution.

2.2 Quantum theory: Born-Markov master equation

In this section, we derive a Born-Markov master equation (BMME) for the model system defined in Sec. 2.1. The starting point for calculating the dynamics of our model is the von Neumann equation [43],

$$\frac{\mathrm{d}}{\mathrm{d}t}\rho(t) = -\frac{\mathrm{i}}{\hbar}\left[H, \rho(t)\right], \tag{2.13}$$

which connects the model's current state, described by the density operator $\rho(t)$, to its time derivative. In our further considerations, we are only interested in the dynamics of the nanosystem, which, from now on, we will refer to as the *system*. Our goal is, therefore, to trace out the degrees of freedom of the electrodes and to find a closed equation of motion for the reduced dynamics of the system, described by the reduced density operator, $\rho_\mathrm{S}(t) = \mathrm{tr}_\mathrm{B}\{\rho(t)\}$, such that

$$\frac{\mathrm{d}}{\mathrm{d}t}\rho_\mathrm{S}(t) = \mathrm{tr}_\mathrm{B}\left\{\frac{\mathrm{d}}{\mathrm{d}t}\rho(t)\right\} \overset{(2.13)}{=} -\frac{\mathrm{i}}{\hbar}\,\mathrm{tr}_\mathrm{B}\left[H, \rho(t)\right] \overset{?}{=} f(\rho_\mathrm{S}(t)) \tag{2.14}$$

for some function f. This function is called the *generator* of the *dynamical map* that maps $\rho_\mathrm{S}(t_0) \to \rho_\mathrm{S}(t)$ for $t \geq t_0$. However, finding such a generator and its associated dynamical map is highly non-trivial. The definitional requirements for $\rho_\mathrm{S}(t)$ are a particular challenge. As for any density operator, we require its diagonal values in any basis to satisfy $(\rho_\mathrm{S})_{ii} \geq 0$, and we assume normalization, $\mathrm{tr}_\mathrm{S}\{\rho_\mathrm{S}(t)\} = 1$. These requirements for $\rho_\mathrm{S}(t)$ put the additional constraints of complete positivity and trace preservation on the sought dynamical map and its generator [31].

The theory of open quantum systems provides various options to find such a closed equation of motion. In this work, we use the Born-Markov approximation to derive an approximate Born-Markov master equation for our model.

2.2.1 Derivation

In the following, we derive a general Born-Markov master equation (BMME) for our model, making no assumptions other than those from Sec. 2.1. We mainly follow the derivation given on pp. 126-131 of [31]. Our starting point is the von Neumann equation for the entire model, introduced in Eq. (2.13).

We start by transforming to the interaction picture, regarding H_SB as the perturbation. In the interaction picture, the total model is described by a different density operator, $\rho_\mathrm{I}(t)$, given by [43]

$$\rho_\mathrm{I}(t) = e^{\mathrm{i}(H_\mathrm{S}+H_\mathrm{B})t/\hbar}\rho(t)e^{-\mathrm{i}(H_\mathrm{S}+H_\mathrm{B})t/\hbar}.$$

For this density operator, the von Neumann equation takes the form

$$\frac{\mathrm{d}}{\mathrm{d}t}\rho_\mathrm{I}(t) = -\frac{\mathrm{i}}{\hbar}\left[H_\mathrm{SB,I}(t), \rho_\mathrm{I}(t)\right], \tag{2.15}$$

where the transformed coupling Hamiltonian is given by

$$H_\mathrm{SB,I}(t) = e^{\mathrm{i}(H_\mathrm{S}+H_\mathrm{B})t/\hbar}H_\mathrm{SB}e^{-\mathrm{i}(H_\mathrm{S}+H_\mathrm{B})t/\hbar}.$$

We formally integrate Eq. (2.15) to obtain

$$\rho_{\mathrm{I}}(t) = \rho_{\mathrm{I}}(t_0) - \frac{\mathrm{i}}{\hbar}\int_{t_0}^{t} \mathrm{d}t' \left[H_{\mathrm{SB,I}}(t'), \rho_{\mathrm{I}}(t')\right],$$

and insert the formal solution back into Eq. (2.15),

$$\frac{\mathrm{d}}{\mathrm{d}t}\rho_{\mathrm{I}}(t) = -\frac{\mathrm{i}}{\hbar}\left[H_{\mathrm{SB,I}}(t), \rho_{\mathrm{I}}(t_0)\right] - \frac{1}{\hbar^2}\int_{t_0}^{t} \mathrm{d}t' \left[H_{\mathrm{SB,I}}(t), \left[H_{\mathrm{SB,I}}(t'), \rho_{\mathrm{I}}(t')\right]\right].$$

As mentioned in Sec. 2.1, we assume that the coupling between the electrodes and the nanosystem is weak, such that the interaction with the nanosystem does not significantly influence the state of the electrodes. Therefore, the electrodes always reside in their respective local equilibrium states, so no memory effects occur, and no coherence is built up between the system and the electrodes. Mathematically, this means that the state of the entire model factors at each time point as $\rho_{\mathrm{I}}(t) \approx \rho_{\mathrm{S,I}}(t) \otimes \rho_{\mathrm{B}}^0$. This approximation is called the *Born approximation*. Together with the fact that the bath equilibrium state, defined in Eq. (2.11), is diagonal in the Fock basis, whereas H_{SB} has no diagonal elements in the Fock basis, it follows that

$$\mathrm{tr}_{\mathrm{B}}\left[H_{\mathrm{SB,I}}(t), \rho_{\mathrm{I}}(t')\right] = 0.$$

Thus, if we now form the partial trace over the bath to obtain the equation of motion for the reduced density operator of the system, $\rho_{\mathrm{S,I}}$, the first term disappears,

$$\begin{aligned}\frac{\mathrm{d}}{\mathrm{d}t}\rho_{\mathrm{S,I}}(t) = \frac{\mathrm{d}}{\mathrm{d}t}\,\mathrm{tr}_{\mathrm{B}}\left\{\rho_{\mathrm{I}}(t)\right\} &= -\frac{1}{\hbar^2}\int_{t_0}^{t} \mathrm{d}t'\,\mathrm{tr}_{\mathrm{B}}\left[H_{\mathrm{SB,I}}(t), \left[H_{\mathrm{SB,I}}(t'), \rho_{\mathrm{I}}(t')\right]\right] \\ &= -\frac{1}{\hbar^2}\int_{0}^{t-t_0} \mathrm{d}\tau\,\mathrm{tr}_{\mathrm{B}}\left[H_{\mathrm{SB,I}}(t), \left[H_{\mathrm{SB,I}}(t-\tau), \rho_{\mathrm{I}}(t-\tau)\right]\right],\end{aligned}$$

where we have transformed to relative time, $\tau = t - t'$, in the bottom line. Next, we insert the factorization for the density operator $\rho_{\mathrm{I}}(t) = \rho_{\mathrm{S,I}}(t) \otimes \rho_{\mathrm{B}}^0$ and the interaction Hamiltonian from Eq. (2.9), that is,

$$H_{\mathrm{SB}} = \sum_{i,\sigma} \zeta^{\sigma} d_i^{\sigma} B_i^{\bar{\sigma}} \quad \Rightarrow \quad H_{\mathrm{SB,I}}(t) = \sum_{i,\sigma} \zeta^{\sigma} d_i^{\sigma}(t) B_i^{\bar{\sigma}}(t).$$

Here we omit the index $\square_{\mathrm{I}}$ for the operators $d_i^{\sigma}(t)$ and $B_i^{\sigma}(t)$ for brevity. This should not lead to any confusion as the corresponding operators in the Schrödinger picture are time-independent. With this separation, we can expand the nested commutators and get

$$\begin{aligned}\frac{\mathrm{d}}{\mathrm{d}t}\rho_{\mathrm{S,I}}(t) = \frac{1}{\hbar}\sum_{ij\sigma\sigma'} \zeta^{\sigma}\zeta^{\sigma'} \int_0^{t-t_0} \frac{\mathrm{d}\tau}{\hbar} \Big\{ & G_{ij}^{\sigma'\sigma}(\tau) d_i^{\sigma}(t) d_j^{\sigma'}(t-\tau) \rho_{\mathrm{S,I}}(t-\tau) \\ & - G_{ji}^{\sigma\sigma'}(-\tau) d_i^{\sigma}(t) \rho_{\mathrm{S,I}}(t-\tau) d_j^{\sigma'}(t-\tau) \\ & - G_{ij}^{\sigma'\sigma}(\tau) d_j^{\sigma'}(t-\tau) \rho_{\mathrm{S,I}}(t-\tau) d_i^{\sigma}(t) \\ & + G_{ji}^{\sigma\sigma'}(-\tau) \rho_{\mathrm{S,I}}(t-\tau) d_j^{\sigma'}(t-\tau) d_i^{\sigma}(t) \Big\},\end{aligned}$$

where we have introduced the bath correlation functions $G_{ij}^{\sigma\sigma'}$,

$$G_{ij}^{\sigma\sigma'}(\tau) := \mathrm{tr}_{\mathrm{B}}\left\{\rho_{\mathrm{B}}^0 B_i^{\sigma}(t) B_j^{\sigma'}(t-\tau)\right\} \neq f(t). \tag{2.16}$$

Note that the bath correlation functions are independent of the time t, at which they are evaluated, because the bath operators, $B_i^\sigma(t)$, only contain the trivial time-dependence from the interaction picture. Using the fact again that the bath density operator, ρ_B^0, is diagonal in the Fock basis, whereas $B_i(t)$ and $B_i^\dagger(t)$ have no elements on the diagonal in the Fock basis, we find $G_{ij}^{\sigma\sigma'} = G_{ij}^{\sigma\bar{\sigma}} \cdot \delta_{\sigma'\bar{\sigma}}$. With $\zeta^\sigma\zeta^{\bar{\sigma}} = -1$, this simplifies the above equation to

$$\begin{aligned}\frac{\mathrm{d}}{\mathrm{d}t}\rho_\mathrm{S,I}(t) = -\frac{1}{\hbar}\sum_{ij\sigma}\int_0^{t-t_0}\frac{\mathrm{d}\tau}{\hbar}\Big\{&G_{ij}^{\bar{\sigma}\sigma}(\tau)d_i^\sigma(t)d_j^{\bar{\sigma}}(t-\tau)\rho_\mathrm{S,I}(t-\tau)\\ &- G_{ji}^{\sigma\bar{\sigma}}(-\tau)d_i^\sigma(t)\rho_\mathrm{S,I}(t-\tau)d_j^{\bar{\sigma}}(t-\tau)\\ &- G_{ij}^{\bar{\sigma}\sigma}(\tau)d_j^{\bar{\sigma}}(t-\tau)\rho_\mathrm{S,I}(t-\tau)d_i^\sigma(t)\\ &+ G_{ji}^{\sigma\bar{\sigma}}(-\tau)\rho_\mathrm{S,I}(t-\tau)d_j^{\bar{\sigma}}(t-\tau)d_i^\sigma(t)\Big\}.\end{aligned}$$

At this point, we perform the so-called *Markovian approximation*. From the assumption that the electrodes are always in their local equilibrium states, it naturally follows that the bath correlation functions are non-zero only for very short times τ, much smaller time scales than those on which the state of the system, $\rho_\mathrm{S,I}$, changes. Therefore, we can approximate $\rho_\mathrm{S,I}(t-\tau) \approx \rho_\mathrm{S,I}(t)$ under the integral. This implies further that we can extend the upper integral bound to infinity, which simplifies later calculations considerably,

$$\begin{aligned}\frac{\mathrm{d}}{\mathrm{d}t}\rho_\mathrm{S,I}(t) = -\frac{1}{\hbar}\sum_{ij\sigma}\int_0^{\infty}\frac{\mathrm{d}\tau}{\hbar}\Big\{&G_{ij}^{\bar{\sigma}\sigma}(\tau)d_i^\sigma(t)d_j^{\bar{\sigma}}(t-\tau)\rho_\mathrm{S,I}(t)\\ &- G_{ji}^{\sigma\bar{\sigma}}(-\tau)d_i^\sigma(t)\rho_\mathrm{S,I}(t)d_j^{\bar{\sigma}}(t-\tau)\\ &- G_{ij}^{\bar{\sigma}\sigma}(\tau)d_j^{\bar{\sigma}}(t-\tau)\rho_\mathrm{S,I}(t)d_i^\sigma(t)\\ &+ G_{ji}^{\sigma\bar{\sigma}}(-\tau)\rho_\mathrm{S,I}(t)d_j^{\bar{\sigma}}(t-\tau)d_i^\sigma(t)\Big\}.\end{aligned} \tag{2.17}$$

Taken together, these two approximations are often referred to as the *Born-Markov approximation*. However, the resulting master equation (2.17) is generally not trace-preserving or completely positive [31, 44]. To fix these problems, we make one further approximation, the so-called *secular approximation*. For this, we first determine the eigenvalues and eigenstates of the system Hamiltonian, $H_\mathrm{S}\,|E_n\rangle = E_n\,|E_n\rangle$. Using these, we split the creation and annihilation operators of the system, d_i^σ, into their various frequency components,

$$\begin{aligned}d_i^\sigma(\omega) &:= \sum_{\substack{(n,m)\\ E_m - E_n = \hbar\omega}} |E_n\rangle\langle E_n|\, d_i^\sigma\, |E_m\rangle\langle E_m|\,, \\ \Rightarrow \quad d_i^\sigma &= \sum_\omega d_i^\sigma(\omega).\end{aligned} \tag{2.18}$$

We call them *frequency projected operators*, $d_i^\sigma(\omega)$. These fulfill the following commutation relations,

$$\Big[H_\mathrm{S}, d_i^\sigma(\omega)\Big] = -\hbar\omega\, d_i^\sigma(\omega), \tag{2.19}$$

$$\Big[H_\mathrm{S}, d_i(\omega)\Big[d_j(\omega)\Big]^\dagger\Big] = 0, \tag{2.20}$$

$$\Big[H_\mathrm{S}, \Big[d_j(\omega)\Big]^\dagger d_i(\omega)\Big] = 0, \tag{2.21}$$

where we have used $d_i^{\bar{\sigma}}(-\omega) = [d_i^{\sigma}(\omega)]^\dagger$. With Eq. (2.19), the time-dependent interaction picture operators can be easily represented,

$$e^{\mathrm{i}H_{\mathrm{S}}t/\hbar} d_i^{\sigma}(\omega) e^{-\mathrm{i}H_{\mathrm{S}}t} = e^{-\mathrm{i}\omega t} d_i^{\sigma}(\omega), \tag{2.22}$$

$$d_i^{\sigma}(t) = \sum_{\omega} e^{\mathrm{i}H_{\mathrm{S}}t/\hbar} d_i^{\sigma}(\omega) e^{-\mathrm{i}H_{\mathrm{S}}t/\hbar} = \sum_{\omega} e^{-\mathrm{i}\omega t} d_i^{\sigma}(\omega). \tag{2.23}$$

Using this expansion in Eq. (2.17), we get

$$\begin{aligned}\frac{\mathrm{d}}{\mathrm{d}t}\rho_{\mathrm{S,I}}(t) = -\frac{1}{\hbar}\sum_{ij\sigma}\sum_{\omega\omega'} e^{-\mathrm{i}(\omega+\omega')t}\int_0^\infty \frac{\mathrm{d}\tau}{\hbar} e^{\mathrm{i}\omega'\tau}\Big\{ & G_{ij}^{\bar{\sigma}\sigma}(\tau) d_i^{\sigma}(\omega) d_j^{\bar{\sigma}}(\omega')\rho_{\mathrm{S,I}}(t) \\ & - G_{ji}^{\sigma\bar{\sigma}}(-\tau) d_i^{\sigma}(\omega)\rho_{\mathrm{S,I}}(t) d_j^{\bar{\sigma}}(\omega') \\ & - G_{ij}^{\bar{\sigma}\sigma}(\tau) d_j^{\bar{\sigma}}(\omega')\rho_{\mathrm{S,I}}(t) d_i^{\sigma}(\omega) \\ & + G_{ji}^{\sigma\bar{\sigma}}(-\tau)\rho_{\mathrm{S,I}}(t) d_j^{\bar{\sigma}}(\omega') d_i^{\sigma}(\omega)\Big\}.\end{aligned}$$

We now have a series of rapidly oscillating terms for $\omega \neq -\omega'$ next to a set of non-oscillating terms for $\omega = -\omega'$. In the spirit of a rotating-wave approximation, we neglect all the oscillating terms, keeping only the terms with $\omega = -\omega'$, thereby reducing the equation of motion to a single sum over ω,

$$\begin{aligned}\frac{\mathrm{d}}{\mathrm{d}t}\rho_{\mathrm{S,I}}(t) = -\frac{1}{\hbar}\sum_{ij\sigma}\sum_{\omega}\int_0^\infty \frac{\mathrm{d}\tau}{\hbar} e^{-\mathrm{i}\omega\tau}\Big\{ & G_{ij}^{\bar{\sigma}\sigma}(\tau) d_i^{\sigma}(\omega) d_j^{\bar{\sigma}}(-\omega)\rho_{\mathrm{S,I}}(t) \\ & - G_{ji}^{\sigma\bar{\sigma}}(-\tau) d_i^{\sigma}(\omega)\rho_{\mathrm{S,I}}(t) d_j^{\bar{\sigma}}(-\omega) \\ & - G_{ij}^{\bar{\sigma}\sigma}(\tau) d_j^{\bar{\sigma}}(-\omega)\rho_{\mathrm{S,I}}(t) d_i^{\sigma}(\omega) \\ & + G_{ji}^{\sigma\bar{\sigma}}(-\tau)\rho_{\mathrm{S,I}}(t) d_j^{\bar{\sigma}}(-\omega) d_i^{\sigma}(\omega)\Big\}.\end{aligned}$$

To write the above in a more compact form, we start by writing out the sum over σ using $d_i^{\bar{\sigma}}(-\omega) = [d_i^{\sigma}(\omega)]^\dagger$, where we use the notation

$$G_{ij}^{<}(\tau) := G_{ij}^{\dagger -}(\tau), \qquad\qquad G_{ij}^{>}(\tau) := G_{ij}^{-\dagger}(\tau), \tag{2.24}$$

and introduce the one-sided Fourier-transformed bath correlation functions,

$$\begin{aligned}\tilde{G}_{ij}^{<}(\omega) &:= \int_0^\infty \frac{\mathrm{d}\tau}{\hbar} G_{ij}^{<}(\tau) e^{-\mathrm{i}\omega\tau}, \\ \tilde{G}_{ij}^{>}(\omega) &:= \int_0^\infty \frac{\mathrm{d}\tau}{\hbar} G_{ji}^{>}(-\tau) e^{-\mathrm{i}\omega\tau}.\end{aligned}$$

We get

$$\begin{aligned}\frac{\mathrm{d}}{\mathrm{d}t}\rho_{\mathrm{S,I}}(t) = -\frac{1}{\hbar}\sum_{ij\omega}\Big\{ & d_i(\omega)\Big[d_j(\omega)\Big]^\dagger \rho_{\mathrm{S,I}}(t)\tilde{G}_{ij}^{<}(\omega) - d_i(\omega)\rho_{\mathrm{S,I}}(t)\Big[d_j(\omega)\Big]^\dagger \tilde{G}_{ij}^{>}(\omega) \\ & - \Big[d_j(\omega)\Big]^\dagger \rho_{\mathrm{S,I}}(t) d_i(\omega)\tilde{G}_{ij}^{<}(\omega) + \rho_{\mathrm{S,I}}(t)\Big[d_j(\omega)\Big]^\dagger d_i(\omega)\tilde{G}_{ij}^{>}(\omega) \\ & + \Big[d_i(\omega)\Big]^\dagger d_j(\omega)\rho_{\mathrm{S,I}}(t)\Big[\tilde{G}_{ij}^{>}(\omega)\Big]^* - \Big[d_i(\omega)\Big]^\dagger \rho_{\mathrm{S,I}}(t) d_j(\omega)\Big[\tilde{G}_{ij}^{<}(\omega)\Big]^* \\ & - d_j(\omega)\rho_{\mathrm{S,I}}(t)\Big[d_i(\omega)\Big]^\dagger\Big[\tilde{G}_{ij}^{>}(\omega)\Big]^* + \rho_{\mathrm{S,I}}(t) d_j(\omega)\Big[d_i(\omega)\Big]^\dagger\Big[\tilde{G}_{ij}^{<}(\omega)\Big]^*\Big\}.\end{aligned}$$

In the next step, we exchange the indices i and j of the last four terms and group similar terms together,

$$\begin{aligned}\frac{\mathrm{d}}{\mathrm{d}t}\rho_{\mathrm{S,I}}(t) = -\frac{1}{\hbar}\sum_{ij\omega}\Big\{ & d_i(\omega)\Big[d_j(\omega)\Big]^\dagger \rho_{\mathrm{S,I}}(t)\tilde{G}^<_{ij}(\omega) + \rho_{\mathrm{S,I}}(t)d_i(\omega)\Big[d_j(\omega)\Big]^\dagger\Big[\tilde{G}^<_{ji}(\omega)\Big]^* \\ & + \rho_{\mathrm{S,I}}(t)\Big[d_j(\omega)\Big]^\dagger d_i(\omega)\tilde{G}^>_{ij}(\omega) + \Big[d_j(\omega)\Big]^\dagger d_i(\omega)\rho_{\mathrm{S,I}}(t)\Big[\tilde{G}^>_{ji}(\omega)\Big]^* \\ & - \Big[d_j(\omega)\Big]^\dagger \rho_{\mathrm{S,I}}(t)d_i(\omega)\Big(\tilde{G}^<_{ij}(\omega) + \Big[\tilde{G}^<_{ji}(\omega)\Big]^*\Big) \\ & - d_i(\omega)\rho_{\mathrm{S,I}}(t)\Big[d_j(\omega)\Big]^\dagger\Big(\tilde{G}^>_{ij}(\omega) + \Big[\tilde{G}^>_{ji}(\omega)\Big]^*\Big)\Big\}.\end{aligned}$$

Note that the first two lines each have the structure $\mathcal{A}\mathcal{B}x+\mathcal{B}\mathcal{A}y$, where $\mathcal{A} \in \{d_i d_j^\dagger, d_j^\dagger d_i\}$, $\mathcal{B} = \rho_{\mathrm{S}}(t)$, and x, y are the transformed correlation functions. This structure can be reshaped to the sum of an anticommutator and a commutator, namely, $\frac{1}{2}\{\mathcal{A},\mathcal{B}\}(x+y) + \frac{1}{2}[\mathcal{A},\mathcal{B}](x-y)$. Applying this procedure to the above, we get

$$\begin{aligned}\frac{\mathrm{d}}{\mathrm{d}t}\rho_{\mathrm{S,I}}(t) = -\frac{1}{\hbar}\sum_{ij\omega}\Big\{ & \frac{1}{2}\Big\{d_i(\omega)\Big[d_j(\omega)\Big]^\dagger, \rho_{\mathrm{S,I}}(t)\Big\}\Big(\tilde{G}^<_{ij}(\omega) + \Big[\tilde{G}^<_{ji}(\omega)\Big]^*\Big) \\ & + \frac{1}{2}\Big[d_i(\omega)\Big[d_j(\omega)\Big]^\dagger, \rho_{\mathrm{S,I}}(t)\Big]\Big(\tilde{G}^<_{ij}(\omega) - \Big[\tilde{G}^<_{ji}(\omega)\Big]^*\Big) \\ & + \frac{1}{2}\Big\{\Big[d_j(\omega)\Big]^\dagger d_i(\omega), \rho_{\mathrm{S,I}}(t)\Big\}\Big(\tilde{G}^>_{ij}(\omega) + \Big[\tilde{G}^>_{ji}(\omega)\Big]^*\Big) \\ & - \frac{1}{2}\Big[\Big[d_j(\omega)\Big]^\dagger d_i(\omega), \rho_{\mathrm{S,I}}(t)\Big]\Big(\tilde{G}^>_{ij}(\omega) - \Big[\tilde{G}^>_{ji}(\omega)\Big]^*\Big) \\ & - \Big[d_j(\omega)\Big]^\dagger \rho_{\mathrm{S,I}}(t)d_i(\omega)\Big(\tilde{G}^<_{ij}(\omega) + \Big[\tilde{G}^<_{ji}(\omega)\Big]^*\Big) \\ & - d_i(\omega)\rho_{\mathrm{S,I}}(t)\Big[d_j(\omega)\Big]^\dagger\Big(\tilde{G}^>_{ij}(\omega) + \Big[\tilde{G}^>_{ji}(\omega)\Big]^*\Big)\Big\}.\end{aligned}$$

At this point, we are left with six terms, each containing a sum of two one-sided Fourier-transformed correlation functions. We define these sums as new quantities,

$$S^<_{ij}(\omega) = \frac{1}{2\mathrm{i}}\Big(\tilde{G}^<_{ij}(\omega) - \Big[\tilde{G}^<_{ji}(\omega)\Big]^*\Big) = \frac{1}{2\mathrm{i}}\int_0^\infty \frac{\mathrm{d}\tau}{\hbar}\Big(G^<_{ij}(\tau)e^{-\mathrm{i}\omega\tau} - G^<_{ij}(-\tau)e^{\mathrm{i}\omega\tau}\Big), \quad (2.25)$$

$$S^>_{ij}(\omega) = \frac{1}{2\mathrm{i}}\Big(\Big[\tilde{G}^>_{ji}(\omega)\Big]^* - \tilde{G}^>_{ij}(\omega)\Big) = \frac{1}{2\mathrm{i}}\int_0^\infty \frac{\mathrm{d}\tau}{\hbar}\Big(G^>_{ji}(\tau)e^{\mathrm{i}\omega\tau} - G^>_{ji}(-\tau)e^{-\mathrm{i}\omega\tau}\Big), \quad (2.26)$$

$$\gamma^<_{ij}(\omega) = \tilde{G}^<_{ij}(\omega) + \Big[\tilde{G}^<_{ji}(\omega)\Big]^* = \int_{-\infty}^\infty \frac{\mathrm{d}\tau}{\hbar}G^<_{ij}(\tau)e^{-\mathrm{i}\omega\tau}, \quad (2.27)$$

$$\gamma^>_{ij}(\omega) = \tilde{G}^>_{ij}(\omega) + \Big[\tilde{G}^>_{ji}(\omega)\Big]^* = \int_{-\infty}^\infty \frac{\mathrm{d}\tau}{\hbar}G^>_{ji}(-\tau)e^{-\mathrm{i}\omega\tau}. \quad (2.28)$$

This allows us to write the equation of motion in a more compact form,

$$\begin{aligned}\frac{\mathrm{d}}{\mathrm{d}t}\rho_{\mathrm{S,I}}(t) = & -\frac{\mathrm{i}}{\hbar}\Big[\sum_{ij\omega}\Big(S^<_{ij}(\omega)d_i(\omega)\Big[d_j(\omega)\Big]^\dagger + S^>_{ij}(\omega)\Big[d_j(\omega)\Big]^\dagger d_i(\omega)\Big), \rho_{\mathrm{S,I}}(t)\Big] \\ & + \frac{1}{\hbar}\sum_{ij\omega}\Big\{\Big(\Big[d_j(\omega)\Big]^\dagger \rho_{\mathrm{S,I}}(t)d_i(\omega) - \frac{1}{2}\Big\{d_i(\omega)\Big[d_j(\omega)\Big]^\dagger, \rho_{\mathrm{S,I}}(t)\Big\}\Big)\cdot\gamma^<_{ij}(\omega) \\ & + \Big(d_i(\omega)\rho_{\mathrm{S,I}}(t)\Big[d_j(\omega)\Big]^\dagger - \frac{1}{2}\Big\{\Big[d_j(\omega)\Big]^\dagger d_i(\omega), \rho_{\mathrm{S,I}}(t)\Big\}\Big)\cdot\gamma^>_{ij}(\omega)\Big\}.\end{aligned}$$

Note that the commutator term in the above equation provides a Hamiltonian contribution to the dynamics. This term effectively renormalizes the system's energy levels and corresponds to the *Lamb shift*. Thus, we define the Lamb shift Hamiltonian as

$$H_{\mathrm{LS}} := \sum_{ij\omega} \Big(S^{<}_{ij}(\omega) d_i(\omega) \Big[d_j(\omega) \Big]^\dagger + S^{>}_{ij}(\omega) \Big[d_j(\omega) \Big]^\dagger d_i(\omega) \Big). \tag{2.29}$$

From $[G^{<}_{ij}(\tau)]^* = G^{<}_{ji}(-\tau)$, it follows that $[S^{<}_{ij}(\omega)]^* = S^{<}_{ji}(\omega)$, and analogously for $S^{>}_{ij}$. From this, it is easy to see that the Lamb shift Hamiltonian defined above is Hermitian, $H^\dagger_{\mathrm{LS}} = H_{\mathrm{LS}}$. Furthermore, by virtue of Eqs. (2.20) and (2.21), it follows that $[H_{\mathrm{S}}, H_{\mathrm{LS}}] = 0$.

At this point, we translate the equation of motion back into the Schrödinger picture, remembering that $[H_{\mathrm{S}}, H_{\mathrm{B}}] = [H_{\mathrm{S}}, H_{\mathrm{LS}}] = 0$. Further, we need Eq. (2.20), and the fact that $e^{-\mathrm{i}H_{\mathrm{S}}t/\hbar} d_i(\omega) = e^{\mathrm{i}\omega t} d_i(\omega) e^{-\mathrm{i}H_{\mathrm{S}}t/\hbar}$, which results from Eq. (2.22). Altogether, we arrive at the following master equation,

$$\begin{aligned} \frac{\mathrm{d}}{\mathrm{d}t}\rho_{\mathrm{S}}(t) = &- \frac{\mathrm{i}}{\hbar}\Big[H_{\mathrm{S}} + H_{\mathrm{LS}}, \rho_{\mathrm{S}}(t)\Big] \\ &+ \frac{1}{\hbar}\sum_{ij\omega}\Bigg\{ \bigg(\Big[d_j(\omega)\Big]^\dagger \rho_{\mathrm{S}}(t) d_i(\omega) - \frac{1}{2}\Big\{ d_i(\omega)\Big[d_j(\omega)\Big]^\dagger, \rho_{\mathrm{S}}(t) \Big\}\bigg) \cdot \gamma^{<}_{ij}(\omega) \\ &\quad + \bigg(d_i(\omega)\rho_{\mathrm{S}}(t)\Big[d_j(\omega)\Big]^\dagger - \frac{1}{2}\Big\{ \Big[d_j(\omega)\Big]^\dagger d_i(\omega), \rho_{\mathrm{S}}(t) \Big\}\bigg) \cdot \gamma^{>}_{ij}(\omega) \Bigg\}. \end{aligned} \tag{2.30}$$

Eq. (2.30) is our final form of the Born-Markov master equation (BMME). It has the standard form, called the *Lindblad form*, defined in Eq. (3.66) in [31]. As outlined in [31], this form guarantees the trace preservation and complete positivity of the master equation. Since we have derived the above Eq. (2.30) using three approximations, its validity is limited. We will discuss this limitation in Sec. 2.2.4.

Before we can use Eq. (2.30) in practice, we must also determine the Fourier-transformed correlation functions defined in Eqs. (2.25) to (2.28). As mentioned in Sec. 2.1, we always work in the *wideband limit* in the following, that is, we assume the electrode coupling functions, $\Gamma^K_{ij}(\omega)$, defined in Eq. (2.8), to equal a constant value,

$$\Gamma^K_{ij} := \Gamma^K_{ij}(\omega) = 2\pi \sum_{k_K} V_{i,k_K} V^*_{j,k_K} \delta(\varepsilon_{k_K} - \hbar\omega), \tag{2.31}$$

though they may change for different electronic levels, i and j, and for the different electrodes, $K \in \{\mathrm{L}, \mathrm{R}\}$. In the wideband limit, the Fourier-transformed correlation functions can be calculated analytically. The detailed procedure can be found in Appendix A. We find

$$\gamma^{<}_{ij}(\omega) = \sum_K \Gamma^K_{ij}\, f^K(\hbar\omega), \tag{2.32}$$

$$\gamma^{>}_{ij}(\omega) = \sum_K \Gamma^K_{ij} \Big(1 - f^K(\hbar\omega)\Big), \tag{2.33}$$

$$S^{<}_{ij}(\omega) = S^{>}_{ij}(\omega) = \sum_K \Gamma^K_{ij}\, \psi^K(\hbar\omega), \tag{2.34}$$

where f^K is the Fermi function given in Eq. (A.2), and ψ^K is defined in Eq. (A.4).

2.2.2 Calculation of steady state

In the following work, the transient dynamics of the molecular junction are not studied, which means that only the unique steady state, $\rho_{\mathrm{S}}^{\mathrm{ss}}$, is of interest. The steady state of a linear differential equation is easily obtained if the differential equation is in the form

$$\frac{\mathrm{d}}{\mathrm{d}t}\left|\rho\right\rangle = L\left|\rho\right\rangle,$$

where the unknowns are written as a vector, $|\rho\rangle$, and the matrix L represents the action of the differential equation on this vector. To put the BMME defined in Eq. (2.30) into this form, a transition to the vector space of the linear operators, which act in the Hilbert space of the nanosystem, is required. This space of linear operators is also called the *Liouville space*. In this space, the usual $n \times n$ matrix representation of the system density operator, ρ_{S}, is flattened into an n^2 vector, $|\rho_{\mathrm{S}}\rangle$. We do this flattening by ordering the columns of ρ_{S} one below the other. In the Liouville space, left-hand and right-hand matrix multiplication with ρ_{S} turn into left-hand matrix-vector multiplication with $|\rho_{\mathrm{S}}\rangle$ as follows [45],

$$A\rho_{\mathrm{S}} \quad \rightarrow \quad (\mathbb{1} \otimes A)\left|\rho_{\mathrm{S}}\right\rangle, \qquad \rho_{\mathrm{S}} A \quad \rightarrow \quad (A^{\mathrm{T}} \otimes \mathbb{1})\left|\rho_{\mathrm{S}}\right\rangle,$$

where $\mathbb{1}$ denotes the $n \times n$ unit matrix and $\otimes$ denotes the Kronecker direct product. With this, the BMME from Eq. (2.30) takes the desired form

$$\frac{\mathrm{d}}{\mathrm{d}t}\left|\rho_{\mathrm{S}}\right\rangle = L\left|\rho_{\mathrm{S}}\right\rangle, \tag{2.35}$$

where the matrix L, usually called the *Liouvillian matrix*, is given by

$$\begin{aligned} L = &-\frac{\mathrm{i}}{\hbar}\Big(\mathbb{1} \otimes \Big(H_{\mathrm{S}} + H_{\mathrm{LS}}\Big) - \Big(H_{\mathrm{S}} + H_{\mathrm{LS}}\Big)^{\mathrm{T}} \otimes \mathbb{1}\Big) \\ &+ \frac{1}{\hbar}\sum_{ij\omega}\Big\{\gamma_{ij}^{<}(\omega) \cdot \Big[d_i(\omega)\Big]^{\mathrm{T}} \otimes \Big[d_j(\omega)\Big]^{\dagger} \\ &\quad - \frac{1}{2}\gamma_{ij}^{<}(\omega) \cdot \Big(\mathbb{1} \otimes \Big(d_i(\omega)\Big[d_j(\omega)\Big]^{\dagger}\Big) + \Big(d_i(\omega)\Big[d_j(\omega)\Big]^{\dagger}\Big)^{\mathrm{T}} \otimes \mathbb{1}\Big) \\ &\quad + \gamma_{ij}^{>}(\omega) \cdot \Big[d_j(\omega)\Big]^{\dagger\mathrm{T}} \otimes d_i(\omega) \\ &\quad - \frac{1}{2}\gamma_{ij}^{>}(\omega) \cdot \Big(\mathbb{1} \otimes \Big(\Big[d_j(\omega)\Big]^{\dagger} d_i(\omega)\Big) + \Big(\Big[d_j(\omega)\Big]^{\dagger} d_i(\omega)\Big)^{\mathrm{T}} \otimes \mathbb{1}\Big)\Big\}. \end{aligned} \tag{2.36}$$

The steady-state vector, $|\rho_{\mathrm{S}}^{\mathrm{ss}}\rangle$, can now be found by solving $L\left|\rho_{\mathrm{S}}^{\mathrm{ss}}\right\rangle = 0$, and then be transformed back into the steady-state density matrix, $\rho_{\mathrm{S}}^{\mathrm{ss}}$.

In practice, however, directly solving the equation $L\left|\rho_{\mathrm{S}}^{\mathrm{ss}}\right\rangle = 0$ is often undesirable because many powerful linear equation solvers work by inverting the matrix L to find the solution. This is impossible here since we assume L to be singular. A common way around this is to define an auxiliary operator, Tr_{S}, which essentially acts like the trace, tr_{S}, on ρ_{S}, but projects the resulting scalar value onto one of the basis vectors of the Liouvillian space, $|\mathbf{u}\rangle$. We can now find the steady state by solving

$$(L + \mathrm{Tr}_{\mathrm{S}})\left|\rho_{\mathrm{S}}^{\mathrm{ss}}\right\rangle = \left|\mathbf{u}\right\rangle, \tag{2.37}$$

where we exploited the fact that $\mathrm{tr}_{\mathrm{S}}\{\rho_{\mathrm{S}}\} = 1$. This brings the additional effect that the resulting solution $|\rho_{\mathrm{S}}^{\mathrm{ss}}\rangle$ is, by design, correctly normalized. In the following, we use the routines `scipy.linalg.solve` [46] and `scipy.linalg.lstsq` [47] from the Python library SciPy to solve Eq. (2.37) for the steady state, $|\rho_{\mathrm{S}}^{\mathrm{ss}}\rangle$.

2.2.3 Observables of interest

As aforementioned, we study the flow of an electric current through a molecular junction and its induced effects on the vibrational modes of the molecule. Therefore, the observables of interest include the steady-state electric current, on the one hand, and various steady-state characteristics of the vibrational modes. The latter include the average excitation, $\langle N\rangle^{\mathrm{ss}} = \langle a^\dagger a\rangle^{\mathrm{ss}}$, the mean values of displacement and momentum, $\langle\hat{x}\rangle^{\mathrm{ss}}$ and $\langle\hat{p}\rangle^{\mathrm{ss}}$, and the mean values of their squares, $\langle\hat{x}^2\rangle^{\mathrm{ss}}$ and $\langle\hat{p}^2\rangle^{\mathrm{ss}}$. Since N, $\hat{x}$, and $\hat{p}$ are operators acting solely on the system Hilbert space, we can find their steady-state expectation values directly from $\rho_{\mathrm{S}}^{\mathrm{ss}}$,

$$\langle A\rangle^{\mathrm{ss}} = \mathrm{tr}_{\mathrm{S}}\{\rho_{\mathrm{S}}^{\mathrm{ss}} A\}.$$

The procedure is not as straightforward for the electric current because there is no inherent operator associated with it. In the following, we use the continuity relation of charge to derive a system-internal representation of the average electric current.

Electric charge is a conserved quantity, and despite the approximations included in the BMME, it indeed conserves charge. Therefore, the total charge of our model, given by the sum of the number operators, $N_{\mathrm{L}} + N_{\mathrm{S}} + N_{\mathrm{R}}$, times the elementary charge, is constant,

$$0 = \mathrm{e}\,\frac{\mathrm{d}}{\mathrm{d}t}\langle N_{\mathrm{L}} + N_{\mathrm{S}} + N_{\mathrm{R}}\rangle_t = \mathrm{e}\,\frac{\mathrm{d}}{\mathrm{d}t}\langle N_{\mathrm{L}}\rangle_t + \mathrm{e}\,\frac{\mathrm{d}}{\mathrm{d}t}\langle N_{\mathrm{S}}\rangle_t + \mathrm{e}\,\frac{\mathrm{d}}{\mathrm{d}t}\langle N_{\mathrm{R}}\rangle_t,$$

where $N_{\mathrm{S}} = \sum_i n_i = \sum_i d_i^\dagger d_i$ is the fermionic number operator of the system. This is the continuity relation of charge for our model. The current flowing from the left electrode into the system, which we denote by $\langle I_{\mathrm{L}}\rangle_t$, is given by

$$\langle I_{\mathrm{L}}\rangle_t = -\mathrm{e}\,\frac{\mathrm{d}}{\mathrm{d}t}\langle N_{\mathrm{L}}\rangle_t,$$

and vice versa for the current flowing from the right electrode into the system, $\langle I_{\mathrm{R}}\rangle_t$. With this, the continuity relation turns into

$$\mathrm{e}\,\frac{\mathrm{d}}{\mathrm{d}t}\langle N_{\mathrm{S}}\rangle_t = \langle I_{\mathrm{L}}\rangle_t + \langle I_{\mathrm{R}}\rangle_t. \tag{2.38}$$

The left-hand side of the above contains only operators acting in the system Hilbert space. Thus, it can be directly calculated from $\rho_{\mathrm{S}}(t)$ or $\rho_{\mathrm{S}}^{\mathrm{ss}}$. The right-hand side follows accordingly, but to find the separate currents, $\langle I_{\mathrm{L}}\rangle_t$ and $\langle I_{\mathrm{R}}\rangle_t$, we need to split $\frac{\mathrm{d}}{\mathrm{d}t}\langle N_{\mathrm{S}}\rangle_t$ in its respective contributions from the left and right electrodes. For this, we evaluate $\frac{\mathrm{d}}{\mathrm{d}t}\langle N_{\mathrm{S}}\rangle_t$ using the BMME. The detailed evaluation is shown in Appendix C. We find

$$\begin{aligned}\frac{\mathrm{d}}{\mathrm{d}t}\langle N_{\mathrm{S}}\rangle_t = \frac{1}{\hbar}\sum_{ij\omega}\mathrm{tr}_{\mathrm{S}}\Big\{ & d_i(\omega)\Big[d_j(\omega)\Big]^\dagger \rho_{\mathrm{S}}(t)\gamma_{ij}^{<}(\omega) \\ & - \Big[d_j(\omega)\Big]^\dagger d_i(\omega)\rho_{\mathrm{S}}(t)\gamma_{ij}^{>}(\omega)\Big\}.\end{aligned} \tag{2.39}$$

According to Eqs. (2.32) and (2.33), we can split the Fourier-transformed correlation functions $\gamma_{ij}^{<}$ and $\gamma_{ij}^{>}$ into parts corresponding to the different electrodes,

$$\begin{aligned}\gamma_{ij}^{<,K}(\omega) &:= \Gamma_{ij}^K\, f^K(\hbar\omega) && \Rightarrow\quad \gamma_{ij}^{<}(\omega) = \sum_K \gamma_{ij}^{<,K}(\omega), \\ \gamma_{ij}^{>,K}(\omega) &:= \Gamma_{ij}^K\left(1 - f^K(\hbar\omega)\right) && \Rightarrow\quad \gamma_{ij}^{>}(\omega) = \sum_K \gamma_{ij}^{>,K}(\omega).\end{aligned} \tag{2.40}$$

Using this in Eq. (2.39) and comparing it with the continuity relation, Eq. (2.38), we find the current from the different electrodes,

$$\begin{aligned}\langle I_{\mathrm{L}}\rangle_t = \frac{\mathrm{e}}{\hbar}\sum_{ij\omega}\mathrm{tr}_{\mathrm{S}}\Big\{ & d_i(\omega)\Big[d_j(\omega)\Big]^\dagger\rho_{\mathrm{S}}(t)\gamma_{ij}^{<,\mathrm{L}}(\omega) \\ & - \Big[d_j(\omega)\Big]^\dagger d_i(\omega)\rho_{\mathrm{S}}(t)\gamma_{ij}^{>,\mathrm{L}}(\omega)\Big\}, \\ \langle I_{\mathrm{R}}\rangle_t = \frac{\mathrm{e}}{\hbar}\sum_{ij\omega}\mathrm{tr}_{\mathrm{S}}\Big\{ & d_i(\omega)\Big[d_j(\omega)\Big]^\dagger\rho_{\mathrm{S}}(t)\gamma_{ij}^{<,\mathrm{R}}(\omega) \\ & - \Big[d_j(\omega)\Big]^\dagger d_i(\omega)\rho_{\mathrm{S}}(t)\gamma_{ij}^{>,\mathrm{R}}(\omega)\Big\}.\end{aligned} \tag{2.41}$$

In the steady state, when all expectation values of the system are constant in time, $\langle I_{\mathrm{L}}\rangle^{\mathrm{ss}} = -\langle I_{\mathrm{R}}\rangle^{\mathrm{ss}}$ follows immediately from the continuity relation, Eq. (2.38). Since we are only interested in the steady state in this work, only the steady-state current from the left electrode will be indicated in the following. We will refer to it for short as the steady-state current, $\langle I\rangle^{\mathrm{ss}}$,

$$\begin{aligned}\langle I\rangle^{\mathrm{ss}} := \langle I_{\mathrm{L}}\rangle^{\mathrm{ss}} = \frac{\mathrm{e}}{\hbar}\sum_{ij\omega}\mathrm{tr}_{\mathrm{S}}\Big\{ & d_i(\omega)\Big[d_j(\omega)\Big]^\dagger\rho_{\mathrm{S}}^{\mathrm{ss}}\gamma_{ij}^{<,\mathrm{L}}(\omega) \\ & - \Big[d_j(\omega)\Big]^\dagger d_i(\omega)\rho_{\mathrm{S}}^{\mathrm{ss}}\gamma_{ij}^{>,\mathrm{L}}(\omega)\Big\}.\end{aligned} \tag{2.42}$$

2.2.4 Validity of the Born-Markov approximation

In the derivation of the BMME in Sec. 2.2.1, we have used three approximations. Therefore, the validity of the master equation is limited to fulfilling these approximations. As mentioned several times, the fundamental assumption of the Born-Markov approximation is weak coupling between the nanosystem and the electrodes.

In performing the Born approximation, we specifically assume that the interaction between the nanosystem and the electrodes does not significantly influence the state of the electrodes. This is fulfilled in parts already by the design of the junction model. Since the nanosystem in the center of the junction is orders of magnitude smaller than the macroscopic electrodes and has correspondingly fewer degrees of freedom, it is naturally clear that the influence of the nanosystem on the electrodes can be very small at most. The weak-coupling assumption promotes this further. In addition, we neglected higher-order interaction terms with the electrodes by applying the Born approximation. These include, for example, cotunneling events of two electrons simultaneously. The contribution of these higher-order terms scales with $(\Gamma_{ij}^K)^{n>1}$. Hence, they are negligible under the above weak-coupling assumption.

In the Markovian approximation, we assume that after an interaction with the system, the electrodes always return to their local equilibrium state before interacting with the system again. The time scale of relaxation of electrode K is given by its thermal energy, as we show in Appendix D,

$$\tau_{\mathrm{relax},K} = \frac{\hbar}{\pi k_{\mathrm{B}} T_K}.$$

The time scale of interactions between the system and the electrodes is given by their coupling, defined in Eq. (2.31). Since each electronic level of the nanosystem interacts independently with the electrodes, the respective total coupling to either of the electrodes determines the interaction time scale,

$$\tau_{\mathrm{int},K} \sim \frac{\hbar}{\sum_{ij} \Gamma_{ij}^K}.$$

For the Markovian assumption to be satisfied, we require

$$\tau_{\mathrm{relax},K} \ll \tau_{\mathrm{int},K} \qquad \Rightarrow \qquad \sum_{ij} \Gamma_{ij}^K \ll k_{\mathrm{B}} T_K,$$

for each electrode.

Furthermore, we neglected rapidly oscillating terms in the master equation by applying the additional secular approximation. While this approximation is, in a sense, required to obtain trace preservation and complete positivity, it is still an approximation. For it to be justified, the inverse frequency difference between any two distinct frequencies of the nanosystem, $|\omega - \omega'|^{-1}$, must be much smaller than the frequency of interactions with the electrodes, $\tau_{\mathrm{int},K}$, [31]

$$\frac{1}{|\omega - \omega'|} \ll \tau_{\mathrm{int},K} \qquad \Rightarrow \qquad \sum_{ij} \Gamma_{ij}^K \ll \frac{1}{\hbar |\omega - \omega'|}, \qquad \forall \omega \neq \omega'.$$

2.3 Examples

2.3.1 Resonant level model

So far, our derivations have been fairly general. In this section, we consider a first example of a molecular junction to demonstrate the BMME approach and the features of the resulting current-voltage characteristics. The simplest example system is the well-known resonant level model (RLM), also called the resonant tunneling model [48], which comprises just one electronic level. We do not take any spin-related effects into account, such that

$$H_{\mathrm{S}} = \varepsilon d^\dagger d,$$

and the corresponding interaction Hamiltonian is

$$H_{\mathrm{SB}} = -d \cdot \underbrace{\sum_{K\in\{L,R\}} \sum_{k_K} V c_{k_K}^\dagger}_{B^\dagger} + d^\dagger \cdot \underbrace{\sum_{K\in\{L,R\}} \sum_{k_K} V^* c_{k_K}}_{B}. \tag{2.43}$$

Starting from the general BMME in Eq. (2.30), we derive the equation of motion for this system. The sum over i and j disappears because we have only one creation and annihilation operator. We have, in principle, two possible frequencies in the system: $\omega = \pm\varepsilon/\hbar$. But a short calculation shows that $d(-\varepsilon/\hbar) = 0$; thus, only the positive one contributes. The resulting equation of motion is

$$\begin{aligned}\frac{\mathrm{d}}{\mathrm{d}t}\rho_{\mathrm{S}}(t) = &-\frac{\mathrm{i}}{\hbar}\left[H_{\mathrm{S}} + H_{\mathrm{LS}}, \rho_{\mathrm{S}}(t)\right] \\ &+ \frac{1}{\hbar}\left\{d^\dagger \rho_{\mathrm{S}}(t) d - \frac{1}{2} d d^\dagger \rho_{\mathrm{S}}(t) - \frac{1}{2}\rho_{\mathrm{S}}(t) d d^\dagger\right\} \cdot \gamma^< \\ &+ \frac{1}{\hbar}\left\{d \rho_{\mathrm{S}}(t) d^\dagger - \frac{1}{2} d^\dagger d \rho_{\mathrm{S}}(t) - \frac{1}{2}\rho_{\mathrm{S}}(t) d^\dagger d\right\} \cdot \gamma^>,\end{aligned}$$

where we used $d(\varepsilon/\hbar) = d$, and we defined $\gamma^{\lessgtr} := \gamma^{\lessgtr}(\varepsilon/\hbar)$. This matrix equation evaluates to the following differential equations for the elements $\rho_{ij} := \langle i|\rho_{\mathrm{S}}(t)|j\rangle$ of $\rho_{\mathrm{S}}(t)$, where $|0\rangle$ and $|1\rangle$ are the Fock basis states defined by Eq. (2.1),

$$\begin{aligned}\frac{\mathrm{d}}{\mathrm{d}t}\rho_{00} &= -\frac{\gamma_1}{\hbar}\rho_{00} + \frac{\gamma_2}{\hbar}\left(1 - \rho_{00}\right) = -\frac{\mathrm{d}}{\mathrm{d}t}\rho_{11}, \\ \frac{\mathrm{d}}{\mathrm{d}t}\rho_{01} &= \frac{\mathrm{i}\varepsilon}{\hbar}\rho_{01} - \frac{\gamma_1 + \gamma_2}{2\hbar}\rho_{01} = \frac{\mathrm{d}}{\mathrm{d}t}\rho_{10}^*.\end{aligned}$$

From these differential equations, we can directly see that the populations are uncoupled from the coherences. To solve the above equations, we first look at the transformed correlation functions, which we find from Eqs. (2.32) and (2.33) to be

$$\begin{aligned}\gamma^< &= \Gamma^{\mathrm{L/R}} \cdot \left(f^{\mathrm{L}}(\varepsilon) + f^{\mathrm{R}}(\varepsilon)\right), \\ \gamma^> &= \Gamma^{\mathrm{L/R}} \cdot \left(2 - f^{\mathrm{L}}(\varepsilon) - f^{\mathrm{R}}(\varepsilon)\right),\end{aligned}$$

where we assumed $\Gamma^{\mathrm{L}} = \Gamma^{\mathrm{R}}$. Using the above, we find a simple expression for the steady state of ρ_{S},

$$\rho_{00}^{\mathrm{ss}} = 1 - \frac{1}{2}\left(f^{\mathrm{L}}(\varepsilon) + f^{\mathrm{R}}(\varepsilon)\right) = 1 - \rho_{11}^{\mathrm{ss}}.$$

Finally, we calculate the electric current through the system using Eq. (2.41),

$$\langle I_{\mathrm{L}} \rangle = \frac{\mathrm{e}\Gamma^{\mathrm{L/R}}}{\hbar} \Big(f^{\mathrm{L}}(\varepsilon) + \rho_{00} - 1 \Big) ,$$
$$\langle I_{\mathrm{R}} \rangle = \frac{\mathrm{e}\Gamma^{\mathrm{L/R}}}{\hbar} \Big(f^{\mathrm{R}}(\varepsilon) + \rho_{00} - 1 \Big) ,$$

and we insert the steady-state solution for ρ_{00} to get the steady-state currents,

$$\langle I \rangle^{\mathrm{ss}} = \langle I_{\mathrm{L}} \rangle^{\mathrm{ss}} = \frac{\mathrm{e}\Gamma^{\mathrm{L/R}}}{2\hbar} \Big(f^{\mathrm{L}}(\varepsilon) - f^{\mathrm{R}}(\varepsilon) \Big) = -\langle I_{\mathrm{R}} \rangle^{\mathrm{ss}} .$$

As the maximum difference between the two Fermi functions is 1, the maximum possible current is $\mathrm{e}\Gamma^{\mathrm{L/R}}/2\hbar$.

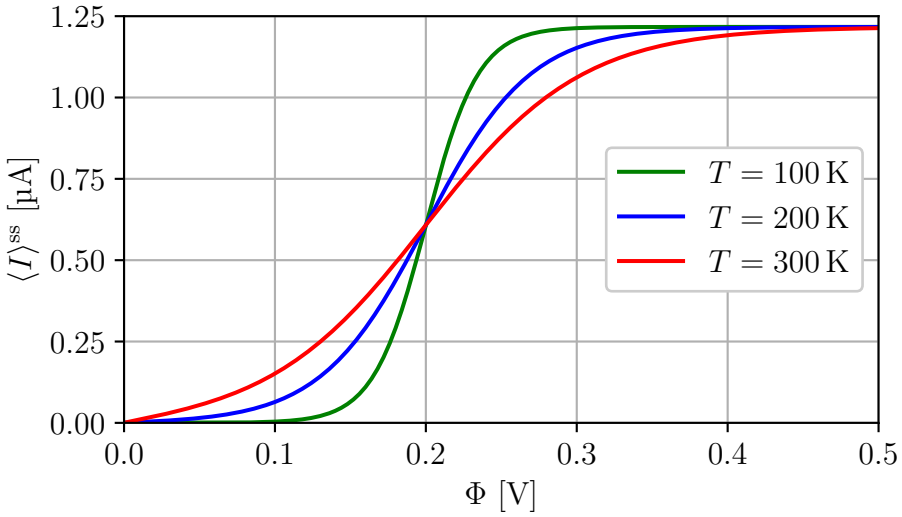

Figure 2.2: Current-voltage characteristics of a resonant level model with $\varepsilon = 100\,\mathrm{meV}$, $\Gamma^{\mathrm{L}} = \Gamma^{\mathrm{R}} = 10\,\mathrm{meV}$.

Fig. 2.2 depicts the steady-state current for an example set of parameters: $\varepsilon = 100\,\mathrm{meV}$, $\Gamma^{\mathrm{L/R}} = 10\,\mathrm{meV}$. It can be seen that the current initially vanishes at $\Phi = 0$, as it should be. For $\Phi > 0$, it increases in a step-like shape; the center of the step lies at $\Phi = 0.2\,\mathrm{V}$. For large bias voltage $\Phi > 0.4\,\mathrm{V}$, the current approaches its maximum value of $\mathrm{e}\Gamma^{\mathrm{L/R}}/2\hbar$, which evaluates to $1.217\,\mu\mathrm{A}$ for the parameters chosen.

To understand the behavior of the current, we examine the energy level diagram depicted in Fig. 2.3. In Fig. 2.3**(a)**, we can see that at zero bias voltage, the chemical potentials of the electrodes are well below the energy level ε of the nanosystem. Thus, even with the broadening of the Fermi functions due to finite temperature taken into account, there is no charge transport between the electrodes and the nanosystem, and the current is zero. When the bias voltage is increased, electron transport becomes possible as the chemical potential, μ_{L}, surpasses the energy level ε of the nanosystem, as depicted in Fig. 2.3**(b)**. This is because energy levels $\geq \varepsilon$ become occupied in the left lead. Due to the finite temperatures considered here, the Fermi functions of the electrodes are broadened, and the current increases gradually as the region where the Fermi function of the left electrode changes from 0 to 1 surpasses the energy ε. In

Fig. 2.3**(c)**, we see the situation for much higher bias voltage. The chemical potential of the left electrode and the associated step in the Fermi function are now well above ε, such that electron transport is now possible from an extensive range of initial energy levels in the left electrode. The current, however, saturates to a finite value because of the finite coupling $\Gamma^{\mathrm{L/R}}$.

Note that for $T = 100\,\mathrm{K}$, we have $k_\mathrm{B}T \approx 8\,\mathrm{meV} < \Gamma^{\mathrm{L/R}}$. Hence, the validity of the curve for 100 K is questionable according to our discussion in Sec. 2.2.4. It is shown here for illustrative purposes only. In the following, we will usually consider $k_\mathrm{B}T = 26\,\mathrm{meV}$, corresponding to $T \approx 300\,\mathrm{K}$, and $\Gamma^{\mathrm{L/R}} \leq 10\,\mathrm{meV}$ to ensure that the Born-Markov approximation is satisfied.

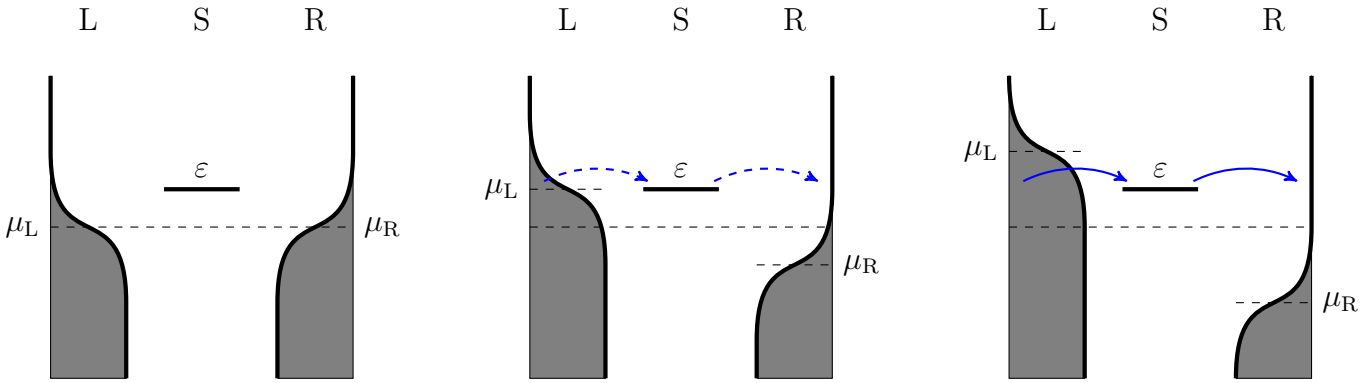

(a) $\Phi = 0$. **(b)** $\Phi = 2\varepsilon/\mathrm{e}$. **(c)** $\Phi > 2\varepsilon/\mathrm{e}$.

Figure 2.3: Energy level scheme for the resonant level model. At zero bias voltage, depicted in **(a)**, the chemical potentials of the electrodes are well below the energy level ε of the system; therefore, no charge transport is possible. When the bias voltage is increased, electron transport becomes possible as the chemical potential of the left electrode surpasses the energy level of the system, that is $\mu_\mathrm{L} = \varepsilon$ corresponding to $\Phi = 2\varepsilon/\mathrm{e}$, depicted in **(b)**. For higher bias voltage, electron transport can occur from an extensive range of initial energy levels in the left electrode, and the resulting current saturates, depicted in **(c)**.

2.3.2 Anderson impurity model - How to incorporate electron spin

In this section, we investigate the effect of including the electron spin. For this, we consider the Anderson impurity model [48], which comprises a nanosystem with one electronic level that can be occupied by two electrons of different spin. To describe this level, two separate sets of creation and annihilation operators, $d_\uparrow^{(\dagger)}$ and $d_\downarrow^{(\dagger)}$, are used. Additionally, we include an interaction energy U between the two electrons. The system Hamiltonian H_S is

$$H_\mathrm{S} = \sum_{s\in\{\uparrow,\downarrow\}} \varepsilon_s d_s^\dagger d_s + U d_\uparrow^\dagger d_\uparrow d_\downarrow^\dagger d_\downarrow.$$

We do not require $\varepsilon_\uparrow = \varepsilon_\downarrow$, such that our following calculations also allow considering a system that is spin-split, for example, due to an external magnetic field. We do not incorporate spin flipping.

Like the nanosystem, we also have to treat the electrodes including spin. We assume that no interactions exist between the different spin states in the electrodes. As a result, we effectively have four different electrodes, one spin-$\uparrow$ and one spin-$\downarrow$ on each of the two sides,

$$H_\mathrm{B} = H_{\mathrm{L}\uparrow} + H_{\mathrm{L}\downarrow} + H_{\mathrm{R}\uparrow} + H_{\mathrm{R}\downarrow} = \sum_{K\in\{\mathrm{L},\mathrm{R}\}} \sum_{s\in\{\uparrow,\downarrow\}} \sum_{k_K} \varepsilon_{k_K,s} c_{k_K,s}^\dagger c_{k_K,s},$$

where we set the chemical potentials and temperatures equal on each side,

$$\mu_{K\uparrow} = \mu_{K\downarrow} =: \mu_K, \qquad T_{K\uparrow} = T_{K\downarrow} =: T, \qquad K \in \{\mathrm{L},\mathrm{R}\}.$$

Interactions between the system and electrodes occur only between levels of the same spin orientation, and we assume the coupling constants are for the two spin states. Thus, the interaction Hamiltonian takes the form

$$\begin{aligned} H_\mathrm{SB} &= -d_\uparrow \cdot \Big(\sum_K \sum_{k_K} V c_{k_K\uparrow}^\dagger\Big) - d_\downarrow \cdot \Big(\sum_K \sum_{k_K} V c_{k_K\downarrow}^\dagger\Big) \\ &\quad + d_\uparrow^\dagger \cdot \Big(\sum_K \sum_{k_K} V^* c_{k_K\uparrow}\Big) + d_\downarrow^\dagger \cdot \Big(\sum_K \sum_{k_K} V^* c_{k_K\downarrow}\Big) \\ &=: -d_\uparrow B_\uparrow^\dagger - d_\downarrow B_\downarrow^\dagger + d_\uparrow^\dagger B_\uparrow + d_\downarrow^\dagger B_\downarrow. \end{aligned}$$

We start from the BMME in Eq. (2.30) to derive the specific master equation for this system. First, we note that $\gamma_{ij}^{\lessgtr}(\omega) = 0 = S_{ij}^{\lessgtr}(\omega)$ for $i \neq j$ because there is no coupling between the different spin orientations. Thus, the double sum over i and j reduces to a single sum. Furthermore, we find

$$\begin{aligned} \gamma_{\uparrow\uparrow}^{\lessgtr}(\omega) = \gamma_{\downarrow\downarrow}^{\lessgtr}(\omega) =: \gamma^{\lessgtr}(\omega), \\ S_{\uparrow\uparrow}^{\lessgtr}(\omega) = S_{\downarrow\downarrow}^{\lessgtr}(\omega) =: S^{\lessgtr}(\omega), \end{aligned}$$

because we set the chemical potentials, temperatures, and couplings equal for both spin orientations. The system Hamiltonian H_S is already in diagonal form; hence, we can easily read off the possible energy differences $\hbar\omega \in \{\varepsilon_\uparrow, \varepsilon_\downarrow, U+\varepsilon_\uparrow, U+\varepsilon_\downarrow\}$. Using

the Fock basis states, defined by

$$
\begin{aligned}
d_\uparrow^\dagger |0\rangle &= |\uparrow\rangle\,, & d_\downarrow^\dagger |0\rangle &= |\downarrow\rangle\,,\\
d_\uparrow^\dagger |\downarrow\rangle &= |\uparrow\downarrow\rangle\,, & d_\downarrow^\dagger |\uparrow\rangle &= |\downarrow\uparrow\rangle = -|\uparrow\downarrow\rangle\,,
\end{aligned}
$$

we find the following non-vanishing frequency-projected operators,

$$
\begin{aligned}
d_\uparrow(\varepsilon_\uparrow) &= |0\rangle\langle\uparrow|\,, & d_\uparrow(U+\varepsilon_\uparrow) &= -|\downarrow\rangle\langle\uparrow\downarrow|\,,\\
d_\downarrow(\varepsilon_\downarrow) &= |0\rangle\langle\downarrow|\,, & d_\downarrow(U+\varepsilon_\downarrow) &= |\uparrow\rangle\langle\uparrow\downarrow|\,,
\end{aligned}
$$

and all others vanish. Note that other than in Eq. (2.18), we use the energy difference $\hbar\omega$ as the argument of the frequency projected operators here instead of the frequency ω, to avoid writing $\frac{1}{\hbar}$ everywhere. With these, we find the master equation to be

$$
\begin{aligned}
\frac{\mathrm{d}}{\mathrm{d}t}\rho_\mathrm{S}(t) = -\frac{\mathrm{i}}{\hbar}\left[H_\mathrm{S} + H_\mathrm{LS}, \rho_\mathrm{S}(t)\right]
&+ \frac{1}{\hbar}\Big\{ \Big(|\uparrow\rangle\langle 0|\,\rho_\mathrm{S}(t)\,|0\rangle\langle\uparrow| - \frac{1}{2}\Big\{ |0\rangle\langle 0|\,, \rho_\mathrm{S}(t)\Big\}\Big)\cdot\gamma^<(\varepsilon_\uparrow)\\
&\quad + \Big(|0\rangle\langle\uparrow|\,\rho_\mathrm{S}(t)\,|\uparrow\rangle\langle 0| - \frac{1}{2}\Big\{ |\uparrow\rangle\langle\uparrow|\,, \rho_\mathrm{S}(t)\Big\}\Big)\cdot\gamma^>(\varepsilon_\uparrow)\\
&\quad + \Big(|\uparrow\downarrow\rangle\langle\downarrow|\,\rho_\mathrm{S}(t)\,|\downarrow\rangle\langle\uparrow\downarrow| - \frac{1}{2}\Big\{ |\downarrow\rangle\langle\downarrow|\,, \rho_\mathrm{S}(t)\Big\}\Big)\cdot\gamma^<(\varepsilon_\uparrow + U)\\
&\quad + \Big(|\downarrow\rangle\langle\uparrow\downarrow|\,\rho_\mathrm{S}(t)\,|\uparrow\downarrow\rangle\langle\downarrow| - \frac{1}{2}\Big\{ |\uparrow\downarrow\rangle\langle\uparrow\downarrow|\,, \rho_\mathrm{S}(t)\Big\}\Big)\cdot\gamma^>(\varepsilon_\uparrow + U)\\
&\quad + \Big(|\downarrow\rangle\langle 0|\,\rho_\mathrm{S}(t)\,|0\rangle\langle\downarrow| - \frac{1}{2}\Big\{ |0\rangle\langle 0|\,, \rho_\mathrm{S}(t)\Big\}\Big)\cdot\gamma^<(\varepsilon_\downarrow)\\
&\quad + \Big(|0\rangle\langle\downarrow|\,\rho_\mathrm{S}(t)\,|\downarrow\rangle\langle 0| - \frac{1}{2}\Big\{ |\downarrow\rangle\langle\downarrow|\,, \rho_\mathrm{S}(t)\Big\}\Big)\cdot\gamma^>(\varepsilon_\downarrow)\\
&\quad + \Big(|\uparrow\downarrow\rangle\langle\uparrow|\,\rho_\mathrm{S}(t)\,|\uparrow\rangle\langle\uparrow\downarrow| - \frac{1}{2}\Big\{ |\uparrow\rangle\langle\uparrow|\,, \rho_\mathrm{S}(t)\Big\}\Big)\cdot\gamma^<(\varepsilon_\downarrow + U)\\
&\quad + \Big(|\uparrow\rangle\langle\uparrow\downarrow|\,\rho_\mathrm{S}(t)\,|\uparrow\downarrow\rangle\langle\uparrow| - \frac{1}{2}\Big\{ |\uparrow\downarrow\rangle\langle\uparrow\downarrow|\,, \rho_\mathrm{S}(t)\Big\}\Big)\cdot\gamma^>(\varepsilon_\downarrow + U)\Big\}.
\end{aligned}
$$

Since both the system Hamiltonian H_S and the Lamb shift H_LS are diagonal in the Fock basis, we find no coupling between the diagonal and off-diagonal values of $\rho_\mathrm{S}(t)$. For the diagonal elements, $\rho_{ii} := \langle i|\rho_\mathrm{S}(t)|i\rangle$, we get the following closed equations of motion

$$
\begin{aligned}
\hbar\cdot\dot\rho_{00} &= -\Big(\gamma^<(\varepsilon_\uparrow) + \gamma^<(\varepsilon_\downarrow)\Big)\,\rho_{00} + \gamma^>(\varepsilon_\uparrow)\rho_{\uparrow\uparrow} + \gamma^>(\varepsilon_\downarrow)\rho_{\downarrow\downarrow},\\
\hbar\cdot\dot\rho_{\uparrow\uparrow} &= -\Big(\gamma^>(\varepsilon_\uparrow) + \gamma^<(\varepsilon_\downarrow + U)\Big)\,\rho_{\uparrow\uparrow} + \gamma^<(\varepsilon_\uparrow)\rho_{00} + \gamma^>(\varepsilon_\downarrow + U)\rho_{\uparrow\downarrow\uparrow\downarrow},\\
\hbar\cdot\dot\rho_{\downarrow\downarrow} &= -\Big(\gamma^>(\varepsilon_\downarrow) + \gamma^<(\varepsilon_\uparrow + U)\Big)\,\rho_{\downarrow\downarrow} + \gamma^<(\varepsilon_\downarrow)\rho_{00} + \gamma^>(\varepsilon_\uparrow + U)\rho_{\uparrow\downarrow\uparrow\downarrow},\\
\hbar\cdot\dot\rho_{\uparrow\downarrow\uparrow\downarrow} &= -\Big(\gamma^>(\varepsilon_\uparrow + U) + \gamma^>(\varepsilon_\downarrow + U)\Big)\,\rho_{\uparrow\downarrow\uparrow\downarrow} + \gamma^<(\varepsilon_\uparrow + U)\rho_{\downarrow\downarrow} + \gamma^<(\varepsilon_\downarrow + U)\rho_{\uparrow\uparrow},
\end{aligned}
\tag{2.44}
$$

which obey $\frac{\mathrm{d}}{\mathrm{d}t}\,\mathrm{tr}_\mathrm{S}\{\rho_\mathrm{S}(t)\} = 0$ as expected. By requiring $\dot\rho_{ii} = 0$, we can solve for the steady state, $\rho_\mathrm{S}^\mathrm{ss}$. The result is given in Eq. (E.1) in Appendix E.

In the next step, we use Eq. (2.41) to calculate the electric current through the system. Here, the left and right currents are the sum of the respective spin-↑ and

spin-↓ currents,

$$\begin{aligned}\langle I_K\rangle = \langle I_{K\uparrow}\rangle + \langle I_{K\downarrow}\rangle = \frac{\mathrm{e}}{\hbar}\Big[&\rho_{00}\Big(\gamma^{<,K}(\varepsilon_\uparrow) + \gamma^{<,K}(\varepsilon_\downarrow)\Big)\\ &+ \rho_{\uparrow\uparrow}\Big(\gamma^{<,K}(\varepsilon_\downarrow + U) - \gamma^{>,K}(\varepsilon_\uparrow)\Big)\\ &+ \rho_{\downarrow\downarrow}\Big(\gamma^{<,K}(\varepsilon_\uparrow + U) - \gamma^{>,K}(\varepsilon_\downarrow)\Big)\\ &- \rho_{\uparrow\downarrow\uparrow\downarrow}\Big(\gamma^{>,K}(\varepsilon_\uparrow + U) + \gamma^{>,K}(\varepsilon_\downarrow + U)\Big)\Big],\end{aligned}$$

where the transformed correlation functions are given by

$$\begin{aligned}\gamma^{<,K}(\varepsilon) &= \Gamma^K\left(f^{K\uparrow}(\varepsilon) + f^{K\downarrow}(\varepsilon)\right),\\ \gamma^{>,K}(\varepsilon) &= \Gamma^K\left(2 - f^{K\uparrow}(\varepsilon) - f^{K\downarrow}(\varepsilon)\right),\end{aligned}$$

following Eqs. (2.32) and (2.33), where we used $\Gamma^{K\uparrow} = \Gamma^{K\downarrow} =: \Gamma^K$.

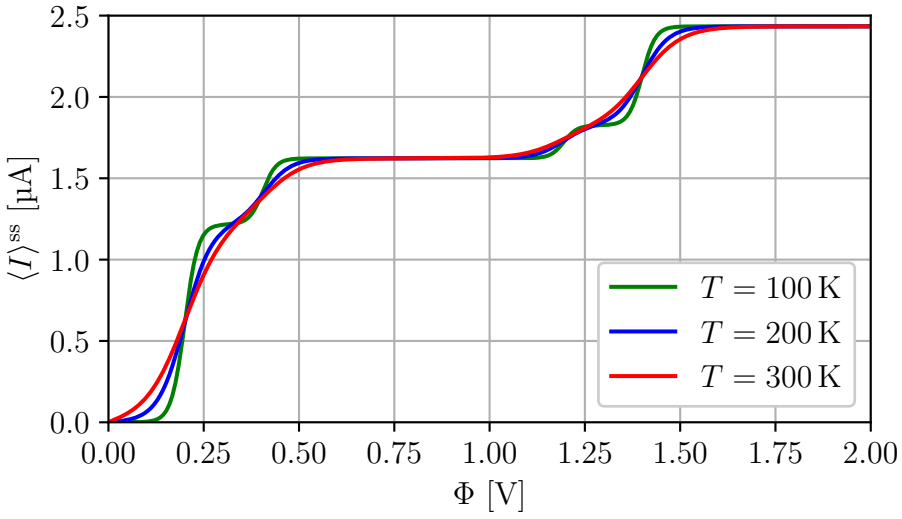

Figure 2.4: Current-voltage characteristics of a spin-split Anderson impurity model with $\varepsilon_\uparrow = 100\,\mathrm{meV}$, $\varepsilon_\downarrow = 200\,\mathrm{meV}$, $U = 500\,\mathrm{meV}$, $\Gamma^{\mathrm{L}} = \Gamma^{\mathrm{R}} = 10\,\mathrm{meV}$.

Fig. 2.4 depicts the steady-state current for a spin-split Anderson impurity model with the following parameters: $\varepsilon_\uparrow = 100\,\mathrm{meV}$, $\varepsilon_\downarrow = 200\,\mathrm{meV}$, $U = 500\,\mathrm{meV}$, $\Gamma^{\mathrm{L/R}} = 10\,\mathrm{meV}$. As expected, the current initially vanishes at $\Phi = 0$. As the bias voltage is increased, the current increases in a series of four distinct steps to the maximum value of $\mathrm{e}\Gamma^{\mathrm{L/R}}/\hbar = 2.434\,\mu\mathrm{A}$, which is twice the current of the resonant level model with the same coupling $\Gamma^{\mathrm{L/R}}$ discussed in the previous section. With higher temperatures, the current steps are increasingly broadened, which makes the distinction more difficult; hence, for illustrative purposes, we have again depicted also the case $T = 100\,\mathrm{K}$, although $k_{\mathrm{B}}T \approx 8\,\mathrm{meV} < \Gamma^{\mathrm{L/R}}$ there.

To understand the emergence of the four steps in the current, we consider the energy level diagram shown in Fig. 2.5. In Fig. 2.5**(a)**, we find that at zero bias voltage the chemical potentials are well below the energy levels of the Anderson system; thus, no charge transport occurs between the electrodes and the system. As the bias voltage is increased, the chemical potential of the left electrode, $\mu_{\mathrm{L}} = \mathrm{e}\Phi/2$, increases and

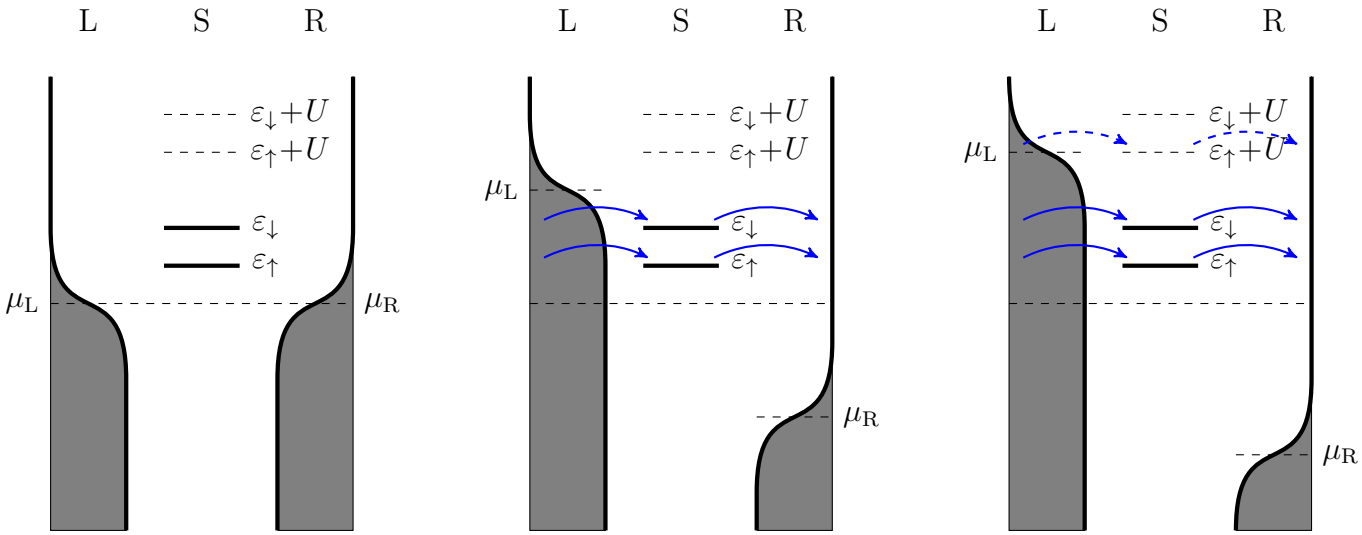

(a) $\Phi = 0$. **(b)** $\Phi > 2\varepsilon_\downarrow/\mathrm{e}$. **(c)** $\Phi = 2(\varepsilon_\uparrow + U)/\mathrm{e}$.

Figure 2.5: Energy level scheme for the spin-split Anderson impurity model. At zero bias voltage, depicted in **(a)**, the chemical potentials of the electrodes are well below the energy levels of the nanosystem; therefore, no charge transport is possible. When the bias voltage is large enough that the chemical potential of the left electrode is above the energy levels $\varepsilon_\uparrow$ and $\varepsilon_\downarrow$, as depicted in **(b)**, transport of spin-↑ and spin-↓ electrons through the junction is possible, though only if no electron with opposite spin resides in the system. Only when the bias voltage is so large that the chemical potential of the left electrode also surpasses $\mu_\mathrm{L} = \varepsilon_\uparrow + U$, as indicated in **(c)**, transport of spin-↑ electrons through the junction becomes possible even if a spin-↓ electron resides in the system, leading to a further increase in the current.

surpasses the energies $\varepsilon_\uparrow$ and $\varepsilon_\downarrow$, as indicated in Fig. 2.5**(b)**. When this happens, spin-↑ and spin-↓ electron transport from the left electrode via the system to the right electrode becomes possible, leading to an increase in the current. As we consider a spin-split system here, $\varepsilon_\uparrow \neq \varepsilon_\downarrow$, this happens at two different bias voltages for spin-↑ and spin-↓, $\Phi = 2\varepsilon_\uparrow/\mathrm{e} = 0.2\,\mathrm{V}$ and $\Phi = 2\varepsilon_\downarrow/\mathrm{e} = 0.4\,\mathrm{V}$, respectively, creating the first two steps in the current. Due to the broadening of the Fermi functions of the electrodes, the steps in the current become broadened as well for increased temperature, until they eventually merge into one large step, as can be seen for $T = 300\,\mathrm{K}$ in Fig. 2.4. It is worth noting that while the step corresponding to the lower energy level, $\varepsilon_\uparrow$ in this case, has a magnitude of $1.217\,\mu\mathrm{A}$, similar to the resonant level discussed in Sec. 2.3.1, the step corresponding to the higher level, $\varepsilon_\downarrow$, has much smaller magnitude. This is due to the interaction energy U, which prevents simultaneous occupation of spin-↑ and spin-↓ at these bias voltages and thereby results in the transport of spin-↑ and spin-↓ electrons not occurring independently. This phenomenon is called the *Coulomb blockade* [48].

If the bias voltage is increased further, the chemical potential of the left electrode surpasses $\mu_\mathrm{L} = \varepsilon_\uparrow + U$, as indicated in Fig. 2.5**(c)**, which happens at $\Phi = 2(\varepsilon_\uparrow + U)/\mathrm{e} = 1.2\,\mathrm{V}$ here. At this point, the additional transport of spin-↑ electrons through the junction while the spin-↓ level stays occupied throughout the process becomes possible, leading to a further increase in the current. Eventually, at an even higher voltage, the

chemical potential also surpasses $\mu_\mathrm{L} = \varepsilon_\downarrow + U$, enabling the transport of spin-↓ electrons through the junction while the spin-↑ state remains occupied, causing another increase in the current. After this point, the transport of spin-↑ and spin-↓ electrons may occur independently because the doubly-occupied state is no longer energetically forbidden. Thus, the maximum current reached is exactly twice that of a resonant level model with the same electrode coupling.

Fig. 2.6 shows the electric currents for a spin-degenerate level with strong electron-electron interaction: $\varepsilon_\uparrow = \varepsilon_\downarrow = 100\,\mathrm{meV}$, $U = 10\,\mathrm{eV}$, $\Gamma^\mathrm{L} = \Gamma^\mathrm{R} = 10\,\mathrm{meV}$. Here, the current steps of the two singly-occupied states now coincide, and the large U shifts the further current steps to a very high bias voltage of $> 20\,\mathrm{V}$. For comparison, we also include the current-voltage characteristics of a resonant level model (RLM) with a larger electrode coupling, $\Gamma^\mathrm{L/R}_\mathrm{RLM} = \frac{4}{3} \cdot \Gamma^\mathrm{L/R}_\mathrm{Anderson}$. It can be seen that the curves of the Anderson model and resonant level are very similar. However, the current of the Anderson model increases slightly faster, reaching, at $\Phi = 0.2\,\mathrm{V}$, already more than half of its value at $\Phi = 0.5\,\mathrm{V}$. In contrast, the current of the resonant level is almost symmetrical around $\Phi = 0.2\,\mathrm{V}$, reaching exactly half its maximum value there. This is because the Anderson junction has two channels for charge transport at the indicated bias voltages, spin-↑ and spin-↓, while the resonant level has only one channel, which is also why a higher electrode coupling is necessary for it to obtain the same current. For our purposes, however, this difference is not relevant. Therefore, we neglect the effect of electron spin in the following chapters for simplicity.

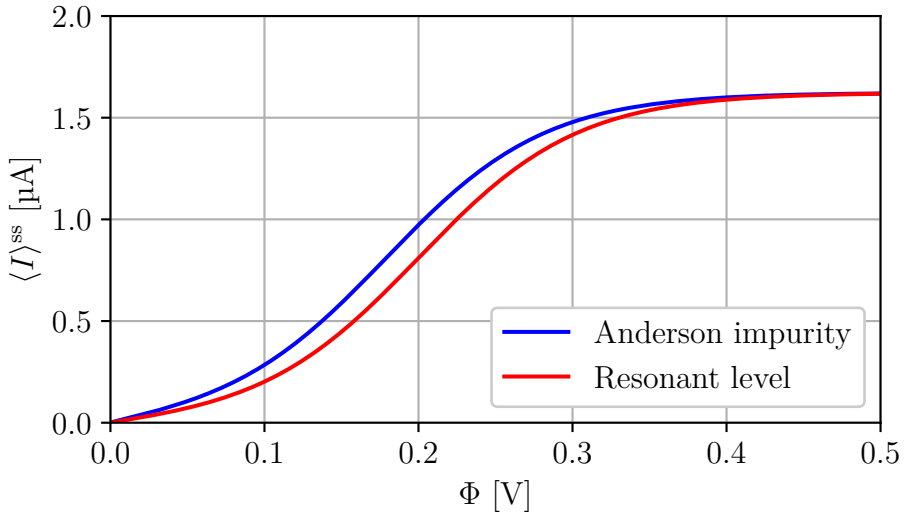

Figure 2.6: Comparison of the current-voltage characteristics of a spin-degenerate Anderson impurity and a resonant level model (RLM) with $\varepsilon_\uparrow = \varepsilon_\downarrow = \varepsilon_\mathrm{RLM} = 100\,\mathrm{meV}$, $\Gamma^\mathrm{L/R}_\mathrm{Anderson} = 10\,\mathrm{meV}$, $\Gamma^\mathrm{L/R}_\mathrm{RLM} = \frac{4}{3} \cdot \Gamma^\mathrm{L/R}_\mathrm{Anderson}$, $k_\mathrm{B}T = 26\,\mathrm{meV}$.

2.4 Semi-classical theory: electronic friction

In Sec. 2.1, we introduced our model of a molecular junction, consisting of a central molecule or similar nanosystem coupled to a left and right electrode. In Sec. 2.2, we derived a Born-Markov master equation for the model, which allows us to determine the quantum-mechanical time evolution of the nanosystem in closed form by statistically accounting for the infinite degrees of freedom of the outer electrodes. What remains complicated, however, are vibrational modes in the nanosystem itself. Since a vibrational mode can be excited to an arbitrary degree, its Hilbert space is theoretically infinite. In practice, of course, a finite number of basis states is sufficient, as we will see in more detail in Sec. 3.2. Nevertheless, considering a correspondingly large number of basis states is costly, especially when several vibrational modes are studied, since the dimension of the system Hilbert space is given by the product of the dimensions of the subspaces. To circumvent this problem, in this section, we will approximate our fully quantum-mechanical description of the molecular junction with a semi-classical description of its vibrational modes.

2.4.1 Mass- and time-scale separation

Vibrational modes in molecular nanosystems are typically stretching and bending vibrations of single atoms, or pairs or groups of a few atoms. The reduced mass of the vibrating system is, therefore, in the range of a few Dalton. The mass of the electrons, which represent the fermionic degrees of freedom of the nanosystem and electrodes, is much smaller in comparison, $m_\mathrm{e} \approx 5.5 \cdot 10^{-4}\,\mathrm{Da}$ [49]. We have, therefore, a mass-scale separation between the heavy, vibrating atoms and the light electrons. This mass-scale separation often leads to a time-scale separation of the slow vibrational dynamics from the fast electron transport dynamics. We can take advantage of this time-scale separation by approximating the slow vibrational dynamics semi-classically and treating only the fast dynamics of the electrons fully quantum-mechanically, thus avoiding the problem of large vibrational Hilbert spaces.

To achieve this, the physical literature offers a variety of different methods, including Ehrenfest dynamics [34, 35], surface hopping [36], and quantum-classical Liouville equations [37]. In the following, we use the theory of electronic friction [30, 38–40], which is derived from a partial Wigner transform in the vibration degrees of freedom, similar to quantum-classical Liouville equations.

2.4.2 Partial Wigner transform and Langevin equation

In this section, we derive a semi-classical description of our model by applying a partial Wigner transform in the vibrational degrees of freedom and expanding up to zeroth order in $\hbar$. In doing so, we follow the derivations given in Sec. II of [37], Sec. II of [30], and Appendix I.B of [39]. Our starting point for the derivation is the BMME in Eq. (2.30), which we split as follows,

$$\frac{\mathrm{d}}{\mathrm{d}t}\rho_\mathrm{S}(t) = -\frac{\mathrm{i}}{\hbar}\Big[H_\mathrm{S}, \rho_\mathrm{S}(t)\Big] + \mathcal{D}\Big(\rho_\mathrm{S}(t)\Big), \tag{2.45}$$

where the function $\mathcal{D}$ contains the Lamb shift contribution and the dissipative part of the master equation. In the following, $\hat{x}_\alpha$ and $\hat{p}_\alpha$ denote the position and momentum operators of low-frequency vibrational degrees of freedom, which we seek to describe

semi-classically, and $\hat{\mathbf{x}} = (\hat{x}_1, ..., \hat{x}_N)$, $\hat{\mathbf{p}} = (\hat{p}_1, ..., \hat{p}_N)$. The explicit notation $\hat{\square}$ for the vibrational operators is used to distinguish them from the later classical coordinates. With this notation, we divide the system Hamiltonian, H_{S}, into two parts,

$$H_{\mathrm{S}} = H_{\mathrm{rS}}(\hat{\mathbf{x}}) + \sum_{\alpha} \frac{\hat{p}_\alpha^2}{2m_\alpha}, \tag{2.46}$$

where the first part, the *reduced* system Hamiltonian H_{rS}, contains all the electronic operators as well as the vibrational coupling and potentials of the low-frequency modes. The second part is the vibrational kinetic energies. Note that H_{rS} may also entail additional high-frequency vibrations whose dynamics take place on the order of the electron transport, and as such, do not interfere with the time-scale separation to the low-frequency vibrations.

Before we perform the partial Wigner transform, we rewrite Eq. (2.45) in the $\mathbf{x}$ representation, where $\mathbf{x} = (x_1, ..., x_N)$. Using $\mathbb{1} = \int \mathrm{d}\mathbf{x}\, |\mathbf{x}\rangle\langle\mathbf{x}|$, we get

$$\begin{aligned}\frac{\partial}{\partial t}\langle\mathbf{x}|\rho_{\mathrm{S}}(t)|\mathbf{x}'\rangle = -\frac{\mathrm{i}}{\hbar}\int \mathrm{d}\mathbf{x}''\, \Big(\langle\mathbf{x}|H_{\mathrm{S}}|\mathbf{x}''\rangle\langle\mathbf{x}''|\rho_{\mathrm{S}}(t)|\mathbf{x}'\rangle - \langle\mathbf{x}|\rho_{\mathrm{S}}(t)|\mathbf{x}''\rangle\langle\mathbf{x}''|H_{\mathrm{S}}|\mathbf{x}'\rangle\Big) \\ + \mathcal{D}\Big(\langle\mathbf{x}|\rho_{\mathrm{S}}(t)|\mathbf{x}'\rangle\Big),\end{aligned} \tag{2.47}$$

where we have used $\langle\mathbf{x}|\mathcal{D}(\rho_{\mathrm{S}}(t))|\mathbf{x}'\rangle = \mathcal{D}(\langle\mathbf{x}|\rho_{\mathrm{S}}(t)|\mathbf{x}'\rangle)$, which follows from the fact that $\mathcal{D}$ does not contain any vibrational operators. Furthermore, we have

$$\langle\mathbf{x}|H_{\mathrm{S}}|\mathbf{x}'\rangle = \Big(H_{\mathrm{rS}}(\mathbf{x}) - \sum_{\alpha}\frac{\hbar^2}{2m_\alpha}\frac{\partial^2}{\partial x_\alpha^2}\Big)\delta(\mathbf{x}-\mathbf{x}'), \tag{2.48}$$

where we used $\langle\mathbf{x}|H_{\mathrm{rS}}(\hat{\mathbf{x}})|\mathbf{x}'\rangle = H_{\mathrm{rS}}(\mathbf{x})\,\delta(\mathbf{x}-\mathbf{x}')$.

At this point, we perform the partial Wigner transform with respect to the vibrational coordinates. For a general operator A, the transform is defined as

$$A^{\mathrm{w}}(\mathbf{x},\mathbf{p}) = \int \mathrm{d}\mathbf{z}\, e^{\mathrm{i}\mathbf{p}\cdot\mathbf{z}/\hbar}\,\langle\mathbf{x}-\frac{\mathbf{z}}{2}|A|\mathbf{x}+\frac{\mathbf{z}}{2}\rangle = \int \mathrm{d}\mathbf{z}\, e^{-\mathrm{i}\mathbf{p}\cdot\mathbf{z}/\hbar}\,\langle\mathbf{x}+\frac{\mathbf{z}}{2}|A|\mathbf{x}-\frac{\mathbf{z}}{2}\rangle\,.$$

Using Eq. (2.48), we find the Wigner transform of the system Hamiltonian,

$$H_{\mathrm{S}}^{\mathrm{w}}(\mathbf{x},\mathbf{p}) = \int \mathrm{d}\mathbf{z}\, e^{\mathrm{i}\mathbf{p}\cdot\mathbf{z}/\hbar}\,\langle\mathbf{x}-\frac{\mathbf{z}}{2}|H_{\mathrm{S}}|\mathbf{x}+\frac{\mathbf{z}}{2}\rangle = H_{\mathrm{rS}}(\mathbf{x}) + \sum_{\alpha}\frac{p_\alpha^2}{2m_\alpha}. \tag{2.49}$$

For the density matrix, the Wigner transform is analogous, but we have to add the normalization factor $1/h^N$,

$$\rho_{\mathrm{S}}^{\mathrm{w}}(\mathbf{x},\mathbf{p},t) = \frac{1}{h^N}\int \mathrm{d}\mathbf{z}\, e^{\mathrm{i}\mathbf{p}\cdot\mathbf{z}/\hbar}\,\langle\mathbf{x}-\frac{\mathbf{z}}{2}|\rho_{\mathrm{S}}(t)|\mathbf{x}+\frac{\mathbf{z}}{2}\rangle\,.$$

Note that $(\mathbf{x},\mathbf{p})$ above are variables, not operators. To transform Eq. (2.47), we also need the partial Wigner transform of a product of operators [37],

$$(AB)^{\mathrm{w}}(\mathbf{x},\mathbf{p}) = A^{\mathrm{w}}(\mathbf{x},\mathbf{p})e^{\hbar\Lambda/2\mathrm{i}}B^{\mathrm{w}}(\mathbf{x},\mathbf{p}),$$

where the Poisson bracket operator Λ is defined as

$$\Lambda = \overleftarrow{\nabla}_{\mathbf{p}}\cdot\overrightarrow{\nabla}_{\mathbf{x}} - \overleftarrow{\nabla}_{\mathbf{x}}\cdot\overrightarrow{\nabla}_{\mathbf{p}},$$

where the direction of the arrow indicates the direction in which the derivative acts. With this, we find the partial Wigner transform of Eq. (2.47),

$$\frac{\partial}{\partial t}\rho_{\mathrm{S}}^{\mathrm{w}}(\mathbf{x},\mathbf{p},t) = -\frac{\mathrm{i}}{\hbar}\Big(H_{\mathrm{S}}^{\mathrm{w}}(\mathbf{x},\mathbf{p})e^{\hbar\Lambda/2\mathrm{i}}\rho_{\mathrm{S}}^{\mathrm{w}}(\mathbf{x},\mathbf{p},t) - \rho_{\mathrm{S}}^{\mathrm{w}}(\mathbf{x},\mathbf{p},t)e^{\hbar\Lambda/2\mathrm{i}}H_{\mathrm{S}}^{\mathrm{w}}(\mathbf{x},\mathbf{p})\Big) + \mathcal{D}\Big(\rho_{\mathrm{S}}^{\mathrm{w}}(\mathbf{x},\mathbf{p},t)\Big).$$

Expanding the above exponentials, we obtain

$$\begin{aligned}\frac{\mathrm{i}}{\hbar}H_{\mathrm{S}}^{\mathrm{w}}e^{\hbar\Lambda/2\mathrm{i}}\rho_{\mathrm{S}}^{\mathrm{w}} &= \frac{\mathrm{i}}{\hbar}H_{\mathrm{S}}^{\mathrm{w}}\left[\mathbb{1} + \sum_{n=1}^{\infty}\frac{1}{n!}\left(\frac{\hbar}{2\mathrm{i}}\right)^n\left(\overleftarrow{\nabla}_{\mathbf{p}}\cdot\overrightarrow{\nabla}_{\mathbf{x}} - \overleftarrow{\nabla}_{\mathbf{x}}\cdot\overrightarrow{\nabla}_{\mathbf{p}}\right)^n\right]\rho_{\mathrm{S}}^{\mathrm{w}} \\ &= \frac{\mathrm{i}}{\hbar}H_{\mathrm{S}}^{\mathrm{w}}\rho_{\mathrm{S}}^{\mathrm{w}} + \frac{1}{2}\sum_{\alpha}\left(\frac{\partial H_{\mathrm{S}}^{\mathrm{w}}}{\partial p_\alpha}\frac{\partial\rho_{\mathrm{S}}^{\mathrm{w}}}{\partial x_\alpha} - \frac{\partial H_{\mathrm{S}}^{\mathrm{w}}}{\partial x_\alpha}\frac{\partial\rho_{\mathrm{S}}^{\mathrm{w}}}{\partial p_\alpha}\right) \\ &\quad + \frac{\hbar}{8\mathrm{i}}\sum_{\alpha\beta}\left(\frac{\partial^2 H_{\mathrm{S}}^{\mathrm{w}}}{\partial p_\alpha\partial p_\beta}\frac{\partial^2\rho_{\mathrm{S}}^{\mathrm{w}}}{\partial x_\alpha\partial x_\beta} + \frac{\partial^2 H_{\mathrm{S}}^{\mathrm{w}}}{\partial x_\alpha\partial x_\beta}\frac{\partial^2\rho_{\mathrm{S}}^{\mathrm{w}}}{\partial p_\alpha\partial p_\beta} - 2\frac{\partial^2 H_{\mathrm{S}}^{\mathrm{w}}}{\partial p_\alpha\partial x_\beta}\frac{\partial^2\rho_{\mathrm{S}}^{\mathrm{w}}}{\partial x_\alpha\partial p_\beta}\right) \\ &\quad + \mathcal{O}(\hbar^2),\end{aligned}$$

and vice versa for $H_{\mathrm{S}}^{\mathrm{w}}$ and $\rho_{\mathrm{S}}^{\mathrm{w}}$ exchanged. By virtue of Eq. (2.49), we know that $\frac{\partial^2 H_{\mathrm{S}}^{\mathrm{w}}}{\partial p_\alpha\partial x_\beta} = 0$, and also $\frac{\partial^2 H_{\mathrm{S}}^{\mathrm{w}}}{\partial p_\alpha\partial p_\beta} = 0$ for $\alpha \neq \beta$. Furthermore, we find that $\frac{\partial^2 H_{\mathrm{S}}^{\mathrm{w}}}{\partial p_\alpha^2}$ does not contribute either, because it is just a scalar, and thus cancels with the corresponding term that results from the other exponential. With this, for first and higher order in $\hbar$, only terms proportional to $\frac{\partial^2 H_{\mathrm{S}}^{\mathrm{w}}}{\partial x_\alpha\partial x_\beta}\frac{\partial^2\rho_{\mathrm{S}}^{\mathrm{w}}}{\partial p_\alpha\partial p_\beta}$ are left. In the case of harmonic potentials, $\frac{\partial^2 H_{\mathrm{S}}^{\mathrm{w}}}{\partial x_\alpha\partial x_\beta}$ is a scalar as well; hence, these terms cancel with the corresponding terms resulting from the other exponential, too; leaving only the terms up to zeroth order in $\hbar$. But in the classical limit, the contribution of $\frac{\partial^2 H_{\mathrm{S}}^{\mathrm{w}}}{\partial x_\alpha\partial x_\beta}$ is negligible even for anharmonic potentials [37]. This justifies that we truncate the exponential expansion at zeroth order in $\hbar$,

$$\frac{\mathrm{i}}{\hbar}H_{\mathrm{S}}^{\mathrm{w}}e^{\hbar\Lambda/2\mathrm{i}}\rho_{\mathrm{S}}^{\mathrm{w}} \approx \frac{\mathrm{i}}{\hbar}H_{\mathrm{S}}^{\mathrm{w}}\rho_{\mathrm{S}}^{\mathrm{w}} + \frac{1}{2}\sum_{\alpha}\left(\frac{\partial H_{\mathrm{S}}^{\mathrm{w}}}{\partial p_\alpha}\frac{\partial\rho_{\mathrm{S}}^{\mathrm{w}}}{\partial x_\alpha} - \frac{\partial H_{\mathrm{S}}^{\mathrm{w}}}{\partial x_\alpha}\frac{\partial\rho_{\mathrm{S}}^{\mathrm{w}}}{\partial p_\alpha}\right),$$

and analogously for $H_{\mathrm{S}}^{\mathrm{w}}$ and $\rho_{\mathrm{S}}^{\mathrm{w}}$ exchanged. But note again that, for harmonic potentials, this approximation is, in fact, exact. With this, we arrive at

$$\begin{aligned}\frac{\partial}{\partial t}\rho_{\mathrm{S}}^{\mathrm{w}}(\mathbf{x},\mathbf{p},t) &= \{H_{\mathrm{S}}^{\mathrm{w}}(\mathbf{x},\mathbf{p}),\rho_{\mathrm{S}}^{\mathrm{w}}(\mathbf{x},\mathbf{p},t)\}_a \underbrace{-\frac{\mathrm{i}}{\hbar}\left[H_{\mathrm{S}}^{\mathrm{w}}(\mathbf{x},\mathbf{p}),\rho_{\mathrm{S}}^{\mathrm{w}}(\mathbf{x},\mathbf{p},t)\right] + \mathcal{D}\Big(\rho_{\mathrm{S}}^{\mathrm{w}}(\mathbf{x},\mathbf{p},t)\Big)}_{} \\ &= \{H_{\mathrm{S}}^{\mathrm{w}}(\mathbf{x},\mathbf{p}),\rho_{\mathrm{S}}^{\mathrm{w}}(\mathbf{x},\mathbf{p},t)\}_a + \qquad \mathcal{L}_{\mathrm{S}}^{\mathrm{w}}(\mathbf{x})\Big(\rho_{\mathrm{S}}^{\mathrm{w}}(\mathbf{x},\mathbf{p},t)\Big),\end{aligned} \tag{2.50}$$

where we introduced the shorthand notation $\mathcal{L}_{\mathrm{S}}^{\mathrm{w}}(\mathbf{x})$ for the reduced BMME of the Wigner-transformed Hamiltonian $H_{\mathrm{S}}^{\mathrm{w}}$ for fixed vibrational coordinates $\mathbf{x}$. By virtue of Eq. (2.49), $\mathcal{L}_{\mathrm{S}}^{\mathrm{w}}$ is independent of the momenta $\mathbf{p}$ because $H_{\mathrm{S}}^{\mathrm{w}}$ only contributes in the form of a commutator. In the spirit of [39], we call the above Eq. (2.50) the *quantum-classical* Born-Markov master equation. The classical part of the equation is given by an anti-symmetrized Poisson bracket,

$$\{A,B\}_a = \frac{1}{2}\sum_{\alpha}\left(\frac{\partial A}{\partial x_\alpha}\frac{\partial B}{\partial p_\alpha} + \frac{\partial B}{\partial p_\alpha}\frac{\partial A}{\partial x_\alpha} - \frac{\partial A}{\partial p_\alpha}\frac{\partial B}{\partial x_\alpha} - \frac{\partial B}{\partial x_\alpha}\frac{\partial A}{\partial p_\alpha}\right).$$

In the next step, we derive the corresponding equation of motion for the classical coordinates $(\mathbf{x}, \mathbf{p})$. We start by evaluating the Poisson bracket in the above Eq. (2.50),

$$\begin{aligned}\{H_{\mathrm{S}}^{\mathrm{w}}, \rho_{\mathrm{S}}^{\mathrm{w}}\}_a &= \frac{1}{2}\sum_\alpha \left(\frac{\partial H_{\mathrm{S}}^{\mathrm{w}}}{\partial x_\alpha}\frac{\partial \rho_{\mathrm{S}}^{\mathrm{w}}}{\partial p_\alpha} + \frac{\partial \rho_{\mathrm{S}}^{\mathrm{w}}}{\partial p_\alpha}\frac{\partial H_{\mathrm{S}}^{\mathrm{w}}}{\partial x_\alpha} - \frac{\partial H_{\mathrm{S}}^{\mathrm{w}}}{\partial p_\alpha}\frac{\partial \rho_{\mathrm{S}}^{\mathrm{w}}}{\partial x_\alpha} - \frac{\partial \rho_{\mathrm{S}}^{\mathrm{w}}}{\partial x_\alpha}\frac{\partial H_{\mathrm{S}}^{\mathrm{w}}}{\partial p_\alpha} \right) \\ &= \frac{1}{2}\sum_\alpha \left(\frac{\partial H_{\mathrm{S}}^{\mathrm{w}}}{\partial x_\alpha}\frac{\partial \rho_{\mathrm{S}}^{\mathrm{w}}}{\partial p_\alpha} + \frac{\partial \rho_{\mathrm{S}}^{\mathrm{w}}}{\partial p_\alpha}\frac{\partial H_{\mathrm{S}}^{\mathrm{w}}}{\partial x_\alpha} \right) - \sum_\alpha \frac{p_\alpha}{m_\alpha}\frac{\partial \rho_{\mathrm{S}}^{\mathrm{w}}}{\partial x_\alpha}.\end{aligned}$$

Now, consider the vibrational coordinates to be fixed and, correspondingly, the momenta to be zero, $\mathbf{p} = 0$. In this case, the Poisson bracket will vanish, and the differential equation left for the Wigner-transformed density matrix $\rho_{\mathrm{S}}^{\mathrm{w}}$ is an ordinary BMME, though without the vibrational degrees of freedom,

$$\frac{\partial}{\partial t}\rho_{\mathrm{S}}^{\mathrm{w}}(\mathbf{x}, \mathbf{p}=0, t) = \mathcal{L}_{\mathrm{S}}^{\mathrm{w}}(\mathbf{x})\Big(\rho_{\mathrm{S}}^{\mathrm{w}}(\mathbf{x}, \mathbf{p}=0, t)\Big),$$

yielding a local steady state, $\rho_{\mathrm{S}}^{\mathrm{w,\,ss}}(\mathbf{x})$, for which

$$\mathcal{L}_{\mathrm{S}}^{\mathrm{w}}(\mathbf{x})\Big(\rho_{\mathrm{S}}^{\mathrm{w,\,ss}}(\mathbf{x})\Big) = 0. \tag{2.51}$$

If the vibrational motion is now taken into account, the transformed density matrix $\rho_{\mathrm{S}}^{\mathrm{w}}$ will differ from the local steady state. We define

$$\begin{aligned} & A(\mathbf{x}, \mathbf{p}, t) := \mathrm{tr}_{\mathrm{S}}^{\mathrm{w}}\left\{\rho_{\mathrm{S}}^{\mathrm{w}}(\mathbf{x}, \mathbf{p}, t)\right\}, \\ & B(\mathbf{x}, \mathbf{p}, t) := \rho_{\mathrm{S}}^{\mathrm{w}}(\mathbf{x}, \mathbf{p}, t) - A(\mathbf{x}, \mathbf{p}, t)\rho_{\mathrm{S}}^{\mathrm{w,\,ss}}(\mathbf{x}) \\ \Rightarrow \quad & \rho_{\mathrm{S}}^{\mathrm{w}}(\mathbf{x}, \mathbf{p}, t) = A(\mathbf{x}, \mathbf{p}, t)\rho_{\mathrm{S}}^{\mathrm{w,\,ss}}(\mathbf{x}) + B(\mathbf{x}, \mathbf{p}, t), \quad \text{with } \mathrm{tr}_{\mathrm{S}}^{\mathrm{w}}\left\{B(\mathbf{x}, \mathbf{p}, t)\right\} = 0. \end{aligned}$$

The quantity $A(\mathbf{x}, \mathbf{p}, t)$ is the phase space probability density of the vibrational degrees of freedom, and $B(\mathbf{x}, \mathbf{p}, t)$ is the difference between its momentary value and the phase space probability density of the corresponding steady state, $\rho_{\mathrm{S}}^{\mathrm{w,\,ss}}(\mathbf{x})$. Using Eq. (2.50), we can write the equations of motion for A and B,

$$\frac{\partial}{\partial t}A = -\sum_\alpha \frac{p_\alpha}{m_\alpha}\frac{\partial A}{\partial x_\alpha} + \sum_\alpha \mathrm{tr}_{\mathrm{S}}^{\mathrm{w}}\left\{\frac{\partial H_{\mathrm{S}}^{\mathrm{w}}}{\partial x_\alpha}\rho_{\mathrm{S}}^{\mathrm{w,\,ss}}\right\}\frac{\partial A}{\partial p_\alpha} + \sum_\alpha \mathrm{tr}_{\mathrm{S}}^{\mathrm{w}}\left\{\frac{\partial H_{\mathrm{S}}^{\mathrm{w}}}{\partial x_\alpha}\frac{\partial B}{\partial p_\alpha}\right\}, \tag{2.52}$$

$$\begin{aligned}\frac{\partial}{\partial t}B = & \left\{H_{\mathrm{S}}^{\mathrm{w}}, B\right\}_a - \rho_{\mathrm{S}}^{\mathrm{w,\,ss}}\,\mathrm{tr}_{\mathrm{S}}^{\mathrm{w}}\left\{H_{\mathrm{S}}^{\mathrm{w}}, B\right\}_a \\ & + \left\{H_{\mathrm{S}}^{\mathrm{w}}, A\rho_{\mathrm{S}}^{\mathrm{w,\,ss}}\right\}_a - \rho_{\mathrm{S}}^{\mathrm{w,\,ss}}\,\mathrm{tr}_{\mathrm{S}}^{\mathrm{w}}\left\{H_{\mathrm{S}}^{\mathrm{w}}, A\rho_{\mathrm{S}}^{\mathrm{w,\,ss}}\right\}_a + \mathcal{L}_{\mathrm{S}}^{\mathrm{w}}(B).\end{aligned} \tag{2.53}$$

So far, we have only made the semi-classical approximation for the vibrational dynamics. Now, we also consider the assumed time-scale separation to the much faster electron dynamics. Therefore, $\rho_{\mathrm{S}}^{\mathrm{w}}(\mathbf{x}, \mathbf{p}, t)$ will always be close to the local steady state, $\rho_{\mathrm{S}}^{\mathrm{w,\,ss}}(\mathbf{x})$, and B is expected to be small. Hence, we approximate the equation of motion for B to lowest order, that is, we keep only zero-order terms in B [36], resulting in

$$0 = \left\{H_{\mathrm{S}}^{\mathrm{w}}, A\rho_{\mathrm{S}}^{\mathrm{w,\,ss}}\right\}_a - \rho_{\mathrm{S}}^{\mathrm{w,\,ss}}\,\mathrm{tr}_{\mathrm{S}}^{\mathrm{w}}\left\{H_{\mathrm{S}}^{\mathrm{w}}, A\rho_{\mathrm{S}}^{\mathrm{w,\,ss}}\right\}_a + \mathcal{L}_{\mathrm{S}}^{\mathrm{w}}(B).$$

By formally inverting $\mathcal{L}_{\mathrm{S}}^{\mathrm{w}}(B)$ in the above, and inserting the solution for B into Eq. (2.52), we arrive at a closed Fokker-Planck equation for A,

$$\frac{\partial}{\partial t}A = -\sum_\alpha \frac{p_\alpha}{m_\alpha}\frac{\partial A}{\partial x_\alpha} - \sum_\alpha F_\alpha \frac{\partial A}{\partial p_\alpha} + \sum_{\alpha\beta}\gamma_{\alpha\beta}\frac{\partial}{\partial p_\alpha}\left(\frac{p_\beta}{m_\beta}A\right) + \sum_{\alpha\beta} D_{\alpha\beta}\frac{\partial^2 A}{\partial p_\alpha \partial p_\beta}, \tag{2.54}$$

where the mean force F_α, the friction tensor $\gamma_{\alpha\beta}$, and the diffusion tensor $D_{\alpha\beta}$ are given as

$$F_\alpha = -\operatorname{tr}_{\mathrm{S}}^{\mathrm{w}}\left\{\frac{\partial H_{\mathrm{S}}^{\mathrm{w}}}{\partial x_\alpha}\rho_{\mathrm{S}}^{\mathrm{w,ss}}\right\}, \tag{2.55}$$

$$\gamma_{\alpha\beta} = \operatorname{tr}_{\mathrm{S}}^{\mathrm{w}}\left\{\frac{\partial H_{\mathrm{S}}^{\mathrm{w}}}{\partial x_\alpha}(\mathcal{L}_{\mathrm{S}}^{\mathrm{w}})^{-1}\left(\frac{\partial \rho_{\mathrm{S}}^{\mathrm{w,ss}}}{\partial x_\beta}\right)\right\}, \tag{2.56}$$

$$D_{\alpha\beta} = -\frac{1}{2}\operatorname{tr}_{\mathrm{S}}^{\mathrm{w}}\left\{\frac{\partial H_{\mathrm{S}}^{\mathrm{w}}}{\partial x_\alpha}(\mathcal{L}_{\mathrm{S}}^{\mathrm{w}})^{-1}\left(\frac{\partial H_{\mathrm{S}}^{\mathrm{w}}}{\partial x_\beta}\rho_{\mathrm{S}}^{\mathrm{w,ss}} + \rho_{\mathrm{S}}^{\mathrm{w,ss}}\frac{\partial H_{\mathrm{S}}^{\mathrm{w}}}{\partial x_\beta} + 2\rho_{\mathrm{S}}^{\mathrm{w,ss}}F_\beta\right)\right\}. \tag{2.57}$$

Eq. (2.54) is a special type of Fokker-Planck equation, usually referred to as a *Fokker-Planck equation in phase space* [50, 51], as it contains both positions and momenta. The Langevin equation that corresponds to the Fokker-Planck equation (2.54) is

$$m_\alpha \ddot{x}_\alpha = F_\alpha - \sum_\beta \gamma_{\alpha\beta}\dot{x}_\beta + \eta_\alpha(t), \tag{2.58}$$

where $\eta_\alpha(t)$ is a stochastic white-noise force, which obeys

$$\langle \eta_\alpha(t)\rangle = 0,$$
$$\left\langle \eta_\alpha(t)\eta_\beta(t')\right\rangle = 2D_{\alpha\beta}\delta(t-t').$$

The above quantities F_α, $\gamma_{\alpha\beta}$, and $D_{\alpha\beta}$ are the central quantities of this semi-classical theory. The mean force, F_α, can be understood as a semi-classical adiabatic approximation of the force on the vibrational degrees of freedom. The stochastic force, specified by the diffusion tensor $D_{\alpha\beta}$, and the electronic friction, $\gamma_{\alpha\beta}$, which also gave this theory its name, are the first-order correction to the adiabatic approximation. In this sense, the theory of electronic friction is the first-order correction to the adiabatic Born-Oppenheimer approximation. As F_α, $\gamma_{\alpha\beta}$, and $D_{\alpha\beta}$ contain various derivatives of $H_{\mathrm{S}}^{\mathrm{w}}$ and $\rho_{\mathrm{S}}^{\mathrm{w,ss}}$ with respect to the vibrational positions x_α, they are themselves position-dependent. The mean force, friction, and diffusion are the means of influence of the electrons on the vibrational modes in this semi-classical picture. Therefore, they are called the *current-induced forces*.

2.4.3 Inverting the master equation

The expressions for the friction tensor, $\gamma_{\alpha\beta}$, and the diffusion tensor, $D_{\alpha\beta}$, given in Eqs. (2.56) and (2.57) raise a question concerning their practical evaluation, as they rely on the existence of an inverse of the BMME, $(\mathcal{L}_{\mathrm{S}}^{\mathrm{w}})^{-1}$. To find this inverse, we make use of our results from Sec. 2.2.2, where we considered the BMME in the Liouville space, leading to the form

$$\frac{\mathrm{d}}{\mathrm{d}t}\left|\rho_{\mathrm{S}}\right\rangle = L\left|\rho_{\mathrm{S}}\right\rangle,$$

with L given by Eq. (2.36). Given that all the systems we consider have a unique steady state, $|\rho_{\mathrm{S}}^{\mathrm{ss}}\rangle$, with $L|\rho_{\mathrm{S}}^{\mathrm{ss}}\rangle = 0$, there exists no ordinary inverse of L. However, we can construct a suitable pseudo-inverse, L^{g}. For this, we determine the eigenvalues and eigenstates of the Liouvillian, $L|\ell_n\rangle = \ell_n|\ell_n\rangle$. In doing so, we expect to find one eigenvalue $\ell_{n_0} = 0$, which corresponds to the steady state, $|\ell_{n_0}\rangle = |\rho_{\mathrm{S}}^{\mathrm{ss}}\rangle$. Assuming that

this is the unique steady state to which all initial states eventually evolve, we expect $\mathrm{Re}(\ell_n) < 0$ for all other eigenvalues. With this, we construct the pseudo-inverse as

$$L^{\mathrm{g}} := \sum_{n \neq n_0} \frac{1}{\ell_n} |\ell_n\rangle\langle\ell_n| \,. \tag{2.59}$$

It can be verified easily that this acts as an inverse of L for all vectors with $\langle \ell_{n_0} | r \rangle = 0$,

$$\begin{aligned} L^{\mathrm{g}} L &= \Big(\sum_{n \neq n_0} \frac{1}{w_n} |n\rangle\langle n| \Big) \Big(\sum_m w_m |m\rangle\langle m| \Big) \\ &= \sum_{n \neq n_0} \sum_m \frac{\ell_m}{\ell_n} |\ell_n\rangle \underbrace{\langle \ell_n | \ell_m \rangle}_{=\delta_{nm}} \langle \ell_m| \\ &= \sum_{n \neq n_0} |\ell_n\rangle\langle\ell_n| = \mathbb{1} - |\ell_{n_0}\rangle\langle\ell_{n_0}| \,. \end{aligned}$$

With this, it now remains to show that the expressions from Eqs. (2.56) and (2.57), for which we seek the inverse, are indeed orthogonal to the kernel of L or $\mathcal{L}_{\mathrm{S}}^{\mathrm{w}}$, respectively. For this, we consider the trace of said expressions, starting with the one from Eq. (2.56). Since $\mathrm{tr}_{\mathrm{S}}^{\mathrm{w}}\{\rho_{\mathrm{S}}^{\mathrm{w,\,ss}}(\mathbf{x})\} = 1$ is a fundamental requirement, any derivative of $\rho_{\mathrm{S}}^{\mathrm{w,\,ss}}$ must be traceless to preserve this property. In particular, this requires

$$\mathrm{tr}_{\mathrm{S}}^{\mathrm{w}} \left\{ \frac{\partial \rho_{\mathrm{S}}^{\mathrm{w,\,ss}}}{\partial x_\beta} \right\} = 0.$$

Furthermore, for the expression from Eq. (2.57), we find

$$\begin{aligned} &\mathrm{tr}_{\mathrm{S}}^{\mathrm{w}} \left\{ \frac{\partial H_{\mathrm{S}}^{\mathrm{w}}}{\partial x_\beta} \rho_{\mathrm{S}}^{\mathrm{w,\,ss}} + \rho_{\mathrm{S}}^{\mathrm{w,\,ss}} \frac{\partial H_{\mathrm{S}}^{\mathrm{w}}}{\partial x_\beta} + 2 \rho_{\mathrm{S}}^{\mathrm{w,\,ss}} F_\beta \right\} \\ = \underbrace{\mathrm{tr}_{\mathrm{S}}^{\mathrm{w}} \left\{ \frac{\partial H_{\mathrm{S}}^{\mathrm{w}}}{\partial x_\beta} \rho_{\mathrm{S}}^{\mathrm{w,\,ss}} \right\}}_{=-F_\beta} &+ \underbrace{\mathrm{tr}_{\mathrm{S}}^{\mathrm{w}} \left\{ \rho_{\mathrm{S}}^{\mathrm{w,\,ss}} \frac{\partial H_{\mathrm{S}}^{\mathrm{w}}}{\partial x_\beta} \right\}}_{=-F_\beta} + 2 \underbrace{\mathrm{tr}_{\mathrm{S}}^{\mathrm{w}} \left\{ \rho_{\mathrm{S}}^{\mathrm{w,\,ss}} \right\}}_{=1} F_\beta = 0. \end{aligned}$$

That is, both expressions upon which we apply the pseudo-inverse are traceless. But since $\mathrm{tr}_{\mathrm{S}}^{\mathrm{w}}\{\rho_{\mathrm{S}}^{\mathrm{w,\,ss}}\} = 1$, the two expressions can consequently have no component proportional to $\rho_{\mathrm{S}}^{\mathrm{w,\,ss}}$. In terms of the Liouville space, the two expressions are, in fact, orthogonal to $|\rho_{\mathrm{S}}^{\mathrm{w,\,ss}}\rangle$ and hence to the kernel of L. Thus, the inverses sought are well-defined via the pseudo-inverse, L^{g}, defined in Eq. (2.59).

2.4.4 Calculation of semi-classical steady state

As mentioned in Sec. 2.2.2, we do not study the transient dynamics of the molecular junction. Therefore, the time evolution of the phase space density, $A(\mathbf{x},\mathbf{p},t) = \mathrm{tr}_{\mathrm{S}}^{\mathrm{w}}\{\rho_{\mathrm{S}}^{\mathrm{w}}(\mathbf{x},\mathbf{p},t)\}$, is not needed. Instead, we are only interested in expectation values of the associated steady state, $A^{\mathrm{ss}}(\mathbf{x},\mathbf{p})$, which is defined by

$$\frac{\partial}{\partial t}A^{\mathrm{ss}}(\mathbf{x},\mathbf{p}) = 0.$$

The existence and uniqueness of a steady state of the type of Fokker-Planck equation in Eq. (2.54) is known only under certain conditions. For example, when the friction, $\gamma_{\alpha\beta}$, and the diffusion, $D_{\alpha\beta}$, are constant, and the mean force, F_α, is linear, a unique steady state exists and can even be derived analytically [50, 51]. In this special case, Eq. (2.54) is also called *Klein-Kramers equation*. For general position-dependent mean force, friction, and diffusion, as given in Eqs. (2.55) to (2.57), however, it is not known, as far as we are aware, whether a steady state exists and if it is unique. As we will see later, though, we are dealing with mean forces in the following, which are approximately linear for most coordinates. Therefore, we assume the existence of a unique steady state for the following consideration.

Directly solving the Fokker-Planck equation (2.54) for the assumed unique steady state by setting $\frac{\partial}{\partial t}A^{\mathrm{ss}} = 0$ is very costly because the current-induced forces are position-dependent. Instead, the development of a different procedure is more promising. For this, we first require a way of propagating the Langevin equations of motion (2.58). In the following studies, we will only consider nanosystems with a single semi-classical vibrational mode. In this case, the equations of motion can be conveniently reformulated in dimensionless variables, defined as

$$X := x\sqrt{\frac{m\omega}{\hbar}}, \qquad P := \frac{p}{\sqrt{\hbar m\omega}}. \tag{2.60}$$

In these dimensionless coordinates, the equations of motion take the form

$$\begin{aligned}\frac{\mathrm{d}}{\mathrm{d}(\omega t)}X(\omega t) &= P(\omega t),\\ \frac{\mathrm{d}}{\mathrm{d}(\omega t)}P(\omega t) &= \frac{F(X)}{\sqrt{\hbar\omega\cdot m\omega^2}} - \frac{\gamma(X)}{m\omega}\cdot P(\omega t) + \frac{\eta(\omega t)}{\sqrt{\hbar m\omega}},\end{aligned} \tag{2.61}$$

where the stochastic force, $\eta(\omega t)$, fulfills the relations

$$\begin{aligned}\langle\eta(\omega t)\rangle &= 0,\\ \left\langle \frac{\eta(\omega t)}{\sqrt{\hbar m\omega}}\frac{\eta(\omega t')}{\sqrt{\hbar m\omega}}\right\rangle &= \frac{1}{\hbar m\omega}\left\langle\eta(\omega t)\eta(\omega t')\right\rangle = \frac{1}{\hbar m\omega}2D(X)\delta(t-t')\\ &= 2\frac{D(X)}{\hbar m\omega^2}\delta(\omega t-\omega t').\end{aligned}$$

To integrate this set of stochastic differential equations, we implement the *multiple time stepping BAOAB* algorithm (m-BAOAB) described in [52]. For the systems considered in this work, a base time step of $\Delta(\omega t) = 10^{-2}$ and a step multiplicity of $K = 10$ have proven to deliver a converged time propagation throughout. As this means that we have to perform on the order of 10^3 integration steps to cover a time interval of only

$\sim 1/\omega$, it is not feasible to individually calculate the current-induced forces, $F(X)$, $\gamma(X)$, and $D(X)$, for each value $X(\omega t)$ that is taken during the propagation. Instead, we pre-calculate F, γ, and D for a fixed grid of X values with an equidistant spacing, ΔX, and use linear interpolation between the two closest grid points to approximate their true values at any $X(\omega t)$. This significantly reduces the numerical effort while still delivering adequate precision, as long as the chosen grid spacing, ΔX, appropriately captures the features of F, γ, and D.

Assuming the steady state of the Fokker-Planck equation (2.54) for given current-induced forces is unique, any trajectory, $(X(\omega t), P(\omega t))$, that is propagated according to the Langevin equation (2.61), will eventually reach that unique steady state after some time ωt^{ss}, in the sense that its momentary coordinate values, $(X(\omega t), P(\omega t))$, for $\omega t \geq \omega t^{\mathrm{ss}}$, will be a statistical sample of the steady-state phase space density, $A^{\mathrm{ss}}(X, P)$. While this does not give us a way to determine the functional form of $A^{\mathrm{ss}}(X, P)$, we can nevertheless approximate expectation values of $A^{\mathrm{ss}}(X, P)$ from a sufficiently large number of such statistical samples by calculating the respective sample average according to

$$\langle f \rangle = \frac{1}{N_{\mathrm{sample}}} \sum_{i=1}^{N_{\mathrm{sample}}} f_{(X,P)_i}, \tag{2.62}$$

$$\tag{2.63}$$

where f is some observable determined by X and P. The statistical uncertainty arising from this process is given by the sample standard deviation,

$$\sigma_{\langle f \rangle} = \frac{1}{N_{\mathrm{sample}}} \sqrt{\sum_{i=1}^{N_{\mathrm{sample}}} \Big(f_{(X,P)_i} - \langle f \rangle \Big)^2}.$$

To reduce this statistical uncertainty, a large sample size is required, typically in the order of several thousand. On the one hand, this can be accomplished by propagating multiple trajectories in parallel. On the other hand, one can also take multiple samples from a single trajectory at multiple time points $\omega t_1, \omega t_2, ... > \omega t^{\mathrm{ss}}$. These individual time points must be sufficiently far apart from each other to ensure statistical independence of the samples. Ultimately, a balanced approach using both of these procedures is implemented.

For the following studies, it has been found to be numerically favorable to propagate 500 individual trajectories in parallel to the steady state. Then, from each trajectory, 100 statistically independent samples are drawn, each $100\,\omega t$ apart from one another to ensure independence. This gives a total of 50 000 coordinate samples, $(X, P)_i$, which allow the computation of sample averages with reasonably small uncertainty.

This procedure can also be generalized for two or more semi-classical vibrations. The introduced representation in dimensionless coordinates is only possible for identical natural frequencies, though. However, in the following, we will only ever consider a single semi-classical vibrational mode.

2.4.5 Observables of interest

In our following semi-classical studies, we differentiate two types of observables. First, there are the momentary observables. These are position-dependent observables for a single realization of the semi-classical system under consideration. For a given Langevin trajectory, $(X(\omega t), P(\omega t))$, they are determined by the momentary position, $X(\omega t)$, at a given time ωt. The momentary observables include, first of all, the current-induced forces, namely the mean force, F, the friction, γ, and the diffusion, D, as given by Eqs. (2.55) to (2.57). To better understand the effects and the physical origin of the mean force, we also determine the potential of the mean force, in the following, always referred to as PMF for short. The PMF is defined as

$$\mathrm{PMF}(X) = \mathrm{PMF}\left(x\sqrt{m\omega/\hbar}\right) := -\int_{x_0}^{x} \mathrm{d}x\, F(x), \tag{2.64}$$

where x_0 is chosen such that $\min_X\{\mathrm{PMF}(X)\} = 0$. In addition, we also consider the instantaneous electric current, $\langle I\rangle(X)$, defined as

$$\langle I\rangle(X) := \langle I\rangle(\rho_{\mathrm{S}}^{\mathrm{w,\,ss}}(X)), \tag{2.65}$$

and in Chapter 4, we also require the instantaneous excitation, $\langle N_{\mathrm{hf}}\rangle(X)$, of an additional high-frequency vibration, which is treated quantum-mechanically alongside the electronic dynamics because of its high frequency. The latter is defined as

$$\langle N_{\mathrm{hf}}\rangle(X) := \langle N_{\mathrm{hf}}\rangle(\rho_{\mathrm{S}}^{\mathrm{w,\,ss}}(X)). \tag{2.66}$$

These two instantaneous quantities, $\langle I\rangle(X)$ and $\langle N_{\mathrm{hf}}\rangle(X)$, are expectation values of observables of the remaining quantum part of the system, which depend on the semi-classical coordinate X due to the position-dependence of the transformed Hamiltonian and density matrix, $H_{\mathrm{S}}^{\mathrm{w}}(X)$ and $\rho_{\mathrm{S}}^{\mathrm{w,\,ss}}(X)$. By themselves, $\langle I\rangle(X)$ and $\langle N_{\mathrm{hf}}\rangle(X)$ are of little interest, but are needed for further calculations, as we shall see in the next paragraph.

The second type of observables is expectation values of the semi-classical steady state. These will be calculated using the procedure described in Sec. 2.4.4. The steady-state expectation values of interest include the mean values of displacement and momentum of the semi-classical vibration, $\langle X\rangle^{\mathrm{ss}}$ and $\langle P\rangle^{\mathrm{ss}}$, and the mean values of their squares, $\langle X^2\rangle^{\mathrm{ss}}$ and $\langle P^2\rangle^{\mathrm{ss}}$, which can be calculated directly from the coordinate samples, $(X, P)_i$, following Eq. (2.62). From $\langle X^2\rangle^{\mathrm{ss}}$ and $\langle P^2\rangle^{\mathrm{ss}}$, we can further determine the average vibrational excitation of the semi-classical mode,

$$\langle N\rangle^{\mathrm{ss}} = \langle a^\dagger a\rangle^{\mathrm{ss}} = \frac{\langle X^2\rangle^{\mathrm{ss}} + \langle P^2\rangle^{\mathrm{ss}} - 1}{2}. \tag{2.67}$$

Another crucial quantity is the steady-state electric current, $\langle I\rangle^{\mathrm{ss}}$, for the calculation of which the above instantaneous quantity, $\langle I\rangle(X)$, is needed,

$$\langle I\rangle^{\mathrm{ss}} = \frac{1}{N_{\mathrm{sample}}} \sum_{i=1}^{N_{\mathrm{sample}}} \langle I\rangle(X_i). \tag{2.68}$$

Lastly, in Chapter 4, we also consider the steady-state excitation of a high-frequency vibrational mode, $\langle N_{\mathrm{hf}}\rangle^{\mathrm{ss}}$, which is also determined from the aforementioned instantaneous quantity,

$$\langle N_{\mathrm{hf}}\rangle^{\mathrm{ss}} = \frac{1}{N_{\mathrm{sample}}} \sum_{i=1}^{N_{\mathrm{sample}}} \langle N_{\mathrm{hf}}\rangle(X_i). \tag{2.69}$$

As mentioned in the previous section, we always use $N_{\text{sample}} = 50\,000$ to determine the steady-state expectation values. In evaluating Eqs. (2.68) and (2.69), it is not feasible to calculate $\langle I \rangle(X)$ and $\langle N_{\text{hf}} \rangle(X)$ for each of the 50 000 coordinate samples individually. Instead, we pre-calculate $\langle I \rangle(X)$ and $\langle N_{\text{hf}} \rangle(X)$ for a fixed grid of X values with an equidistant spacing, and use linear interpolation between the two closest grid points to approximate their true values for any coordinate sample. This procedure is entirely similar to the interpolation of the current-induced forces, mentioned in the previous section.

Chapter 3

Holstein model

In this chapter, we will turn to a well-known example system for a molecular junction: the Holstein model [20, 41, 48]. Our goal is to compare the transport characteristics of the Holstein model, obtained first from a fully quantum-mechanical treatment using the BMME from Sec. 2.2.1, and second obtained by treating the vibrational mode semi-classically via the approach derived in Sec. 2.4. In this way, we want to examine how accurate the semi-classical approach is, and in which parameter regimes it is favorable to use.

In the first section of this chapter, we define the Holstein model and discuss its physical meaning. We then use the BMME to derive its basic quantum-mechanical properties and explain the underlying physical mechanisms in the second section. In the third section, we apply the partial Wigner transform to the quantum Holstein model, and obtain the classical Langevin equation for its vibrational mode. Using this, we calculate the transport characteristics of the Holstein model in the semi-classical picture in the fourth section, and compare them to a fully quantum-mechanical calculation. Lastly, we close this chapter with a summary and conclusion.

3.1 Model

The Holstein model comprises a single electronic level and a vibrational mode with natural frequency ω and mass m. The potential of the vibrational mode is assumed harmonic and depends on the occupation of the electronic level. In the neutral state of the electronic level, the vibrational mode evolves according to the potential energy surface $U_0(\hat{x})$, and in the occupied state, it follows the potential $U_1(\hat{x})$. The system Hamiltonian H_S is

$$H_\mathrm{S} = U_0(\hat{x})dd^\dagger + U_1(\hat{x})d^\dagger d + \frac{\hat{p}^2}{2m},$$

where $\hat{x}$ and $\hat{p}$ are the vibrational displacement and momentum operators. The two potential energy surfaces are

$$U_0(\hat{x}) = \frac{1}{2}m\omega^2\hat{x}^2, \qquad U_1(\hat{x}) = \varepsilon_0 + \Lambda\hat{x} + \frac{1}{2}m\omega^2\hat{x}^2,$$

where ε_0 is the intrinsic energy of the electronic level, and Λ denotes the electronic-vibrational coupling. The explicit notation $\hat{\square}$ for the vibrational operators is used here to distinguish them from classical coordinates.

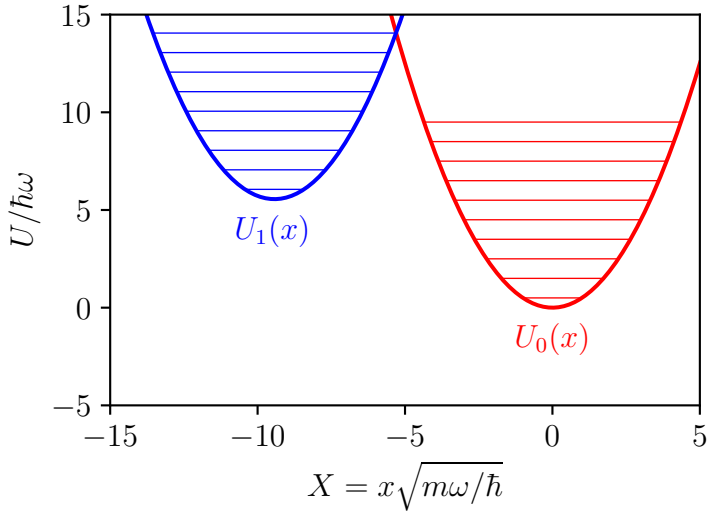

Figure 3.1: Exemplary depiction of two potential energy surfaces for the vibrational mode of a Holstein model. The horizontal lines illustrate the quantized energy levels of the vibrational mode. The parameters are the same as in Fig. 3.6.

Fig. 3.1 shows one example of such two potential energy surfaces. The horizontal lines within the potentials illustrate the quantized energy levels of the vibrational mode. In Fig. 3.1, we used a dimensionless displacement coordinate X. We will use dimensionless displacement and momentum for convenience throughout the following work. These are obtained by defining

$$\hat{X} := \hat{x}\sqrt{\frac{m\omega}{\hbar}}, \qquad \hat{P} := \frac{\hat{p}}{\sqrt{\hbar m\omega}}, \tag{3.1}$$

analogous to Eq. (2.60). In these transformed coordinates, the Hamiltonian and potentials take the form,

$$H_{\mathrm{S}} = U_0(\hat{X})dd^\dagger + U_1(\hat{X})d^\dagger d + \frac{1}{2}\hbar\omega\hat{P}^2, \tag{3.2}$$

$$U_0(\hat{X}) = \frac{1}{2}\hbar\omega\hat{X}^2, \qquad U_1(\hat{X}) = \varepsilon_0 + \sqrt{2}\lambda\hat{X} + \frac{1}{2}\hbar\omega\hat{X}^2, \tag{3.3}$$

where we defined $\lambda := \Lambda\sqrt{\hbar/2m\omega}$. From now on, we will use this λ as the electronic-vibrational coupling.

The electronic level is coupled to both electrodes to enable a current flow through the junction. Coupling between the electrodes and the vibrational mode is neglected. Therefore, the corresponding interaction Hamiltonian, H_{SB}, takes the same form as in Eq. (2.43).

In the next section, we derive the BMME for this model to calculate and discuss its basic quantum-mechanical properties.

3.2 Quantum-mechanical description

3.2.1 Lang-Firsov transformation

To write down the master equation for this system, we first need to diagonalize H_S. This can be accomplished analytically using the Lang-Firsov transformation [48, 53], which is also known as the small polaron transformation. To begin with, we rewrite H_S completely in terms of creation and annihilation operators, $a^\dagger$ and a. Using Eqs. (2.3) and (3.1), we find

$$H_\mathrm{S} = \left(\varepsilon_0 + \lambda(a^\dagger + a)\right) d^\dagger d + \hbar\omega a^\dagger a.$$

For the diagonalization, we define transformed operators as follows,

$$S := \frac{\lambda}{\hbar\omega}\left(a - a^\dagger\right) d^\dagger d, \tag{3.4}$$

$$\tilde{d} := e^S d e^{-S} = d e^{-\lambda(a-a^\dagger)/\hbar\omega}, \qquad \tilde{d}^\dagger := e^S d^\dagger e^{-S} = d^\dagger e^{\lambda(a-a^\dagger)/\hbar\omega}, \tag{3.5}$$

$$\tilde{a} := e^S a e^{-S} = a + \frac{\lambda}{\hbar\omega} d^\dagger d, \qquad \tilde{a}^\dagger := e^S a^\dagger e^{-S} = a^\dagger + \frac{\lambda}{\hbar\omega} d^\dagger d, \tag{3.6}$$

$$\Rightarrow d^\dagger d = \tilde{d}^\dagger \tilde{d}, \qquad \tilde{a}^\dagger\tilde{a} = a^\dagger a + \left(a^\dagger + a\right)\frac{\lambda}{\hbar\omega} d^\dagger d + \left(\frac{\lambda}{\hbar\omega}\right)^2 d^\dagger d.$$

As a result, the system Hamiltonian H_S is diagonal in terms of the transformed operators, $\tilde{d}^{(\dagger)}$ and $\tilde{a}^{(\dagger)}$,

$$H_\mathrm{S} = \left(\varepsilon_0 + \lambda(a^\dagger + a)\right) d^\dagger d + \hbar\omega a^\dagger a = \underbrace{\left(\varepsilon_0 - \frac{\lambda^2}{\hbar\omega}\right)}_{=:\varepsilon_1} \tilde{d}^\dagger\tilde{d} + \hbar\omega\tilde{a}^\dagger\tilde{a},$$

where we defined the renormalized electronic energy $\varepsilon_1 := \varepsilon_0 - \lambda^2/\hbar\omega$.

In the next step, we also need to transform the interaction Hamiltonian. Using $a^\dagger - a = \tilde{a}^\dagger - \tilde{a}$, we find

$$H_\mathrm{SB} = -\underbrace{\tilde{d} e^{\lambda(\tilde{a}-\tilde{a}^\dagger)/\hbar\omega}}_{=d} \cdot \sum_{K\in\{L,R\}} \sum_{k_K} V c_{k_K}^\dagger + \underbrace{\tilde{d}^\dagger e^{-\lambda(\tilde{a}-\tilde{a}^\dagger)/\hbar\omega}}_{=d^\dagger} \cdot \sum_{K\in\{L,R\}} \sum_{k_K} V^* c_{k_K}.$$

Starting from here, we need to find the frequency projected operators, defined in Eq. (2.18), in terms of the transformed operators, $\tilde{d}^{(\dagger)}$ and $\tilde{a}^{(\dagger)}$. Since we have already diagonalized the Hamiltonian, we can read off the possible frequencies directly. Of all possible frequencies, only the frequencies $\frac{\varepsilon_1}{\hbar} + v\cdot\omega$ contribute because the projection of $d^{(\dagger)}$ on any other frequency vanishes. Using the joint Fock basis, $|n, v\rangle := |n\rangle \otimes |v\rangle$, with $\tilde{d}^\dagger\tilde{d}\,|0, v\rangle = 0$, $\tilde{d}^\dagger\tilde{d}\,|1, v\rangle = |1, v\rangle$, and $\tilde{a}^\dagger\tilde{a}\,|n, v\rangle = v\,|n, v\rangle$, we find

$$\begin{aligned}
d(\tfrac{\varepsilon_1}{\hbar} + v\cdot\omega) &= \sum_{v'=\max\{0,-v\}}^{\infty} |0, v'\rangle\langle 0, v'|\, d\, |1, v+v'\rangle\langle 1, v+v'| \\
&= \sum_{v'=\max\{0,-v\}}^{\infty} |0, v'\rangle\langle 0, v'|\, \tilde{d} e^{\lambda(\tilde{a}-\tilde{a}^\dagger)/\hbar\omega}\, |1, v+v'\rangle\langle 1, v+v'| \\
&= \sum_{v'=\max\{0,-v\}}^{\infty} |0, v'\rangle \underbrace{\langle 0|\tilde{d}|1\rangle}_{=1} \underbrace{\langle v'|e^{\lambda(\tilde{a}-\tilde{a}^\dagger)/\hbar\omega}|v+v'\rangle}_{=:\mathrm{FC}^+_{v',v+v'}} \langle 1, v+v'| \\
&= \sum_{v'=\max\{0,-v\}}^{\infty} \mathrm{FC}^+_{v',v+v'}\, |0, v'\rangle\langle 1, v+v'|\,,
\end{aligned}$$

where we defined the so-called *Franck-Condon* matrix, $\mathrm{FC}^{+}_{v,v'}$ [54]. From the expression above, it can be seen that the Franck-Condon matrix elements are essentially a measure of the likelihood that a charge or discharge of the electronic level, mediated by the operators d and $d^\dagger$, is accompanied by a jump of the vibrational excitation from v to v'. The individual Franck-Condon matrix elements can be calculated by dividing the exponential of $(\tilde{a} - \tilde{a}^\dagger)$ into separate exponentials of $\tilde{a}$ and $\tilde{a}^\dagger$, and then inserting the series expansion of the exponential function. The resulting expression is

$$\begin{aligned}\mathrm{FC}^{\pm}_{v,v'} &:= \langle v|e^{\pm\lambda(\tilde{a}-\tilde{a}^\dagger)/\hbar\omega}|v'\rangle = e^{-\frac{1}{2}(\frac{\lambda}{\hbar\omega})^2}\,\langle v|e^{\mp\frac{\lambda}{\hbar\omega}\tilde{a}^\dagger}e^{\pm\frac{\lambda}{\hbar\omega}\tilde{a}}|v'\rangle \\ &= e^{-\frac{1}{2}(\frac{\lambda}{\hbar\omega})^2}\left(\mp\,\mathrm{sgn}(v-v')\frac{\lambda}{\hbar\omega}\right)^{|v-v'|}\sqrt{v!\cdot v'!} \\ &\quad\cdot\sum_{j=0}^{\min\{v,v'\}}\frac{(-1)^j(\frac{\lambda}{\hbar\omega})^{2j}}{(\min\{v,v'\}-j)!\;\;(|v-v'|+j)!\;\,j!}.\end{aligned}$$

We can now, in principle, write down the master equation for the transformed Holstein model. However, as the underlying vibrational basis is technically infinite, there is no way to solve it analytically for the associated steady state, $\rho_{\mathrm{S}}^{\mathrm{ss}}$. Instead, we truncate the vibrational operators, $\tilde{a}^\dagger$ and $\tilde{a}$, at a certain number of vibrational basis states, N_{vib}. The truncated master equation yields only finitely many terms, which we can sum up and solve for an approximate steady state with the procedure from Sec. 2.2.2. It can be safely assumed that the more vibrational basis states we take into account, the closer the approximate solution is to the true solution. To determine whether sufficiently many basis states have been considered, one can either increase N_{vib} until the approximate steady state does not change with further increase, or alternatively check in detail that the highest excited population is close to zero, or to be precise, $\langle N_{\mathrm{vib}}|\rho_{\mathrm{S}}^{\mathrm{ss}}|N_{\mathrm{vib}}\rangle \ll 1/N_{\mathrm{vib}}$.

3.2.2 Properties: Franck-Condon blockade and vibrational instability

Using the procedure from above, we can now determine the steady-state density matrix of the transformed Holstein model, and thus calculate the steady-state electric current through the system by Eq. (2.42). As an example, we consider two different Holstein systems, one with weak electronic-vibrational coupling, $\lambda < \hbar\omega$, and one with strong coupling, $\lambda > \hbar\omega$. We choose the same parameters as in [33] because we also want to compare our results with theirs in the next section. The parameters are

(1) $\varepsilon_0 = 300\,\mathrm{meV}$, $\hbar\omega = 200\,\mathrm{meV}$, $\lambda = 120\,\mathrm{meV}$, $\Gamma^{\mathrm{L}} = \Gamma^{\mathrm{R}} = 10\,\mathrm{meV}$,

(2) $\varepsilon_0 = 1\,050\,\mathrm{meV}$, $\hbar\omega = 200\,\mathrm{meV}$, $\lambda = 400\,\mathrm{meV}$, $\Gamma^{\mathrm{L}} = \Gamma^{\mathrm{R}} = 10\,\mathrm{meV}$.

From the given values ε_0, $\hbar\omega$, and λ, we find that the renormalized energies are $\varepsilon_1 = 228\,\mathrm{meV}$ and $\varepsilon_1 = 250\,\mathrm{meV}$, respectively. Since they are very close to each other and the natural frequencies ω are equal, we find that the frequencies, $\frac{\varepsilon_1}{\hbar} + v\cdot\omega$, of the corresponding transformed Holstein systems are very similar. This allows us to examine in isolation the influence of the different electronic-vibrational couplings, λ.

For these two systems, we calculate the electric current, $\langle I\rangle^{\mathrm{ss}}$, and the average vibrational excitation, $\langle N\rangle^{\mathrm{ss}} = \langle a^\dagger a\rangle^{\mathrm{ss}}$, in the steady state. The results are depicted

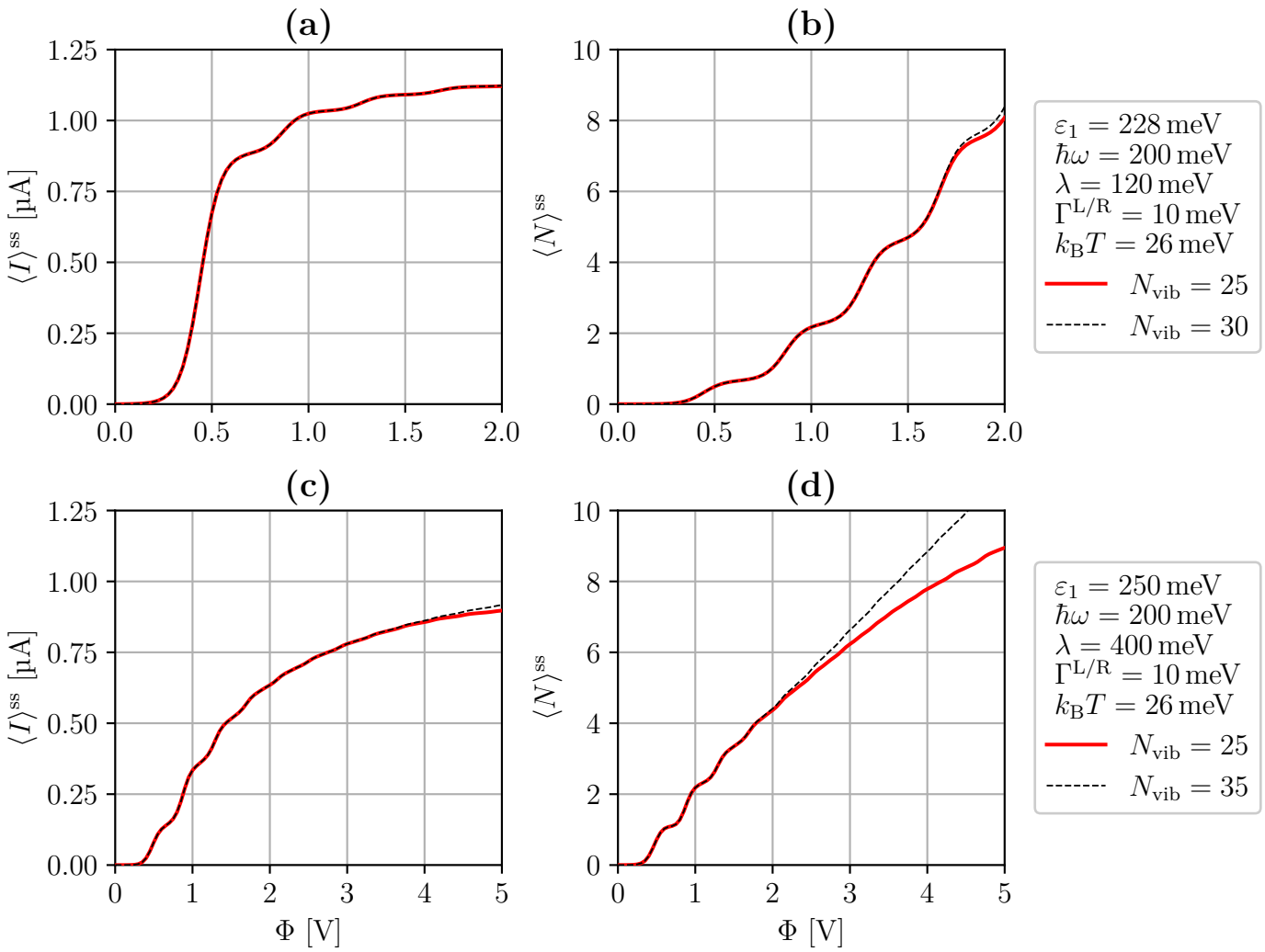

Figure 3.2: Current-voltage characteristics and average vibrational excitation of a Holstein model.

in Fig. 3.2. First, we investigate the convergence. For $\lambda = 120\,\mathrm{meV}$, shown in panels **(a)** and **(b)**, hardly any change is noticeable in the two observables by increasing N_{vib} from 25 to 30. We conclude that the result is well converged for small to medium voltages with $N_{\mathrm{vib}} = 25$ and for high voltages with $N_{\mathrm{vib}} = 30$. For larger coupling, $\lambda = 400\,\mathrm{meV}$, shown in **(c)** and **(d)**, we also see barely any change in the current by increasing N_{vib} from 25 to 35. However, the vibrational excitation significantly differs for bias voltage $\Phi > 2.5\,\mathrm{V}$. We conclude that the electric current is well converged already with $N_{\mathrm{vib}} = 25$, whereas we need an increased $N_{\mathrm{vib}} = 35$ to also converge $\langle N \rangle^{\mathrm{ss}}$ at higher voltages.

Looking at the shape of the curves, it can be seen that with increasing Φ, both current and vibrational excitation continuously increase for both example systems. As in the two examples considered in Sec. 2.3, the increase occurs in a prominent step pattern. For the system with $\lambda = 120\,\mathrm{meV}$, these steps occur at a distance of $\Delta\Phi = 2\hbar\omega/\mathrm{e}$. The first step is at $\Phi = 2\varepsilon_1/\mathrm{e}$. The emergence of these steps can be understood by considering the energy level scheme depicted in Fig. 3.3. In Fig. 3.3**(a)**, we find that at zero bias voltage, the chemical potentials of the electrodes are well below the energy levels of the system; thus, no charge transport is possible. When

the bias voltage is increased to $\Phi > 2\varepsilon_1/\mathrm{e}$, the chemical potential of the left electrode surpasses the energy level ε_1 of the system, as depicted in Fig. 3.3**(b)**. At this point, the first channel of electron transport through the system becomes available, leading to an increase in the current. When the bias voltage is increased further to $\Phi > 2(\varepsilon_1+\hbar\omega)/\mathrm{e}$, shown in Fig. 3.3**(c)**, the chemical potential of the left electrode surpasses the energy $\varepsilon_1 + \hbar\omega$, and a second channel of charge transport becomes available. This channel corresponds to electrons passing through the junction and exciting one quanta of vibration, requiring the additional energy $\hbar\omega$. Subsequently, whenever the voltage is increased above $\Phi > 2(\varepsilon_1 + v \cdot \hbar\omega)/\mathrm{e}$, the chemical potential of the left electrode surpasses another energy threshold, $\varepsilon_1 + v \cdot \hbar\omega$, enabling a further channel of charge transport accompanied by the excitation of v quanta of vibration. This explains the emergence of the many equidistant steps in both current and vibrational excitation. The broadening and finite slope of the steps is due to the broadening of the Fermi functions of the electrodes at finite temperature, $k_\mathrm{B}T > 0$.

Analogous to the excitation of vibrational quanta induced by electron transport, there can also be transport-induced de-excitation. These processes do not contribute to the emergence of the different current steps, however, since they can occur independently of the bias voltage in any transport process, provided that a sufficiently high vibrational excitation is present beforehand.

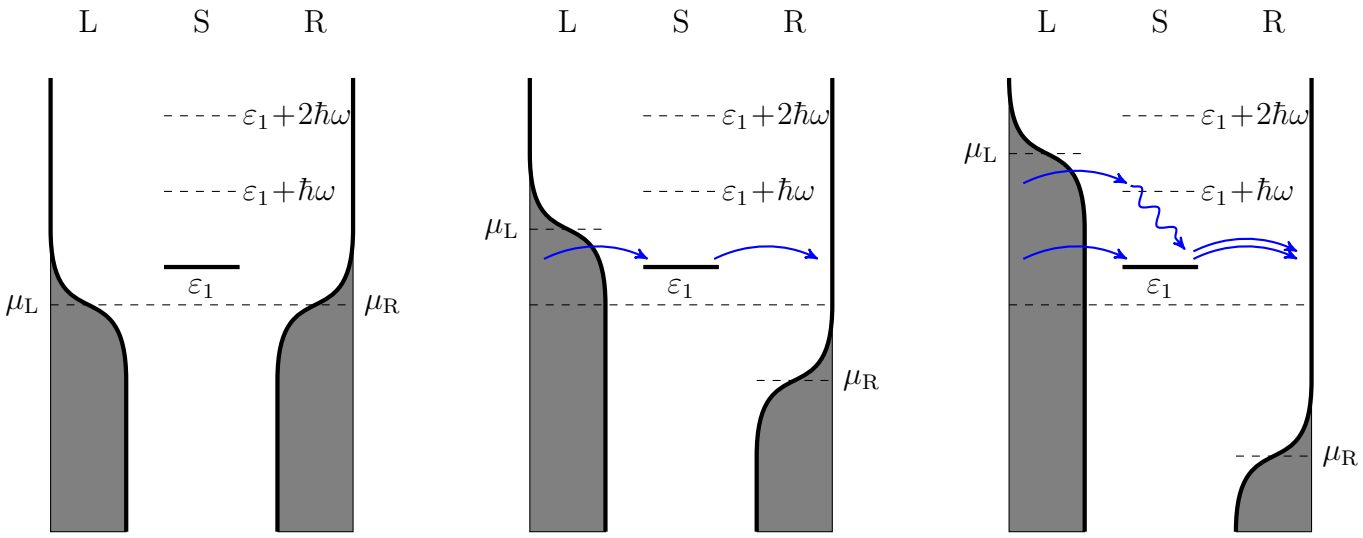

(a) $\Phi = 0$. **(b)** $\Phi > 2\varepsilon_1/\mathrm{e}$. **(c)** $\Phi > 2(\varepsilon_1 + \hbar\omega)/\mathrm{e}$.

Figure 3.3: Energy level scheme for the Holstein model. At zero bias voltage, depicted in **(a)**, the chemical potentials of the electrodes are well below the energy levels of the system; therefore, no charge transport is possible. When the bias voltage is large enough that the chemical potential of the left electrode is above the energy ε_1, as depicted in **(b)**, electron transport becomes possible. When the bias voltage is even larger such that the chemical potential of the left electrode surpasses $\varepsilon_1 + \hbar\omega$, a second transport channel becomes available, as illustrated in **(c)**, where electron transport is accompanied by the excitation of one vibrational quantum.

For the system with larger coupling, $\lambda = 400\,\mathrm{meV}$, the energy thresholds, $\varepsilon_1 + v \cdot \hbar\omega$, are nearly identical as aforementioned, because the values of ε_1 are very close and the

natural frequencies ω are equal. For this reason, we find the current and excitation steps at the same bias voltages also in **(c)** and **(d)** of Fig. 3.2. The magnitude of the steps is different, however. For the system with $\lambda = 120\,\mathrm{meV}$, the step in the current at $\Phi = 2\varepsilon_1/\mathrm{e}$ is the largest, and each subsequent step decreases in size. For the system with $\lambda = 400\,\mathrm{meV}$, on the other hand, the step at $\Phi = 2(\varepsilon_1 + \hbar\omega)/\mathrm{e}$ is the largest. Furthermore, the steps are generally smaller, and the current stays below $1\,\mu\mathrm{A}$ even for bias voltages up to $\Phi = 5\,\mathrm{V}$.

The behavior of $\langle N \rangle^{\mathrm{ss}}$ is also different. For $0 < \Phi < 1\,\mathrm{V}$, the excitation shows hardly any difference for the two considered systems. However, at higher bias voltage, a difference arises. For $\Phi > 1\,\mathrm{V}$, the excitation of the $\lambda = 120\,\mathrm{meV}$ system increases much faster with increasing voltage, reaching an average value of about 8 at $\Phi = 2\,\mathrm{V}$. For $\lambda = 400\,\mathrm{meV}$, on the other hand, the excitation increases to only about 4.5 at $\Phi = 2\,\mathrm{V}$, and stays below 8 until higher voltages around $3.5\,\mathrm{V}$.

The different behavior of the current for small and large electron-vibrational coupling λ can be explained by the *Franck-Condon blockade* [20, 33, 54]. Fig. 3.4 illustrates the Franck-Condon matrices for the two systems considered. It can be seen that, for $\lambda = 120\,\mathrm{meV}$, $\mathrm{FC}^{+}_{0,0}$ is by far the largest matrix element. Consequently, the charge and discharge of the electronic level without additional excitation or de-excitation of the vibrational mode are very likely to occur, which explains why the current step corresponding to this channel, which is the one around $\Phi = 0.45\,\mathrm{V}$, is the largest. In contrast, the largest matrix elements for the $\lambda = 400\,\mathrm{meV}$ system are $\mathrm{FC}^{+}_{0,3}$ and $\mathrm{FC}^{+}_{0,4}$, whereas the $\mathrm{FC}^{+}_{0,0}$ is rather small. As a result, the current step around $\Phi = 0.45\,\mathrm{V}$ is not the largest one because charge and discharge of the electronic level are more favored when accompanied by excitation of multiple quanta of vibration. Overall this leads to a delayed increase in the current as the bias voltage is increased. According to [54], this delay can be quantified to be on the order of $\mathrm{e} \cdot \Delta\Phi \propto \lambda^2/\hbar\omega$. In our case, this would mean that the system with $\lambda = 400\,\mathrm{meV}$ requires an about 11 times larger bias voltage to reach the same current as the system with $\lambda = 120\,\mathrm{meV}$, which fits the results in Fig. 3.2 quite well. For very large bias voltage, though, which is not shown in Fig. 3.2, the currents of both systems saturate to the same limit of $\mathrm{e}\Gamma^{\mathrm{L/R}}/2\hbar = 1.217\,\mu\mathrm{A}$, similar to the resonant level model in Sec. 2.3.1.

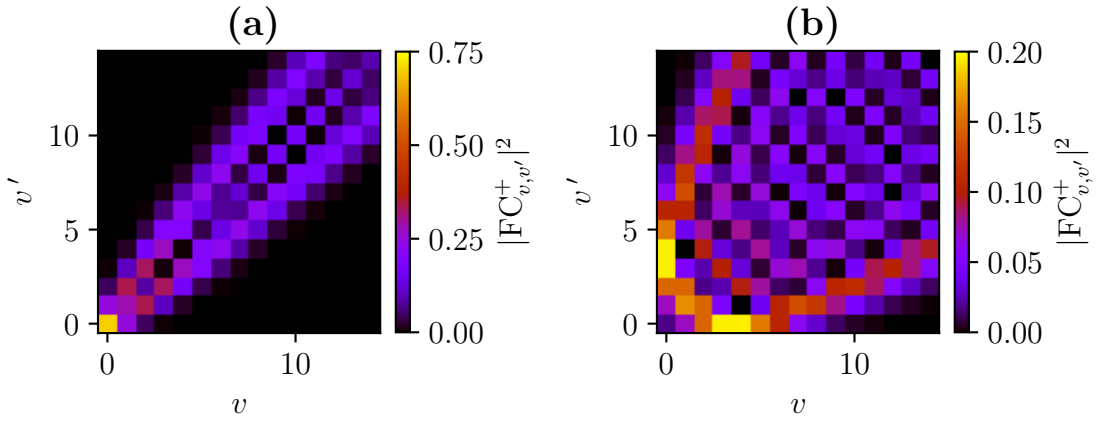

Figure 3.4: Franck-Condon matrix elements for a Holstein model with $\hbar\omega = 200\,\mathrm{meV}$; and $\lambda = 120\,\mathrm{meV}$ in **(a)**; and $\lambda = 400\,\mathrm{meV}$ in **(b)**.

The vibrational excitation cannot be explained by the Franck-Condon blockade and

the transport processes depicted in Fig. 3.3, though. If only current-induced excitation and de-excitation processes were contributing, one would expect the vibrational excitation to saturate as the voltage increases, as does the current. This is, however, not the case because of additional interactions with the electrodes. As is depicted in Fig. 3.5, there can also be vibrationally induced electron-hole pair creation processes [20], which do not contribute to the current but provide a relaxation pathway for the vibrational mode. As the chemical potentials of the electrodes shift further away from the energy level ε_1, when the bias voltage is increased, the creation of electron-hole pairs requires the absorption of increasingly more vibrational quanta, as can be seen by comparing panels **(a)** and **(b)** of Fig. 3.5. This reduces the relaxation effect, thereby leading to an increase in the average vibrational excitation for higher voltages. For weak coupling, $\lambda = 120\,\mathrm{meV}$, the absorption of many vibrational quanta is strongly suppressed by the Franck-Condon matrix, as can be seen in Fig. 3.4. Therefore, the reduction of vibrationally induced electron-hole pair creation is much more pronounced for the weak-coupling system, leading to a much faster increase in the average vibrational excitation in comparison to the strong-coupling case, $\lambda = 400\,\mathrm{meV}$. This counter-intuitive phenomenon is a signature of vibrational instability [20].

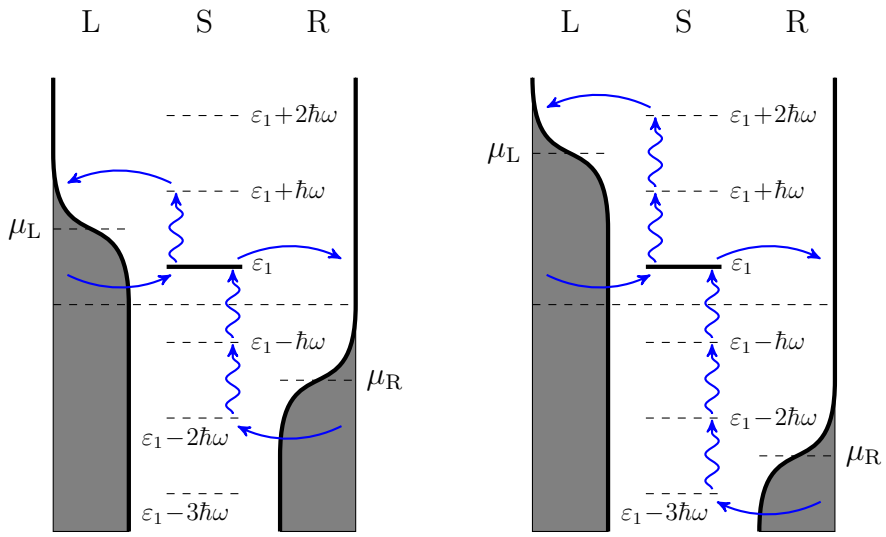

(a) $\Phi > 2\varepsilon_1/\mathrm{e}$. **(b)** $\Phi > 2(\varepsilon_1 + \hbar\omega)/\mathrm{e}$.

Figure 3.5: Energy level scheme for the Holstein model. Apart from charge transport, the Holstein model also exhibits vibrationally induced electron-hole pair creation, as illustrated in **(a)** and **(b)**. In this process, a single or multiple vibrational quanta are de-excited, and the released energy serves to create an electron-hole pair in one of the electrodes. As the bias voltage is increased, electron-hole pair creation requires the de-excitation of increasingly more vibrational quanta, as can be seen by comparing **(a)** and **(b)**.

Both effects discussed only depend on the ratio of the electronic-vibrational coupling to the natural frequency, $\lambda/\hbar\omega$, which is easy to see from the functional form of the Franck-Condon matrix elements. We generally find that the Franck-Condon blockade is stronger the larger $\lambda/\hbar\omega$, leading to a smaller current for strong electronic-vibrational coupling compared to weak coupling at the same voltage. Similarly, the

vibrational excitation is generally larger for weaker electronic-vibrational coupling at a given voltage.

3.2.3 Comparison to exact methods

In this section, we will compare our results with those of [33]. In Fig. 1 of their paper, the authors of [33] have depicted the current-voltage characteristics for the same two Holstein systems discussed in our previous section. Comparing our results from Fig. 3.2 with theirs, we find complete agreement of electric current and vibrational excitation in the voltage ranges they considered.

Apart from using Born-Markov theory, the authors of [33] also calculated the two observables using the numerically exact hierarchical equations of motion (HEOM) approach. They found that for the two systems regarded here, the approximate results from the Born-Markov master equation agree well with the exact HEOM calculation. The Born-Markov calculation slightly underestimates the width of the current and excitation steps. As $\Gamma < k_{\mathrm{B}}T$, their broadening is not significant, though. For larger electrode coupling, $\Gamma > k_{\mathrm{B}}T$, the results of [33] show that the Born-Markov approximation breaks down, however, as we have already anticipated in Sec. 2.2.1.

Concluding our findings from this section, we can trust the BMME for harmonic oscillators linearly coupled to the electronic levels when $\Gamma < k_{\mathrm{B}}T$.

3.3 Semi-classical description and current-induced forces

For the semi-classical treatment of the Holstein model, we take the fully quantum system Hamiltonian, H_S, defined in Eq. (3.2), and apply the partial Wigner transform from Sec. 2.4.2 to find the transformed system Hamiltonian, $H_\mathrm{S}^\mathrm{w}(X,P)$. Following Eq. (2.49), we get

$$H_\mathrm{S}^\mathrm{w}(X,P) = U_0(X)dd^\dagger + U_1(X)d^\dagger d + \frac{1}{2}\hbar\omega P^2,$$

with the potential energy surfaces, $U_0(X)$ and $U_1(X)$, as given in Eq. (3.3). The variables X and P are now the classical coordinates corresponding to the operators $\hat{X}$ and $\hat{P}$. For the time evolution of the classical coordinates, we get the dimensionless Langevin equations from Eq. (2.61). And for the Wigner-transformed density matrix, $\rho_\mathrm{S}^\mathrm{w}(X,P,t)$, we find the quantum-classical BMME in Eq. (2.50).

Before we move on to more comprehensive studies of this semi-classical Holstein system, we first examine the basic physics of the model and compare our results with the literature. To this end, we calculate the current-induced forces and the instantaneous current for a system with the following parameters, $\Gamma^\mathrm{L/R} = 5\,\mathrm{meV}$, $k_\mathrm{B}T = 26\,\mathrm{meV}$, $\hbar\omega = 3\,\mathrm{meV}$, $\lambda = 20\,\mathrm{meV}$, $\varepsilon_0 = 150\,\mathrm{meV}$, and $\Phi = 0\,\mathrm{V}$ [27]. For this, we first need to determine the Wigner-transformed steady state, $\rho_\mathrm{S}^{\mathrm{w,ss}}(X)$, at a fixed vibrational frame, $P = 0$. Following Eq. (2.51), we get $\rho_\mathrm{S}^{\mathrm{w,ss}}(X)$ by solving the BMME of $H_\mathrm{S}^\mathrm{w}(X, P = 0)$, which is just a resonant level model, though with different energy values depending on X. From the resulting $\rho_\mathrm{S}^{\mathrm{w,ss}}(X)$, we calculate the current-induced forces and the instantaneous current, as described in Sec. 2.4.5.

The results are shown in Fig. 3.6. We focus first on the potential of mean force (PMF) in panel **(d)**. We included the potential energy surfaces, $U_0(X)$ and $U_1(X)$, for better understanding. It can be seen that at zero bias voltage, the PMF, which is essentially the adiabatic approximation of the system, follows the course of the potential surface with the lower value for any given X. Around the crossing of the potential surfaces, it switches from one to the other in a shape that reminds of an avoided crossing. From our discussion of the resonant level in Sec. 2.3.1, we know the requirements for charge transport through the junction. For electrons to enter the junction from either of the electrodes, we require $\mu_\mathrm{L/R} > U_1 - U_0$. And for them to leave the junction again, we need $\mu_\mathrm{L/R} < U_1 - U_0$. To achieve a finite current, one of the conditions should be fulfilled for μ_L and the other for μ_R. As illustrated in Fig. 3.7**(a)**, at zero bias voltage, electrons can enter the junction from both electrodes for $X < -\varepsilon_0/\sqrt{2}\lambda \approx -5.3$, because here $U_1 < U_0$, whereas they can leave the junction for $X > -5.3$, where $U_1 > U_0$. But there is no domain where both conditions are satisfied, the resonances, $\mu_\mathrm{L/R} = U_1 - U_0$, are in the same position. Of course, both conditions are not to be understood as sharp limits because of $k_\mathrm{B}T > 0$, as the steps of the Fermi functions of the electrodes are broadened by $k_\mathrm{B}T$. But even if the junction is conductive in a small range around the potential crossing, no net current results, because electrons have no preferred direction through the junction without bias voltage. Thus, for all X, we find $\langle I\rangle(X) = 0$, as it should be. However, if we apply only a small voltage, we immediately find a finite current around the potential crossing point at $X \approx -5.3$.

Next, we take a look at the other quantities as well. We see from Fig. 3.6 that,

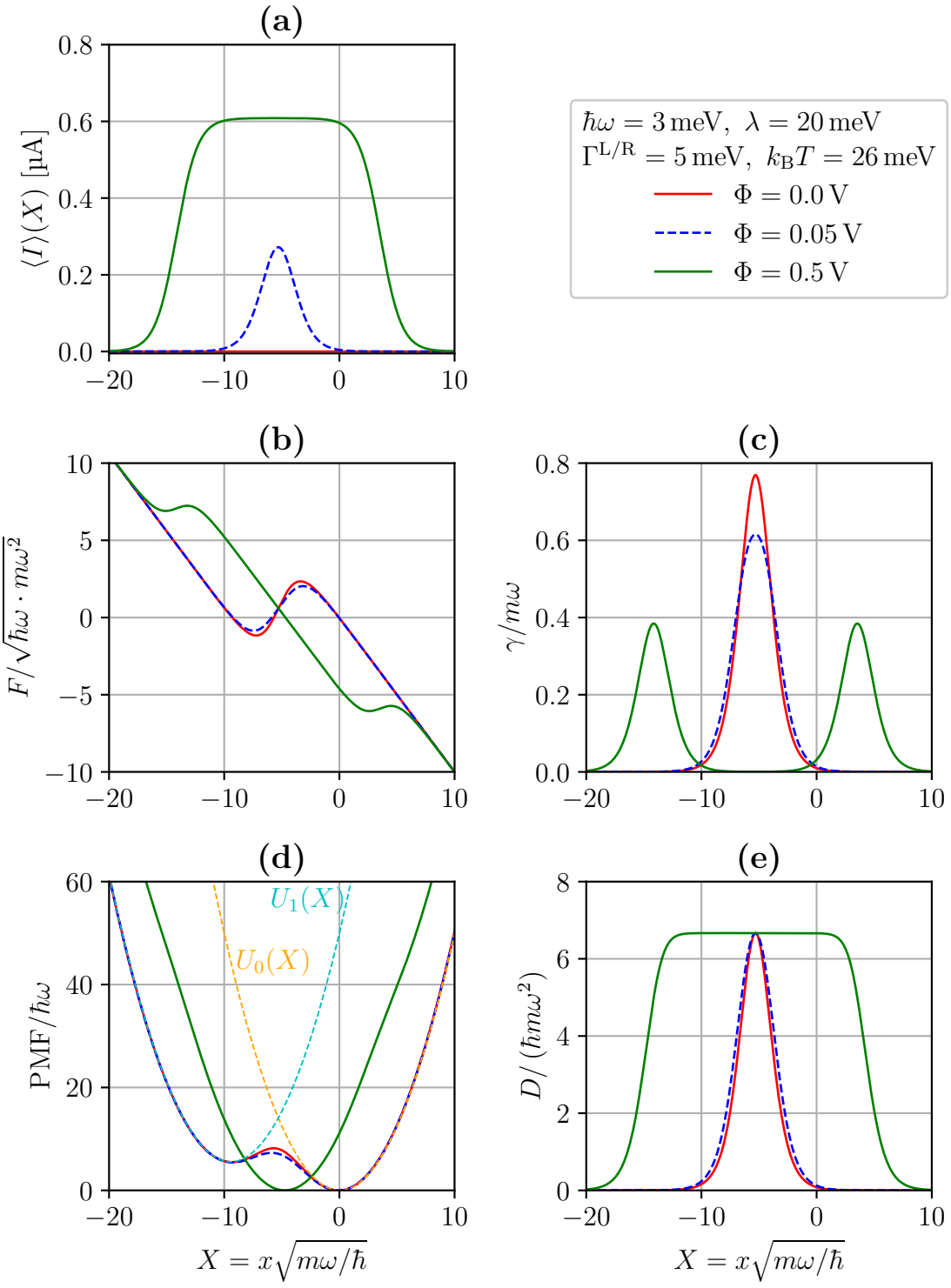

Figure 3.6: Instantaneous current, $\langle I \rangle(X)$, current-induced forces and potential of mean force, PMF(X), of a Holstein model. Parameters not given in the legend: $\varepsilon_0 = 150\,\mathrm{meV}$.

at zero bias voltage, the fluctuation-dissipation theorem between the diffusion and the

electronic friction is satisfied, namely $D = k_\mathrm{B}T \cdot \gamma$ or in dimensionless units

$$\frac{D}{\hbar m\omega^2} = \frac{k_\mathrm{B}T}{\hbar\omega} \cdot \frac{\gamma}{m\omega} = \frac{26}{3} \cdot \frac{\gamma}{m\omega}.$$

If we apply a finite bias voltage to the junction, the fluctuation-dissipation theorem is no longer fulfilled, as the electronic friction, γ, splits into two separate peaks, whereas the diffusion coefficient, D, shows a broad plateau. To understand this behavior, we look again at the conditions for charge transport. The friction peaks are located precisely on the resonances, $\mu_{\mathrm{L/R}} = U_1 - U_0$, which lie at $X = 3.5$ and $X = -14.1$ for $\Phi = 0.5\,\mathrm{V}$, as illustrated in Fig. 3.7**(b)**. At these resonances, the creation of electron-hole pairs in the left and right electrodes can occur [27, 40]. While this process does not contribute to the net current, it does influence the vibrational mode by impeding its movement in order to maintain the resonance state. This manifests itself in a frictional force of the electrons on the vibration, while the energy dissipated by the friction serves to create the electron-hole pairs. Because of the finite broadening of the friction peaks, due to $k_\mathrm{B}T > 0$, the friction splits into two separate peaks not immediately for $\Phi > 0$, but only when $\Phi \gg k_\mathrm{B}T/\mathrm{e}$. The stochastic force, on the other hand, arises primarily from random collisions between the vibrating system and electrons flowing through the junction. Therefore, the diffusion constant is positive when the current is positive, which is satisfied in between the two resonances, $-14.1 < X < 3.5$ at $\Phi = 0.5\,\mathrm{V}$. Hence, both diffusion and current show a similar plateau shape.

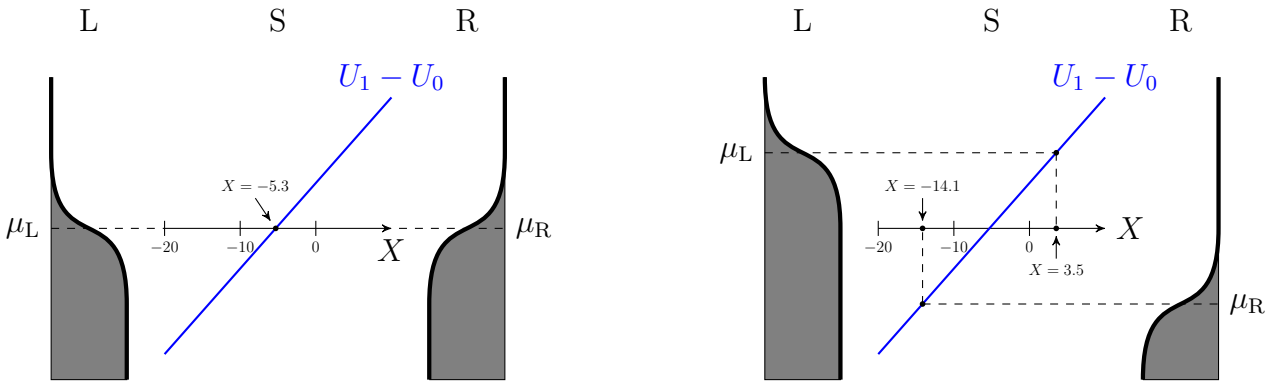

(a) $\Phi = 0.0\,\mathrm{V}$. **(b)** $\Phi = 0.5\,\mathrm{V}$.

Figure 3.7: Illustration of the energy difference, $U_1 - U_0$, between the charged and neutral state of the Holstein model. At zero bias voltage, depicted in **(a)**, the resonances of the chemical potentials with the energy difference, $\mu_{\mathrm{L/R}} = U_1 - U_0$, coincide at $X \approx -5.3$. At a bias voltage of $\Phi = 0.5\,\mathrm{V}$, illustrated in **(b)**, the resonances are split. We find the resonance with μ_L at $X \approx 3.5$, and the resonance with μ_R at $X \approx -14.1$.

Finally, we compare our results with those of [27]. In Fig. 1 of their paper, the authors of [27] depicted the electronic friction for the same system considered here, calculated with the same Born-Markov approximation and also from the exact hierarchical equations of motion (HEOM) and non-equilibrium Green's functions (NEGF) approaches. First, it can be seen that our Born-Markov result matches theirs. Further, we find that the Born-Markov approximation also gives physically realistic values and for this example shows only minimal deviations from the exact calculations using HEOM and NEGF.

Now that we have examined the basic properties of the current-induced forces for the Holstein model, we will give, in the following, a comprehensive analysis of this model in the semi-classical approximation. As aforementioned, we will do so by calculating expectation values of the semi-classical steady state, as described in Secs. 2.4.4 and 2.4.5, and comparing them to a fully quantum-mechanical calculation.

3.4 Semi-classical results and comparison to quantum calculation

In Sec. 2.4, we derived the Langevin equation of motion under the assumption that the vibrational dynamics is much slower than the electronic dynamics. The time scale in which the vibrational dynamics proceeds is given by the natural frequency ω. On the other hand, the typical time scale of the electron transport is given by the coupling to the electrodes. For the vibrational mode, it does not matter if an electronic interaction takes place with the left or right electrode. Therefore, the relevant time scale for the electron dynamics is determined by the total electrode coupling, $\Gamma^{\mathrm{L}} + \Gamma^{\mathrm{R}}$. The relationship between the vibrational frequency and the electrode coupling defines three different parameter regimes:

(1) In the *classical* regime, with $\hbar\omega \ll \Gamma^{\mathrm{L}} + \Gamma^{\mathrm{R}}$, the assumption of slow vibrational dynamics should be satisfied. Therefore, we expect the semi-classical approach to work well.

(2) In the *intermediate* regime, with $\hbar\omega \sim \Gamma^{\mathrm{L}} + \Gamma^{\mathrm{R}}$, both time scales are on the same order of magnitude. At first, it is unclear whether the semi-classical approach will break down or still deliver accurate results.

(3) In the *quantum* regime, with $\hbar\omega \gg \Gamma^{\mathrm{L}} + \Gamma^{\mathrm{R}}$, the assumed time-scale separation is not satisfied, and the vibrational coordinate moves at the same time scale as the electron transport. Therefore, we expect quantum effects to show up, causing the semi-classical approach to break down.

To find out in which parameter regimes the semi-classical approach is applicable, we will calculate the semi-classical dynamics for all of them, and compare the results with a fully quantum-mechanical calculation.

3.4.1 Classical regime

For our studies in the *classical* regime, where $\hbar\omega \ll \Gamma^{\mathrm{L}} + \Gamma^{\mathrm{R}}$, we use mostly similar parameters for the Holstein system as in the previous section. In particular, we keep the natural frequency of the vibrational mode at $\hbar\omega = 3\,\mathrm{meV}$, and also the temperature at $k_{\mathrm{B}}T = 26\,\mathrm{meV}$, which corresponds to $T \approx 300\,\mathrm{K}$. For the coupling to the electrodes, we choose two different values, $\Gamma^{\mathrm{L}} = \Gamma^{\mathrm{R}} \in \{5\,\mathrm{meV}, 10\,\mathrm{meV}\}$. In Sec. 3.2, we found that the electron-vibrational coupling has a significant effect on transport; therefore, we investigate weak, intermediate, and strong coupling, $\lambda \in \{1\,\mathrm{meV}, 2\,\mathrm{meV}, 5\,\mathrm{meV}\}$. To better identify the impact of changing the vibrational parameters, we keep the energy of the electronic level fixed. As we have seen in Sec. 3.2, the energy that matters for the dynamics is the renormalized energy level $\varepsilon_1 = \varepsilon_0 - \lambda^2/\hbar\omega$. Therefore, we fix $\varepsilon_1 = 150\,\mathrm{meV}$. The resulting current-induced forces are shown in Fig. 3.8.

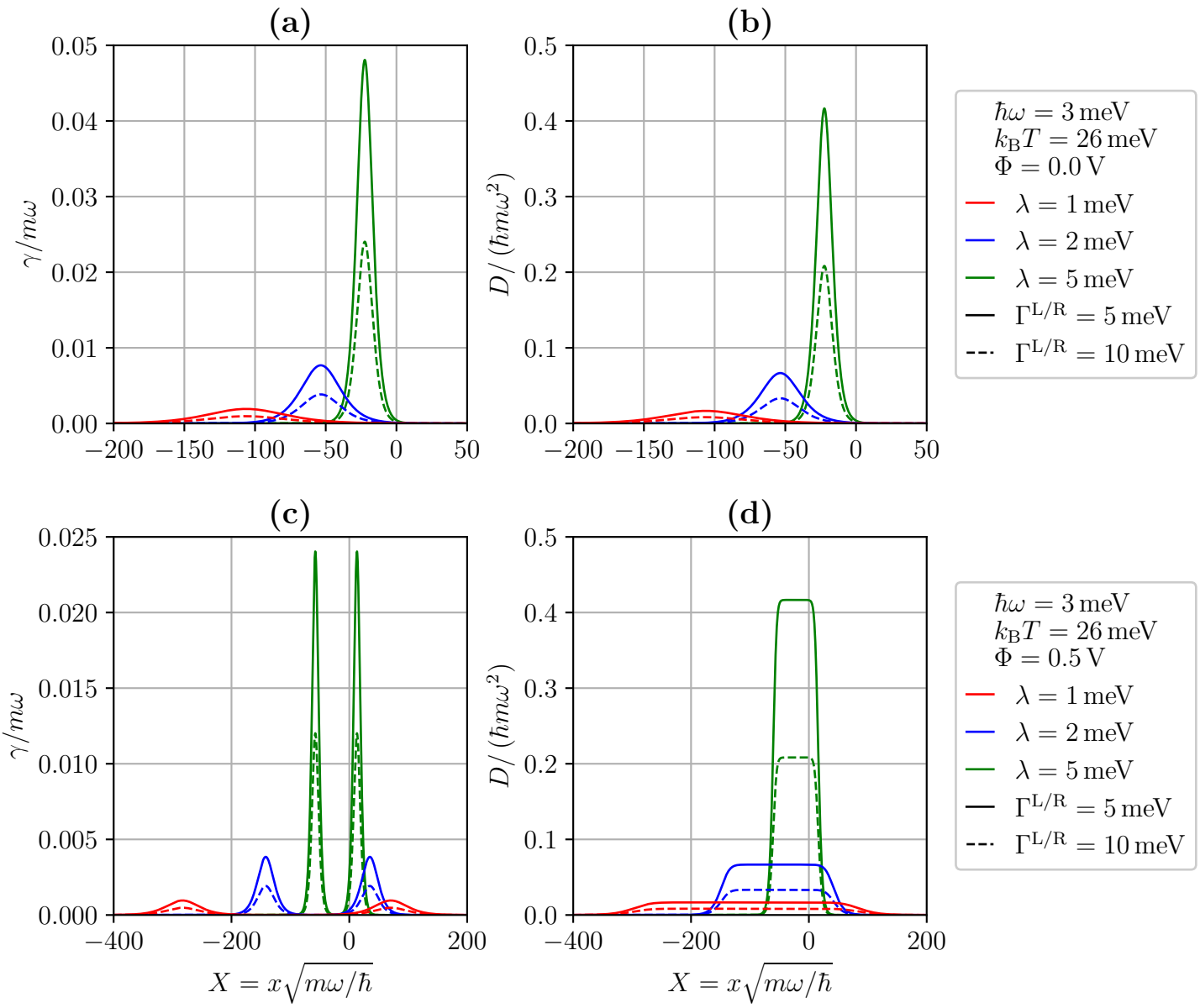

Figure 3.8: Current-induced forces for a Holstein model. Parameters not given in the legend: $\varepsilon_1 = 150\,\mathrm{meV}$.

It can be seen that the friction and diffusion in Fig. 3.8 are very similar to Fig. 3.6 from the previous section. The same also holds for the current and mean force, which is why we do not plot them here again. Therefore, let us directly move on to discussing the effect of the different λ. For smaller λ, the friction and diffusion are stretched over a larger range of X values by a factor of 2.5 and 5, respectively, corresponding to the ratio of the λ values. This behavior follows immediately from the linear coupling term, $\sqrt{2}\lambda X$. At the same time, this also leads to an overall decrease in the value of γ and D. The larger electrode coupling, $\Gamma^{\mathrm{L/R}} = 10\,\mathrm{meV}$, results in a halving of γ and D. This is because, with increased electrode coupling, the electrons spend less time in the junction, which reduces the magnitude of the current-induced forces. The electric current, which is not depicted here, exhibits a similar stretching in X direction as the diffusion, but its value does not change with λ, only when changing $\Gamma^{\mathrm{L/R}}$. As we have

seen before, the current is proportional to $\Gamma^{\mathrm{L/R}}$.

	Grid spacing	Equilibration time	
	ΔX	$\Gamma^{\mathrm{L/R}} = 5\,\mathrm{meV}$	$\Gamma^{\mathrm{L/R}} = 10\,\mathrm{meV}$
$\lambda = 1\,\mathrm{meV}$	0.5	$200\,000\,\omega t$	$200\,000\,\omega t$
$\lambda = 2\,\mathrm{meV}$	0.2	$30\,000\,\omega t$	$100\,000\,\omega t$
$\lambda = 5\,\mathrm{meV}$	0.1	$5\,000\,\omega t$	$5\,000\,\omega t$

Table 3.1: Grid spacings and equilibration times chosen for the calculation of the semi-classical steady state of a Holstein model with $\varepsilon_1 = 150\,\mathrm{meV}$, $\hbar\omega = 3\,\mathrm{meV}$, and $k_{\mathrm{B}}T = 26\,\mathrm{meV}$.

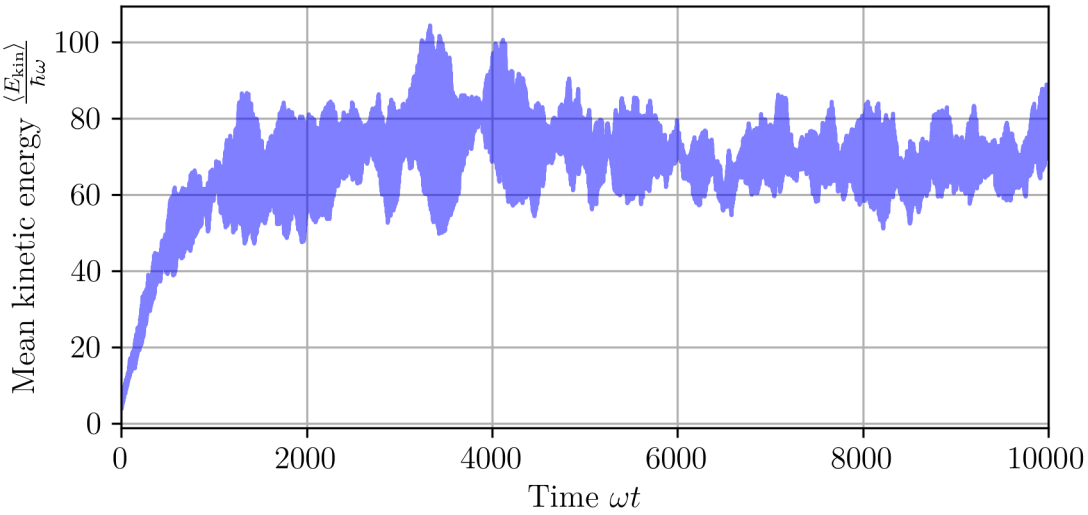

Figure 3.9: Time evolution of the mean kinetic energy of a group of 100 Langevin trajectories for a Holstein model with $\varepsilon_1 = 150\,\mathrm{meV}$, $\hbar\omega = 3\,\mathrm{meV}$, $\lambda = 5\,\mathrm{meV}$, $\Gamma^{\mathrm{L}} = \Gamma^{\mathrm{R}} = 10\,\mathrm{meV}$, $k_{\mathrm{B}}T = 26\,\mathrm{meV}$ at a bias voltage of $\Phi = 0.6\,\mathrm{V}$. It can be seen that the mean kinetic energy increases for $0 < \omega t < 1000$, but then stays between $60\,\hbar\omega$ and $80\,\hbar\omega$ for later times, indicating that the steady state is reached. The fluctuation of the depicted mean kinetic energy for 100 trajectories is still significant in the steady state, however, which is why we calculate the final expectation values using 500 trajectories, from which 100 statistically independent samples are drawn each, giving a total of 50 000 coordinate samples.

In the next step, we calculate the steady-state expectation values $\langle I\rangle^{\mathrm{ss}}$, $\langle X\rangle^{\mathrm{ss}}$, $\langle X^2\rangle^{\mathrm{ss}}$, $\langle P\rangle^{\mathrm{ss}}$, and $\langle P^2\rangle^{\mathrm{ss}}$. For this, we use the procedure discussed in Secs. 2.4.4 and 2.4.5. The grid spacings and equilibration times chosen for the different parameters are indicated in Tab. 3.1. To determine the equilibration time required, we propagate a group of 100 trajectories for an increasing number of time steps and calculate the respective average kinetic energy, $\langle E_{\mathrm{kin}}\rangle(t)$. The steady state is assumed to be reached when the average kinetic energy remains approximately constant in time. Since the equilibration takes longer for higher bias voltage, we carry out this procedure for each set of parameters at the highest considered voltage, which is $\Phi = 0.6\,\mathrm{V}$ here. The resulting kinetic energy curve is shown for one set of parameters in Fig. 3.9. Accord-

ing to it, we choose an equilibration time of $5\,000\,\omega t$ for the parameters $\lambda = 5\,\mathrm{meV}$, $\Gamma^{\mathrm{L/R}} = 10\,\mathrm{meV}$.

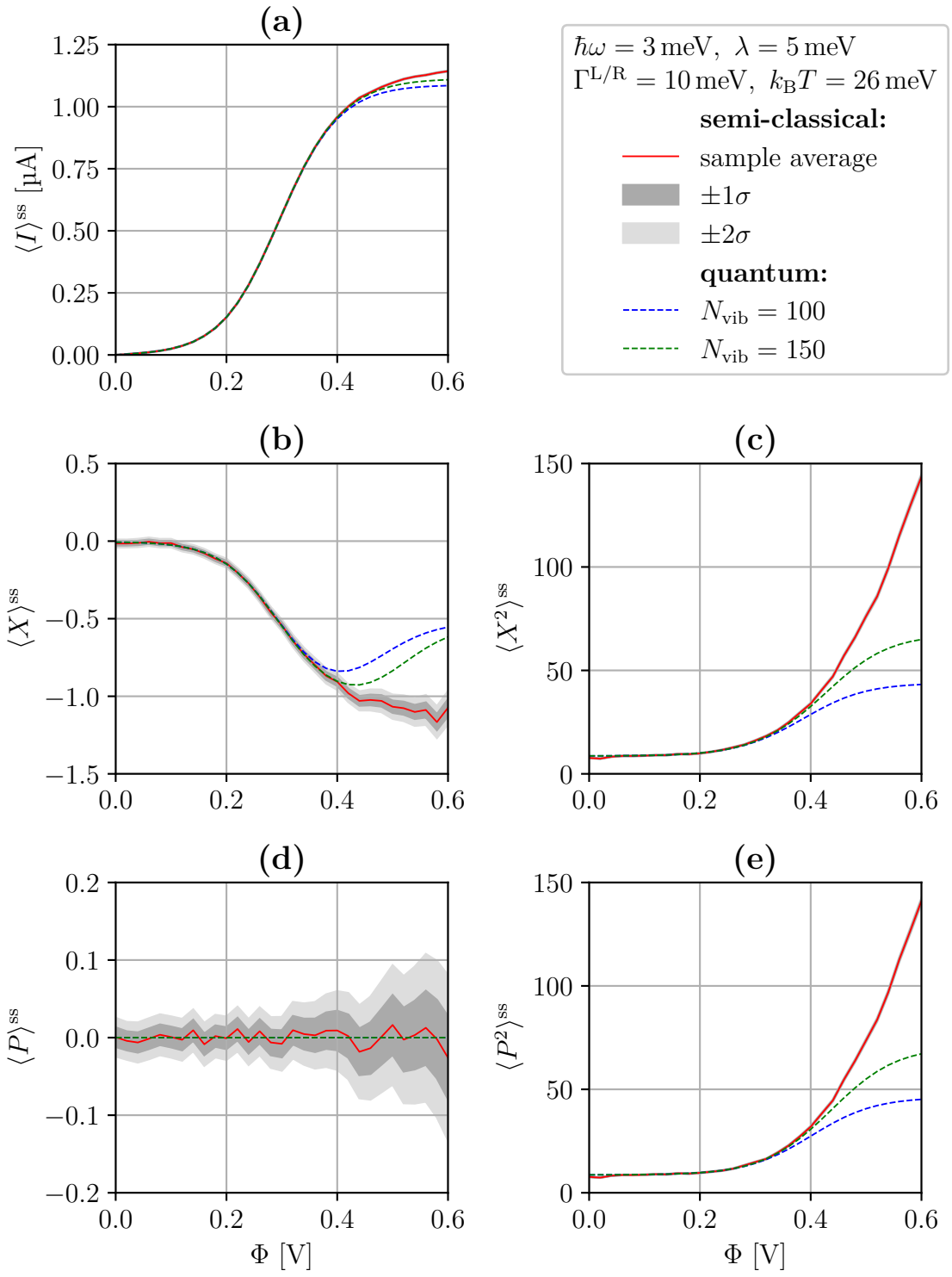

Figure 3.10: Comparison of semi-classical and quantum expectation values for a Holstein model. Parameters not given in the legend: $\varepsilon_1 = 150\,\mathrm{meV}$.

For comparison, we calculate the expectation values also using the purely quantum-mechanical approach from Sec. 2.2. The semi-classical and quantum results are shown

in Fig. 3.10, again for the exemplary parameters $\lambda = 5\,\mathrm{meV}$, $\Gamma^{\mathrm{L/R}} = 10\,\mathrm{meV}$. First, we note that the semi-classical result for $\langle P\rangle^{\mathrm{ss}}$ is consistently compatible with zero. This is again an indication that we have chosen a sufficient equilibration time.

The electric current shows a broad step at $\Phi = 0.3\,\mathrm{V}$, which corresponds to the crossing of $\mu_{\mathrm{L}} = \varepsilon_1$, as we discussed previously in Sec. 3.2. However, the additional steps at $\mu_{\mathrm{L}} = \varepsilon_1 + v \cdot \hbar\omega$, which we found there, are not visible here because the width of the individual steps, given by $k_{\mathrm{B}}T = 26\,\mathrm{meV}$, is much larger here than their spacing of $\hbar\omega = 3\,\mathrm{meV}$. The semi-classical and quantum results agree very well. Only at large bias voltage, the quantum calculations predict a slightly smaller current than the semi-classical approach.

The expectation value $\langle X\rangle^{\mathrm{ss}}$ shows a similar step at $\Phi = 0.3\,\mathrm{V}$. However, the quantum results here deviate more significantly from the semi-classical one for $\Phi > 0.3\,\mathrm{V}$, with the difference becoming smaller for a larger number of vibrational basis states, N_{vib}, though.

The curves for $\langle X^2\rangle^{\mathrm{ss}}$ and $\langle P^2\rangle^{\mathrm{ss}}$ are very similar to each other. Up to $\Phi = 0.3\,\mathrm{V}$, we find good agreement between the quantum and semi-classical calculation again. For $\Phi > 0.3\,\mathrm{V}$, however, a large discrepancy arises. The semi-classical curves continue their essentially exponential growth and reach a value of > 100 already below $\Phi = 0.6\,\mathrm{V}$. The quantum results, on the other hand, approach their infinite bias limit, which for a fixed number of basis states, N_{vib}, is $\langle X^2\rangle^{\mathrm{ss}} = \langle P^2\rangle^{\mathrm{ss}} = N_{\mathrm{vib}}/2$. This means that the quantum calculations are no longer converged for $\Phi > 0.3\,\mathrm{V}$, and apparently, a much larger $N_{\mathrm{vib}} \gg 100$ would be required to achieve convergence up to $\Phi = 0.6\,\mathrm{V}$. Though, increasing N_{vib} from 100 to 150 already leads to a slightly better result. We conclude that, in the considered case, the semi-classical approach is numerically favorable over the quantum calculation, and it agrees with the fully quantum result wherever we achieved converged results for the latter.

Next, we look at the other parameter values, λ and $\Gamma^{\mathrm{L/R}}$, as well. For this, we focus on the electric current and the average vibrational excitation, $\langle N\rangle^{\mathrm{ss}}$. The results for all considered parameter sets are presented collectively in Fig. 3.11.

In general, we find similar behavior for all six parameter combinations considered. In contrast to Sec. 3.2, the electric currents of the systems considered here show only a minimal Franck-Condon blockade for the different electronic-vibrational couplings λ. This is because the Franck-Condon blockade causes a delay in the current increase on the order of $\mathrm{e} \cdot \Delta\Phi \propto \lambda^2/\hbar\omega$ [54], as mentioned in Sec. 3.2, which is less than $0.01\,\mathrm{V}$ for all three λ considered here. Therefore, the current-voltage curves are very similar despite the different λ. The different electrode coupling, $\Gamma^{\mathrm{L/R}} = 5\,\mathrm{meV}$, only has the effect of halving the current, which we have already found in Sec. 2.3.

The semi-classical curves for $\langle N\rangle^{\mathrm{ss}}$ show the same exponential increase we observed earlier for $\langle X^2\rangle^{\mathrm{ss}}$ and $\langle P^2\rangle^{\mathrm{ss}}$. The results for the different $\Gamma^{\mathrm{L/R}}$ are almost identical. The different λ, on the other hand, show a distinct effect. The smaller λ, the faster the exponential increase. For instance, the system with $\lambda = 1\,\mathrm{meV}$ already reaches an average vibrational excitation of 200 at $\Phi = 0.5\,\mathrm{V}$, while the system with $\lambda = 5\,\mathrm{meV}$ remains below 150 up to $0.6\,\mathrm{V}$. In other words, the weaker the electronic-vibrational coupling, the more unstable the molecular junction. This is the same vibrational instability effect we already discussed in Sec. 3.2. It results from the fact that vibrational relaxation via electron-hole pair creation in the electrodes is increasingly suppressed for weaker coupling by the Franck-Condon transition elements.

The quantum results for $\langle N\rangle^{\mathrm{ss}}$ agree well with the semi-classical curves up to about

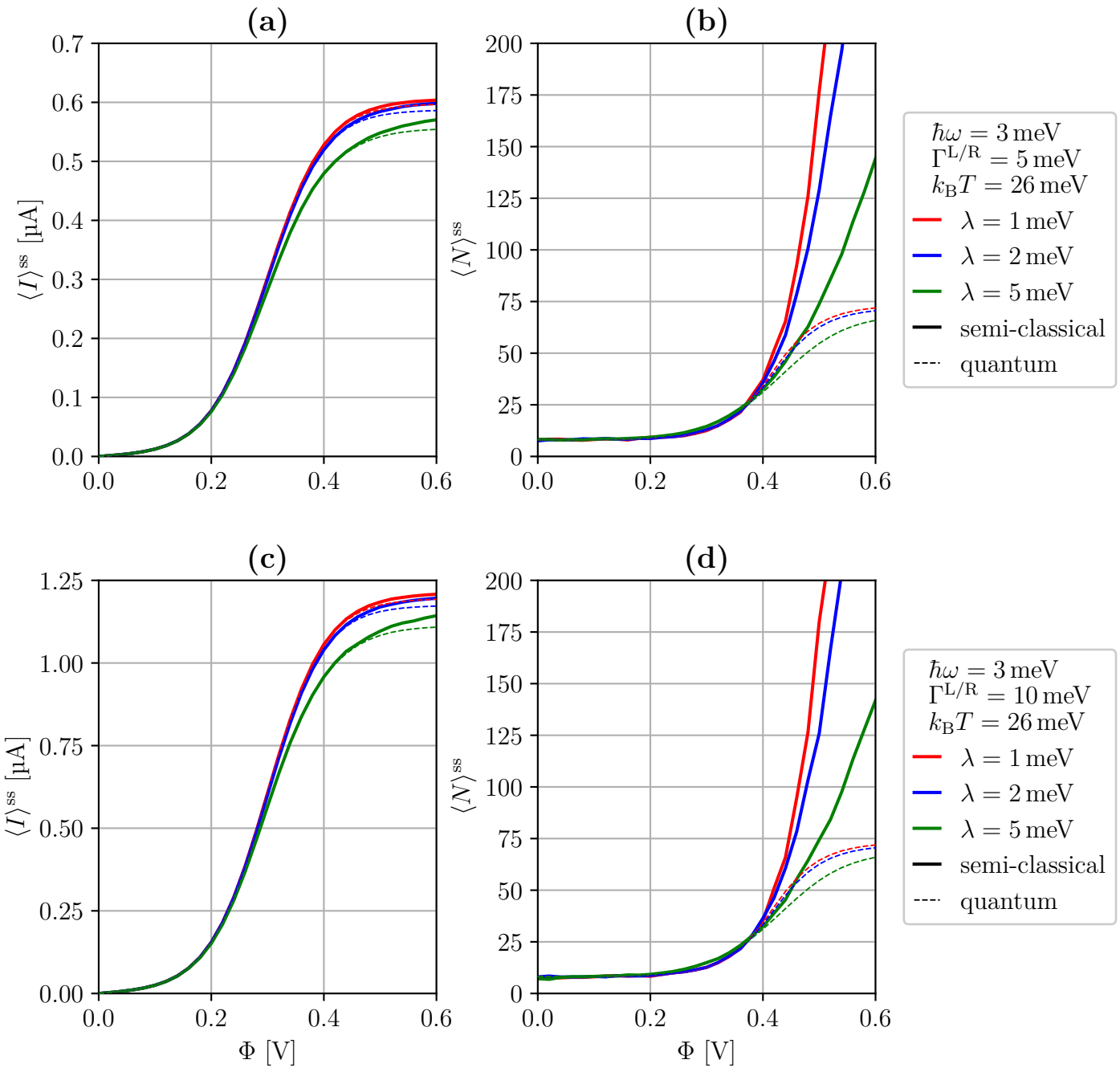

Figure 3.11: Comparison of semi-classical and quantum expectation values for a Holstein model. Parameters not given in the lgend: $\varepsilon_1 = 150\,\mathrm{meV}$, $N_{\mathrm{vib}} = 150$.

0.3 V to 0.4 V. Beyond that, they approach the infinite bias limit, here $N_{\mathrm{vib}}/2 = 75$, similar to our previous finding. Therefore, the quantum results are again not converged here. Nevertheless, the results for the electric current deviate only slightly from the semi-classical calculation. Considering different N_{vib}, we again find a convergence behavior towards the semi-classical curves for increasing N_{vib}. The individual results for this are not depicted here for brevity.

We conclude that in the considered classical regime, the semi-classical approach agrees with the quantum calculation wherever we achieved converged results for the latter. Hence, we called this the classical regime. Depending on the parameters, the

semi-classical calculation may be preferable in terms of computational cost. However, a review of Tab. 3.1 shows that this is only the case for $\lambda \gtrsim \hbar\omega$. For $\lambda \lesssim \hbar\omega$ with equilibration times of $> 100\,000\,\omega t$, the computational effort is comparable to a fully quantum calculation, maybe even larger if only the electric current is of interest.

3.4.2 Intermediate regime

Next, we examine the capabilities of the semi-classical description by turning to the *intermediate* regime, where the natural oscillation frequency $\hbar\omega$ is on the order of the total electrode coupling, $\Gamma^{\mathrm{L}}+\Gamma^{\mathrm{R}}$, and the thermal energy, $k_{\mathrm{B}}T$. To have this, we choose $\hbar\omega = 30\,\mathrm{meV}$ and keep the already known values $\Gamma^{\mathrm{L}} = \Gamma^{\mathrm{R}} \in \{5\,\mathrm{meV}, 10\,\mathrm{meV}\}$. We further keep the same parameters as before, namely $\varepsilon_1 = 150\,\mathrm{meV}$, $k_{\mathrm{B}}T = 26\,\mathrm{meV}$; and for the electronic-vibrational coupling, we choose $\lambda \in \{10\,\mathrm{meV}, 20\,\mathrm{meV}, 50\,\mathrm{meV}\}$ to get the same ratios $\lambda/\hbar\omega$ as previously.

	Grid spacing	Equilibration time	
	ΔX	$\Gamma^{\mathrm{L/R}} = 5\,\mathrm{meV}$	$\Gamma^{\mathrm{L/R}} = 10\,\mathrm{meV}$
$\lambda = 10\,\mathrm{meV}$	0.1	$10\,000\,\omega t$	$30\,000\,\omega t$
$\lambda = 20\,\mathrm{meV}$	0.1	$5\,000\,\omega t$	$5\,000\,\omega t$
$\lambda = 50\,\mathrm{meV}$	0.1	$2\,000\,\omega t$	$2\,000\,\omega t$

Table 3.2: Grid spacings and equilibration times chosen for the calculation of the semi-classical steady state of a Holstein model with $\varepsilon_1 = 150\,\mathrm{meV}$, $\hbar\omega = 30\,\mathrm{meV}$, and $k_{\mathrm{B}}T = 26\,\mathrm{meV}$.

First, we calculate the current-induced forces. The results are depicted in Fig. 3.12; they are very much analogous to the previous section. Using the procedure from Secs. 2.4.4 and 2.4.5, we obtain the semi-classical expectation values of the electric current, $\langle I\rangle^{\mathrm{ss}}$, and of the vibrational excitation, $\langle N\rangle^{\mathrm{ss}}$. The required equilibration times and the chosen grid spacings are indicated in Tab. 3.2. For comparison, we also calculate the expectation values fully quantum-mechanically. Since $\hbar\omega$ is 10-times larger than in the previous section, a maximum number of $N_{\mathrm{vib}} = 100$ is sufficient. The results are presented collectively for all considered parameter combinations in Fig. 3.13.

Starting with the electric current, we find again essentially a single step, which, for $\lambda \in \{10\,\mathrm{meV}, 20\,\mathrm{meV}\}$, is centered around $\Phi = 0.3\,\mathrm{V}$ as previously, corresponding again to the crossing of $\mu_{\mathrm{L}} = \varepsilon_1$. For the large electronic-vibrational coupling, $\lambda = 50\,\mathrm{meV}$, the step is noticeably shifted towards larger Φ. This is again due to the Franck-Condon blockade discussed in Sec. 3.2. For $\lambda \in \{10\,\mathrm{meV}, 20\,\mathrm{meV}\}$, the quantum and semi-classical results agree; only at higher bias voltage, $\Phi > 0.8\,\mathrm{V}$, the quantum calculations underestimate the current, which is again due to insufficient N_{vib}, as we will discuss in the next paragraph. For the stronger coupling, $\lambda = 50\,\mathrm{meV}$, there is a notable deviation between quantum and semi-classical results already at smaller voltages. The semi-classical result underestimates the current around its step significantly compared to the quantum result. However, the curves agree very well again at higher bias voltage, $\Phi > 0.8\,\mathrm{V}$.

Looking at the vibrational excitation, $\langle N\rangle^{\mathrm{ss}}$, we also find similar results as in the previous section. All curves show an exponential rise in the excitation with increasing bias voltage. As we considered $N_{\mathrm{vib}} = 100$ for the quantum calculations, their respective

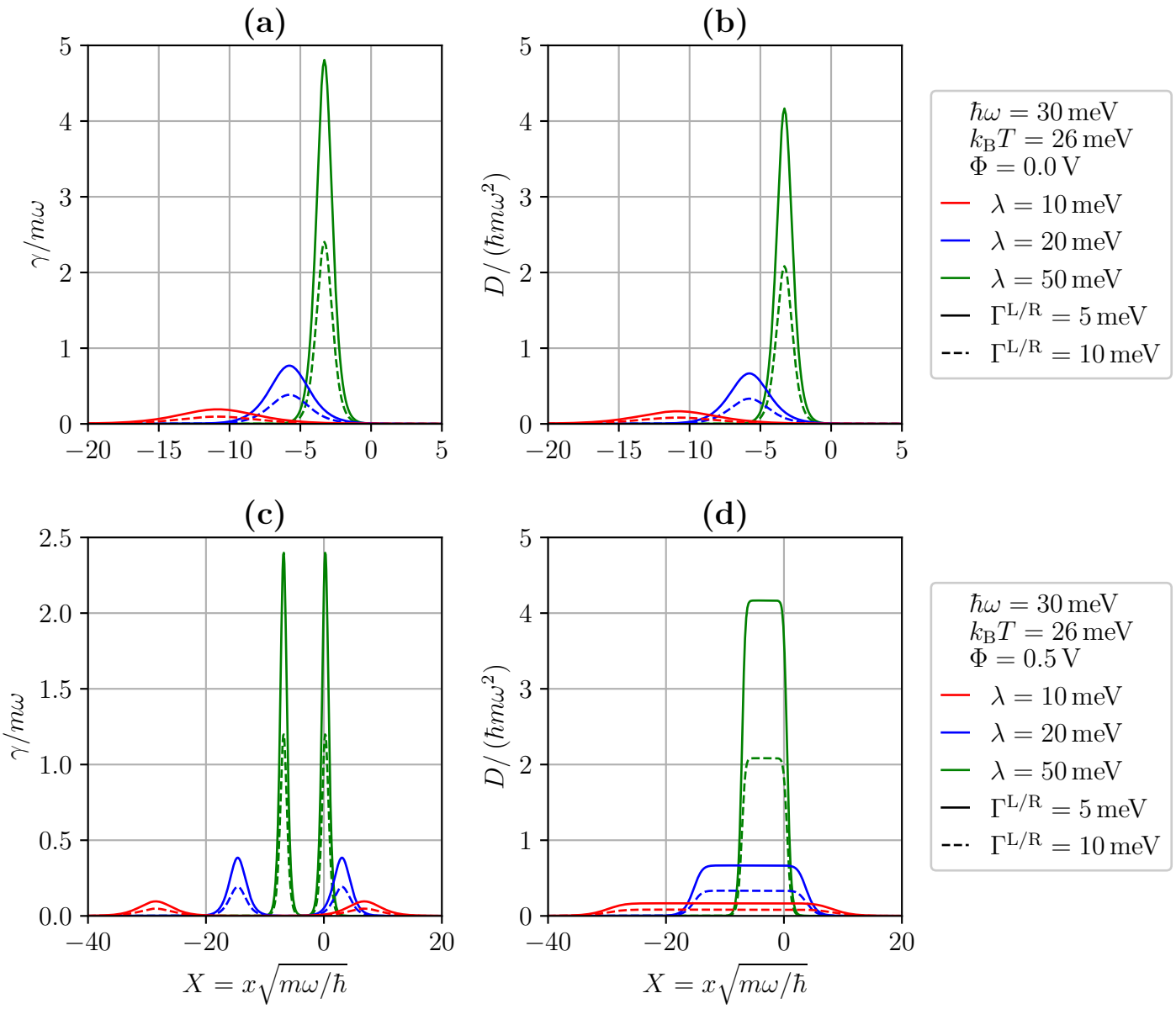

Figure 3.12: Current-induced forces for a Holstein model. Parameters not given in the legend: $\varepsilon_1 = 150\,\mathrm{meV}$.

excitation curves cannot exceed the infinite bias limit of $N_\mathrm{vib}/2 = 50$, which they indeed converge to for $\Phi > 0.8\,\mathrm{V}$ and $\Phi > 1.1\,\mathrm{V}$, respectively, for $\lambda \in \{10\,\mathrm{meV}, 20\,\mathrm{meV}\}$. For the strong coupling, $\lambda = 50\,\mathrm{meV}$, on the other hand, the Franck-Condon blockade slows the increase in vibrational excitation such that it stays below $\langle N\rangle^\mathrm{ss} = 40$ until $\Phi = 1.5\,\mathrm{V}$. Consequently, the corresponding quantum result shows an ongoing growth over the entire range of bias voltages depicted here, and throughout agrees quite well with the semi-classical result.

We conclude that, whereas the quantum results for $\lambda \in \{10\,\mathrm{meV}, 20\,\mathrm{meV}\}$ are not converged at voltages higher than 0.7 V and 0.9 V, respectively, the quantum result for $\lambda = 50\,\mathrm{meV}$ is probably well converged up to 1.5 V. Therefore, poor convergence cannot be responsible for the deviation in electric current in the range $0.2\,\mathrm{V} < \Phi < 0.8\,\mathrm{V}$ at $\lambda = 50\,\mathrm{meV}$. Instead, the deviation must be due to a violation of our assumed time-scale

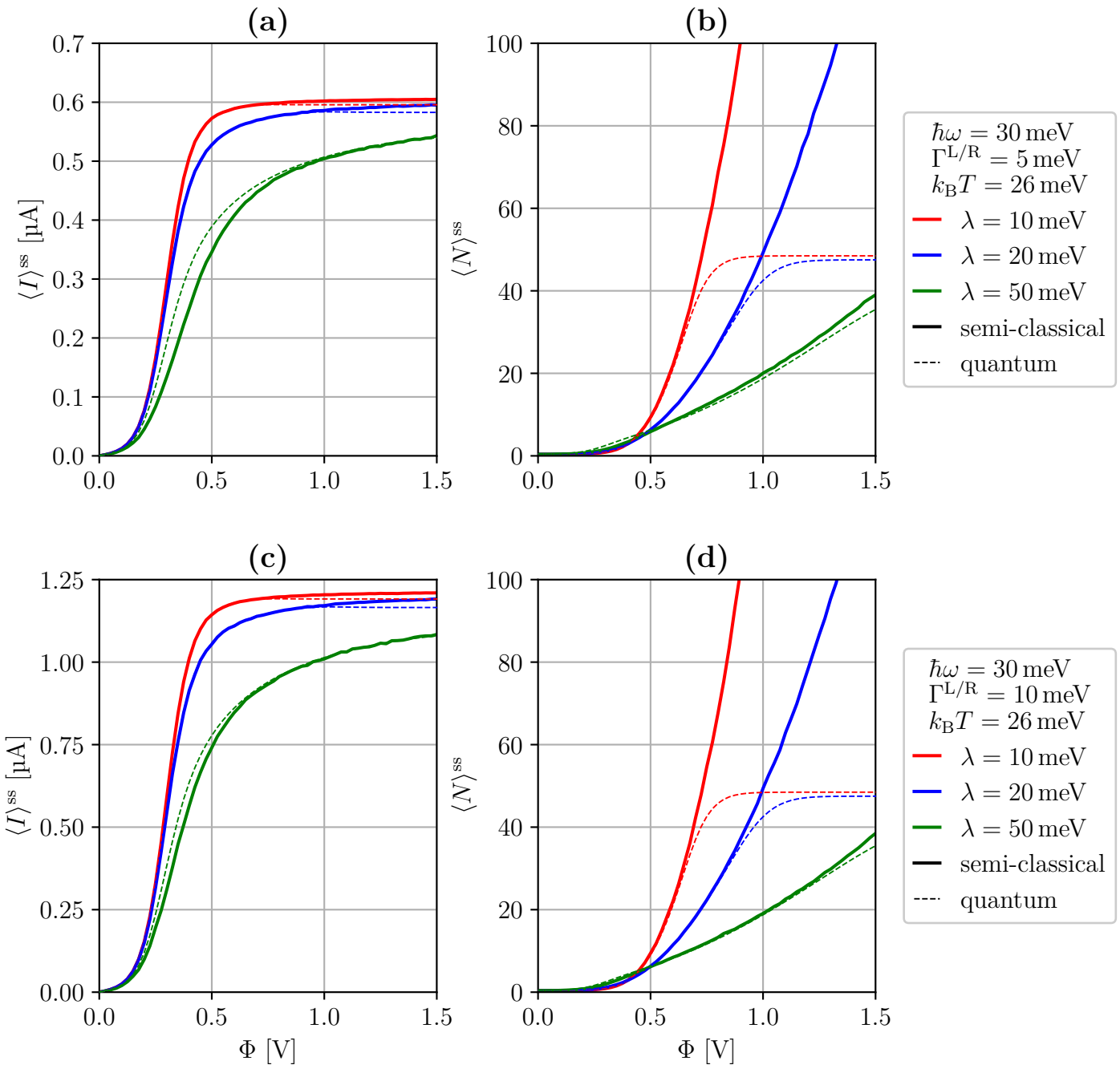

Figure 3.13: Comparison of semi-classical and quantum expectation values for a Holstein model. Parameters not given in the legend: $\varepsilon_1 = 150\,\mathrm{meV}$, $N_{\mathrm{vib}} = 100$.

separation between vibration and electron transport. This cannot be due to our choice of $\hbar\omega$, though, as the semi-classical approach works fine for the other two λ. Instead, the large λ is indeed the problem here. If λ becomes significantly larger than $\hbar\omega$, the latter is no longer a good estimate for the typical time scale of the vibration, because the large coupling increases the chance of electrons interacting with the vibrational mode on short time scales. Thereby, the assumed time-scale separation is violated because of $\lambda > \Gamma^{\mathrm{L}} + \Gamma^{\mathrm{R}}$ even for $\hbar\omega \sim \Gamma^{\mathrm{L}} + \Gamma^{\mathrm{R}}$. This claim is supported by the fact that the deviation is smaller for the larger $\Gamma^{\mathrm{L/R}} = 10\,\mathrm{meV}$.

In conclusion, we have established that the semi-classical approach is also applicable

in the intermediate regime, despite the fact that the requirement $\hbar\omega \ll \Gamma^{\mathrm{L}} + \Gamma^{\mathrm{R}}$ is not technically fulfilled. However, one should not consider too large electronic-vibrational coupling, because this may eventually break the time-scale separation regardless of $\hbar\omega$. Looking at Tab. 3.2, we also notice that the semi-classical calculation is now clearly favorable in terms of computational effort, with equilibration times of mostly $\leq 10\,000\,\omega t$, compared to the classical regime, where we required equilibration times $> 100\,000\,\omega t$ in some instances. This makes it a fairly good alternative to the fully quantum approach.

3.4.3 Quantum regime

To complete our study of the Holstein model, we also investigate the *quantum* regime, where $\hbar\omega \gg \Gamma^{\mathrm{L}} + \Gamma^{\mathrm{R}}$. We choose another 10-times larger natural oscillation frequency, $\hbar\omega = 300\,\mathrm{meV}$, and keep $\Gamma^{\mathrm{L}} = \Gamma^{\mathrm{R}} \in \{5\,\mathrm{meV}, 10\,\mathrm{meV}\}$ again. The further parameters are kept as previously, namely $\varepsilon_1 = 150\,\mathrm{meV}$, $k_{\mathrm{B}}T = 26\,\mathrm{meV}$; and for the electronic-vibrational coupling, we cover a large range of values by regarding $\lambda \in \{30\,\mathrm{meV}, 150\,\mathrm{meV}, 300\,\mathrm{meV}, 600\,\mathrm{meV}\}$.

	Grid spacing	Equilibration time	
	ΔX	$\Gamma^{\mathrm{L/R}} = 5\,\mathrm{meV}$	$\Gamma^{\mathrm{L/R}} = 10\,\mathrm{meV}$
$\lambda = 30\,\mathrm{meV}$	0.1	$5\,000\,\omega t$	$5\,000\,\omega t$
$\lambda = 150\,\mathrm{meV}$	0.02	$1\,000\,\omega t$	$1\,000\,\omega t$
$\lambda = 300\,\mathrm{meV}$	0.01	$1\,000\,\omega t$	$1\,000\,\omega t$
$\lambda = 600\,\mathrm{meV}$	0.005	$1\,000\,\omega t$	$1\,000\,\omega t$

Table 3.3: Grid spacings and equilibration times chosen for the calculation of the semi-classical steady state of a Holstein model with $\varepsilon_1 = 150\,\mathrm{meV}$, $\hbar\omega = 300\,\mathrm{meV}$, and $k_{\mathrm{B}}T = 26\,\mathrm{meV}$.

We start again by calculating the current-induced forces. The results, which are shown in Fig. 3.14, are very similar to what we have found in the previous sections. With the procedure from Secs. 2.4.4 and 2.4.5, we determine the semi-classical expectation values $\langle I \rangle^{\mathrm{ss}}$ and $\langle N \rangle^{\mathrm{ss}}$. As the considered electronic-vibrational couplings λ are fairly large, we have to choose sufficiently small grid spacings for the current-induced forces to achieve appropriate results. The equilibration times can, on the other hand, be chosen very small. The exact values are indicated in Tab. 3.3. For comparison, we calculate the expectation values fully quantum-mechanically as well. As the natural frequency $\hbar\omega$ is much larger than previously, smaller numbers of vibrational basis states, N_{vib}, are sufficient. Eventually, 100, 75, 50, and 25 turned out to be appropriate for the different $\lambda \in \{30\,\mathrm{meV}, 150\,\mathrm{meV}, 300\,\mathrm{meV}, 600\,\mathrm{meV}\}$, respectively. The electric current and vibrational excitation are plotted for the considered parameter sets altogether in Fig. 3.15.

Starting with the weakest electronic-vibrational coupling, $\lambda = 30\,\mathrm{meV}$, we first find that the electric current still displays the same step shape as in the previous regimes. The step is centered around $\Phi = 0.3\,\mathrm{V}$, corresponding again to the crossing of $\mu_{\mathrm{L}} = \varepsilon_1$. Surprisingly, the semi-classical curve captures the behavior of the electric current quite well, even though its underlying assumption $\hbar\omega \ll \Gamma^{\mathrm{L}} + \Gamma^{\mathrm{R}}$ is strongly violated. Solely at the saturation turning point, around $\Phi = 0.5\,\mathrm{V}$, the semi-classical calculation slightly

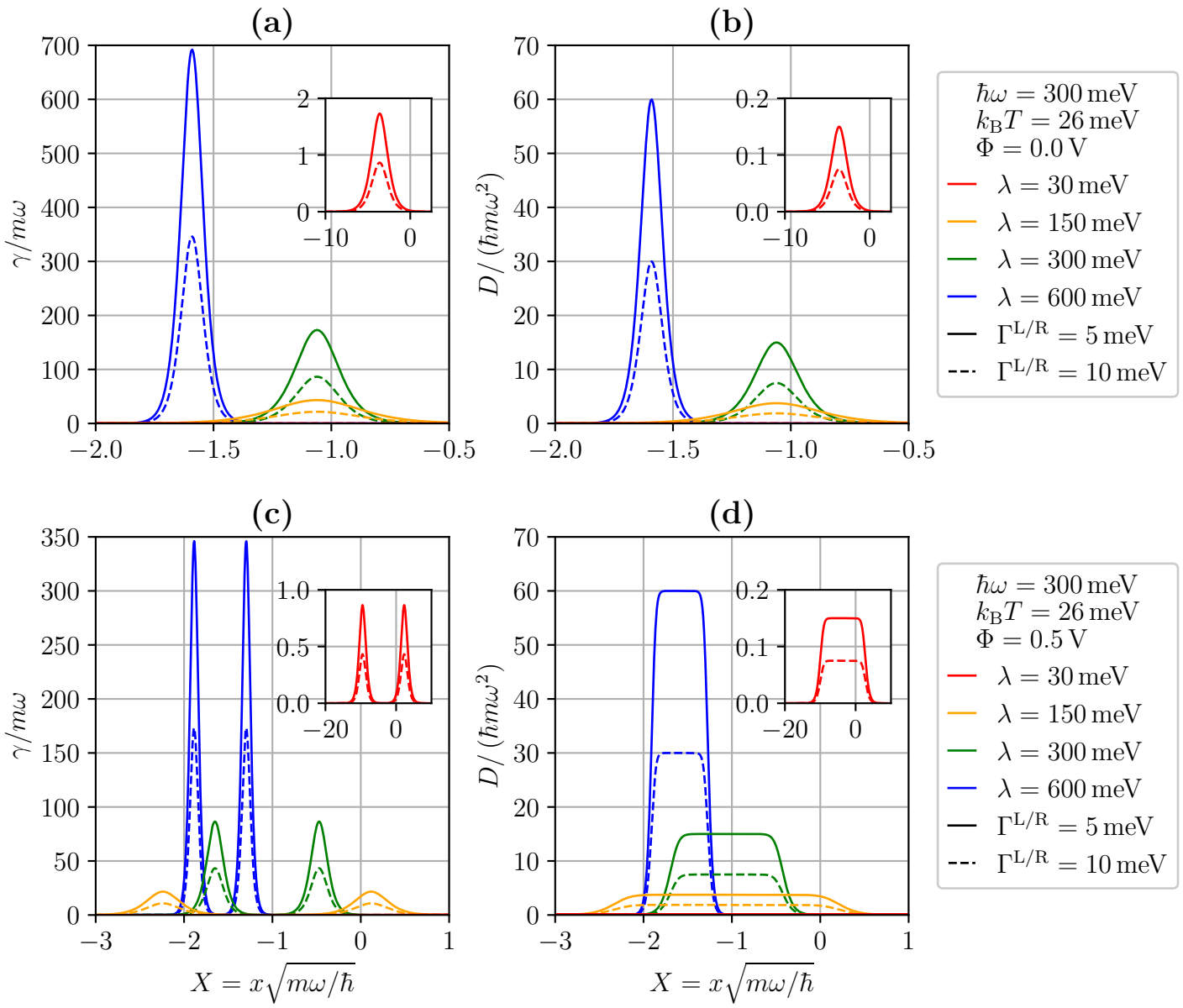

Figure 3.14: Current-induced forces for a Holstein model. Parameters not given in the legend: $\varepsilon_1 = 150\,\mathrm{meV}$.

underestimates the current and saturates to the maximum values of about 0.6 µA and 1.2 µA, respectively, only at slightly higher bias voltage. Evidently, the relationship between λ and $\Gamma^\mathrm{L}+\Gamma^\mathrm{R}$ is also important for the time-scale separation. This observation is a kind of counterpart to $\lambda = 50\,\mathrm{meV}$ in the intermediate regime. The behavior of the average vibrational excitation, however, is not at all reproduced correctly by the semi-classical curve. With the much larger $\hbar\omega = 300\,\mathrm{meV}$, the quantum result now clearly shows additional steps at $\mu_\mathrm{L} = \varepsilon_1 + n \cdot \hbar\omega$, similar to what we have seen in Sec. 3.2. The semi-classical calculation cannot capture this quantization by virtue of treating the vibration as a classical degree of freedom. In principle, the same additional steps are also found in the quantum calculation of the current. However, the effect of the Franck-Condon blockade is apparently so small that the major current step already occurs at $\mu_\mathrm{L} = \varepsilon_1$, and the additional later steps are no longer visible due to their small

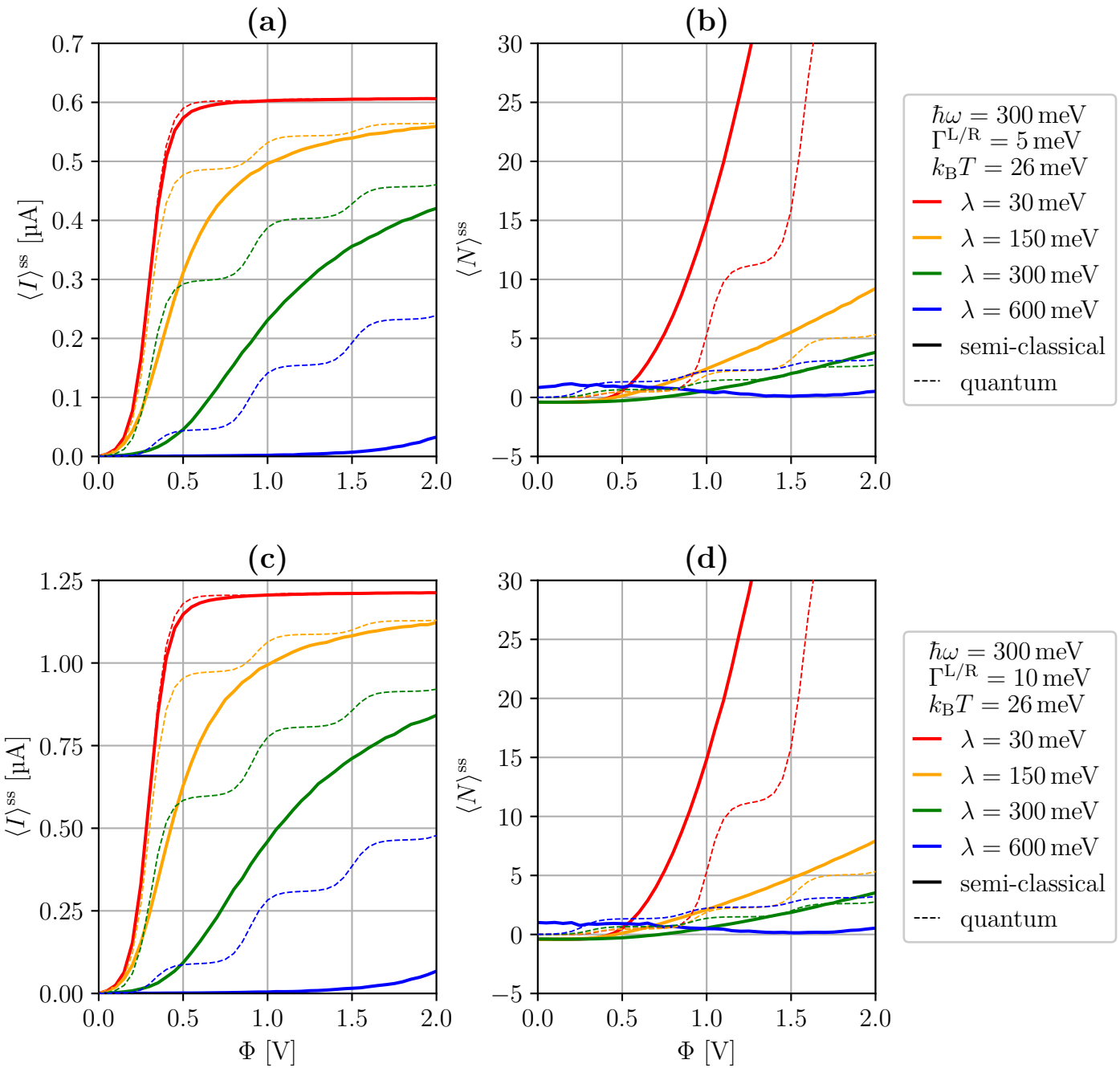

Figure 3.15: Comparison of semi-classical and quantum expectation values for a Holstein model. Parameters not given in the legend: $\varepsilon_1 = 150\,\mathrm{meV}$, $N_{\mathrm{vib}} = 100, 75, 50, 25$ for $\lambda = 30...600\,\mathrm{meV}$.

magnitude.

Turning to $\lambda = 150\,\mathrm{meV}$, additional steps also appear in the electric current. Thus, we now also find a clear deviation between semi-classical and quantum calculations for the current. As before, near the saturation turning point, the semi-classical calculation also underestimates the current. On the other hand, the vibrational excitation is consistently overestimated by the semi-classical curve, again similar to the case regarded beforehand.

Going to the strong electronic-vibrational couplings, $\lambda \geq \hbar\omega$, the deviation between

semi-classical and quantum calculations becomes even larger. The current is consistently underestimated by the semi-classical curve, whereas the vibrational excitation remains overestimated. The quantization features, that is, the steps corresponding to the resonances $\mu_{\mathrm{L}} = \varepsilon_1 + v \cdot \hbar\omega$, are naturally not reproduced by the semi-classical calculation. It is obvious that the semi-classical approach is not viable for the parameters considered in this regime. Hence, we called this the *quantum* regime.

Finally, it should be briefly noted that, for $\lambda \in \{30\,\mathrm{meV}, 150\,\mathrm{meV}, 300\,\mathrm{meV}\}$, the semi-classical vibrational excitation starts at $-\frac{1}{2}$ for $\Phi = 0$. Mathematically, the reason for this is the $-\frac{1}{2}$ term in Eq. (2.67). Physically, this is due to the missing zero-point energy. If we were to consider instead $\langle N + \frac{1}{2}\langle^{\mathrm{ss}} = \langle N\rangle^{\mathrm{ss}} + \frac{1}{2}$, the semi-classical curves would start at 0, whereas the quantum curves would start at $+\frac{1}{2}$ due to the quantum-mechanical zero point energy.

3.5 Conclusions

In this chapter, we have investigated the accurary of the semi-classical method against a fully quantum-mechanical calculation. To this end, we compared three distinct parameter regimes:

(1) In the *classical* regime, $\hbar\omega \ll \Gamma^{\mathrm{L}} + \Gamma^{\mathrm{R}}$, we found the semi-classical approach to be accurate. As the assumption of slow vibrational dynamics is commonly satisfied in this regime, this outcome is very much expected. For weak electronic-vibrational coupling, $\lambda < \hbar\omega$, however, the equilibration time required to reach the semi-classical steady state becomes very large, and the computational advantage over the fully quantum calculation shrinks. For $\lambda > \hbar\omega$, the semi-classical approach is definitely preferable in terms of computational effort, though.

(2) Surprisingly, the semi-classical calculation also delivers very accurate results in the *intermediate* regime, $\hbar\omega \sim \Gamma^{\mathrm{L}} + \Gamma^{\mathrm{R}}$, so long as the electronic-vibrational coupling is weak to intermediate, $\lambda \lesssim \hbar\omega$. For $\lambda > \hbar\omega$, however, the assumed time-scale separation appears to break down, and the semi-classical result no longer delivers accurate results for all considered voltages. In this regime, the semi-classical approach is generally less computationally expensive than a fully quantum-mechanical calculation. Hence, for $\lambda < \hbar\omega$, this regime is the optimal domain of application of the elaborated semi-classical method.

(3) Eventually, in the *quantum* regime, $\hbar\omega \gg \Gamma^{\mathrm{L}} + \Gamma^{\mathrm{R}}$, where the assumed time-scale separation is clearly violated, the semi-classical approach breaks down.

With this summary, we close our study of the Holstein model. In the next chapter, we will investigate a more complicated system containing one fast and one slow vibrational mode coupled to one electronic level.

Chapter 4

One-level two-mode model

In this chapter, we study a junction related to the Holstein model from the previous chapter, but featuring a second vibrational mode with a much higher natural frequency: the *one-level two-mode model* (1L2M model) [27]. The additional high-frequency vibration could describe, for example, an optical cavity similar to the model discussed in [55]. But one could also think of a molecule that contains two bonds of very different rigidity [27].

Since this system contains two vibrational modes, both of which have an infinite vibrational basis, a fully quantum-mechanical treatment is very computationally expensive. Therefore, we will generally consider the low-frequency mode in the semi-classical approximation derived in Sec. 2.4. Our goal is to analyze the transport characteristics of the 1L2M model and compare it to the Holstein model with only a single vibration, with a particular focus on how the addition of the second vibrational mode affects the stability of the low-frequency mode.

4.1 Model

To begin with, we define the fully quantum-mechanical Hamiltonian of the 1L2M model. The starting point for this is the Hamiltonian of the Holstein model, given in Eq. (3.2). In the potential energy surfaces, we add a second vibrational degree of freedom, whose displacement we also couple to the occupied state. Thus, we have

$$H_{\mathrm{S}} = U_0(\hat{X}_{\mathrm{hf}}, \hat{X}_{\mathrm{lf}})dd^\dagger + U_1(\hat{X}_{\mathrm{hf}}, \hat{X}_{\mathrm{lf}})d^\dagger d + \frac{1}{2}\hbar\omega_{\mathrm{hf}}\hat{P}_{\mathrm{hf}}^2 + \frac{1}{2}\hbar\omega_{\mathrm{lf}}\hat{P}_{\mathrm{lf}}^2, \tag{4.1}$$

$$U_0(\hat{X}_{\mathrm{hf}}, \hat{X}_{\mathrm{lf}}) = \frac{1}{2}\hbar\omega_{\mathrm{hf}}\hat{X}_{\mathrm{hf}}^2 + \frac{1}{2}\hbar\omega_{\mathrm{lf}}\hat{X}_{\mathrm{lf}}^2, \tag{4.2}$$

$$U_1(\hat{X}_{\mathrm{hf}}, \hat{X}_{\mathrm{lf}}) = \varepsilon_0 + \sqrt{2}\lambda_{\mathrm{hf}}\hat{X}_{\mathrm{hf}} + \sqrt{2}\lambda_{\mathrm{lf}}\hat{X}_{\mathrm{lf}} + U_0(\hat{X}_{\mathrm{hf}}, \hat{X}_{\mathrm{lf}}). \tag{4.3}$$

We use the values from the previous chapter as a guide for the various parameters, since we already have experience using the semi-classical approximation with these. First of all, we keep the same parameters for the electronic dynamics, namely $\varepsilon_1 = 150\,\mathrm{meV}$ and $\Gamma^{\mathrm{L/R}} \in \{5\,\mathrm{meV}, 10\,\mathrm{meV}\}$. For the low natural frequency, we choose $\hbar\omega_{\mathrm{lf}} = 30\,\mathrm{meV}$, and $\lambda_{\mathrm{lf}} = 10\,\mathrm{meV}$ as the electronic-vibrational coupling. These values are taken from the intermediate regime in the last chapter, in which the semi-classical approximation is accurate. Furthermore, this allows us to make a direct comparison between the transport characteristics of the 1L2M model and the Holstein model. For the high natural frequency, we choose a value ten times larger, $\hbar\omega_{\mathrm{hf}} = 300\,\mathrm{meV}$. We know

from the previous chapter that we cannot treat such a high frequency semi-classically. Instead, we will keep it in the quantum part of the system. Since $\hbar\omega_{\mathrm{hf}} \gg \hbar\omega_{\mathrm{lf}}$ and also $\hbar\omega_{\mathrm{hf}} > \Gamma^{\mathrm{L}} + \Gamma^{\mathrm{R}}$, we expect that this does not break the time-scale separation between the quantum part and the low-frequency mode, and thus, the Langevin equation for the low-frequency mode is still valid.

In the next section, we apply the partial Wigner transform to this model system to obtain the Langevin equation of motion for the low-frequency vibration. To solve for the steady state of the remaining quantum part of the system, we will use the Lang-Firsov transformation from Sec. 3.2 again. With this, we will then study the electron transport through the 1L2M system and the effect of the high-frequency vibration on the stability of the junction. Herein, we will differentiate between two regimes:

(1) First, we consider the *strong-coupling* regime of the high-frequency mode, with $\lambda_{\mathrm{hf}} > \hbar\omega_{\mathrm{hf}}$.

(2) Second, we examine the *weak-coupling* regime of the high-frequency mode, with $\lambda_{\mathrm{hf}} < \hbar\omega_{\mathrm{hf}}$.

From the Holstein model, we know that weak coupling generally corresponds to a higher average vibrational excitation of the respective mode. Hence, we expect the strongly coupled second mode to rather stabilize the 1L2M junction, whereas the weakly coupled second vibration should enhance the instability.

4.2 Semi-classical description

For the semi-classical treatment of the 1L2M model, we start from the purely quantum system Hamiltonian, H_S, defined in Eq. (4.1). By applying the partial Wigner transform to the low-frequency vibration, following Sec. 2.4.2, we find the transformed system Hamiltonian, H_S^w, according to Eq. (2.49),

$$H_\mathrm{S}^\mathrm{w}(X_\mathrm{lf}, P_\mathrm{lf}) = U_0(\hat{X}_\mathrm{hf}, X_\mathrm{lf})dd^\dagger + U_1(\hat{X}_\mathrm{hf}, X_\mathrm{lf})d^\dagger d + \frac{1}{2}\hbar\omega_\mathrm{hf}\hat{P}_\mathrm{hf}^2 + \frac{1}{2}\hbar\omega_\mathrm{lf}P_\mathrm{lf}^2.$$

The variables X_lf and P_lf are the classical coordinates corresponding to the operators $\hat{X}_\mathrm{lf}$ and $\hat{P}_\mathrm{lf}$ of the low-frequency mode. The time evolution of these classical coordinates follows the dimensionless Langevin equations from Eq. (2.61), and the dynamics of the Wigner-transformed electronic density matrix, $\rho_\mathrm{S}^\mathrm{w}(X_\mathrm{lf}, P_\mathrm{lf}, t)$, follow from the quantum-classical BMME in Eq. (2.50).

To find the steady state of $\rho_\mathrm{S}^\mathrm{w}(X_\mathrm{lf}, P_\mathrm{lf}, t)$ for a fixed position X_lf, and $P_\mathrm{lf} = 0$, we have to solve the BMME of $H_\mathrm{S}^\mathrm{w}(X_\mathrm{lf}, P_\mathrm{lf} = 0)$. This is essentially a single electronic level coupled to one vibrational mode, the Holstein model. We know that this can be accomplished using the Lang-Firsov transformation introduced in Sec. 3.2. We start by replacing the displacement and momentum operators, $\hat{X}_\mathrm{hf}$ and $\hat{P}_\mathrm{hf}$, by their corresponding creation and annihilation operators, $a_\mathrm{hf}^\dagger$ and a_hf, according to Eq. (2.3). Using transformed operators, $\tilde{d}^{(\dagger)}$ and $\tilde{a}_\mathrm{hf}^{(\dagger)}$, defined as in Eqs. (3.4) to (3.6), we find the diagonal form of H_S^w,

$$H_\mathrm{S}^\mathrm{w}(X_\mathrm{lf}, P_\mathrm{lf} = 0) = \underbrace{\left(\varepsilon_0 - \frac{\lambda_\mathrm{hf}^2}{\hbar\omega_\mathrm{hf}} + \sqrt{2}\lambda_\mathrm{lf}X_\mathrm{lf}\right)}_{=\tilde{U}_1(X_\mathrm{lf})-\tilde{U}_0(X_\mathrm{lf})}\tilde{d}^\dagger\tilde{d} + \hbar\omega_\mathrm{hf}\tilde{a}_\mathrm{hf}^\dagger\tilde{a}_\mathrm{hf} + \frac{1}{2}\hbar\omega_\mathrm{lf}X_\mathrm{lf}^2, \tag{4.4}$$

where we also found the difference of the transformed potential energy surfaces, $\tilde{U}_1(X_\mathrm{lf}) - \tilde{U}_0(X_\mathrm{lf})$, which we will shall need later to explain some of the resulting physics. With this diagonalization, we can now solve for the steady state of $\rho_\mathrm{S}^\mathrm{w}(X_\mathrm{lf}, P_\mathrm{lf}, t)$ by truncating the vibrational operators, $\tilde{a}_\mathrm{hf}^{(\dagger)}$, at some number of basis states, $N_\mathrm{vib,hf}$, similar to Sec. 3.2. This then allows us to calculate the current-induced forces for the low-frequency vibration according to Eqs. (2.55) to (2.57), as well as the instantaneous electric current, $\langle I\rangle(X_\mathrm{lf})$, and the instantaneous excitation of the high-frequency mode, $\langle N_\mathrm{hf}\rangle(X_\mathrm{lf})$, following Eqs. (2.65) and (2.66).

Before we begin with the calculations, there is one further aspect to consider. As in Chapter 3, we want to compare different parameter sets in the following. For better comparability, the electronic level should always be set to the same energy value. Since we now have two vibrations in the completely quantum Hamiltonian, the renormalized energy also contains two Lang-Firsov corrections, which means $\varepsilon_1 = \varepsilon_0 - \lambda_\mathrm{hf}^2/\hbar\omega_\mathrm{hf} - \lambda_\mathrm{lf}^2/\hbar\omega_\mathrm{lf}$. Therefore, we always set ε_0 for the electronic part in Eq. (4.4) such that the renormalized energy is $\varepsilon_1 = 150\,\mathrm{meV}$. This also leaves us with

$$\tilde{U}_1(X_\mathrm{lf}) - \tilde{U}_0(X_\mathrm{lf}) = \varepsilon_1 + \frac{\lambda_\mathrm{lf}^2}{\hbar\omega_\mathrm{lf}} + \sqrt{2}\lambda_\mathrm{lf}X_\mathrm{lf}.$$

Now, we have all the tools to commence our study of the 1L2M model. In the next section, we will start by calculating and discussing the resulting current-induced forces.

4.3 Current-induced forces

In this section, we will examine the current-induced forces in the 1L2M model in detail. For this purpose, we consider two example systems, one with strong electronic-vibrational coupling of the high-frequency mode, $\lambda_{\mathrm{hf}} = 400\,\mathrm{meV}$, and one with weak coupling, $\lambda_{\mathrm{hf}} = 150\,\mathrm{meV}$. The further parameters are as previously given. For these examples, we calculate the current-induced forces as well as the instantaneous current and excitation of the high-frequency vibration, as explained in the section before.

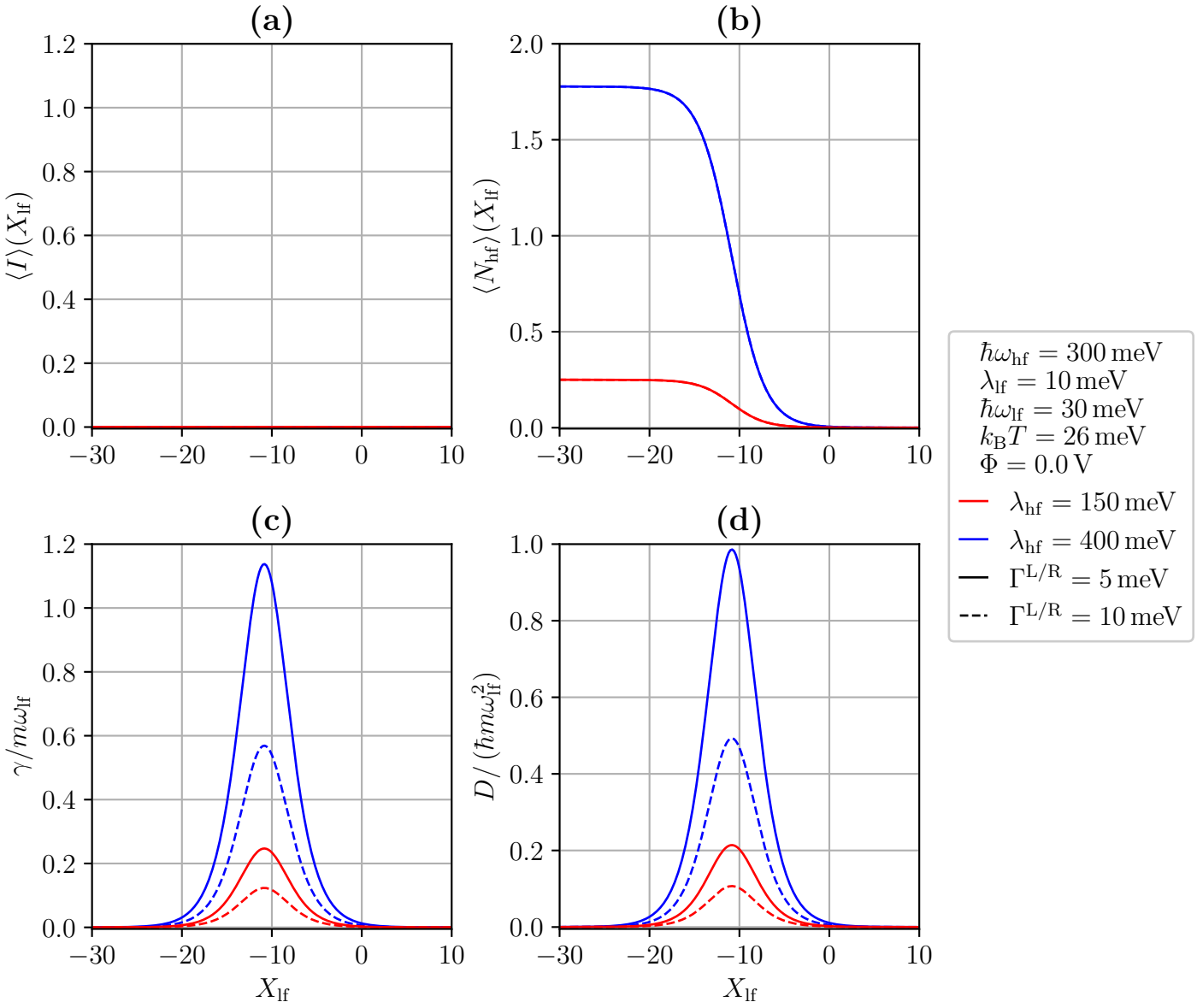

Figure 4.1: Instantaneous current, $\langle I\rangle(X_{\mathrm{lf}})$, instantaneous vibrational excitation, $\langle N_{\mathrm{hf}}\rangle(X_{\mathrm{lf}})$, and current-induced forces for a 1L2M model at zero bias voltage. Parameters not given in the legend: $\varepsilon_1 = 150\,\mathrm{meV}$, $N_{\mathrm{vib,hf}}$ according to Tab. 4.1.

The results for zero bias voltage are depicted in Fig. 4.1. The instantaneous current, $\langle I\rangle(X_{\mathrm{lf}})$, is zero for all X, as it should be. The electronic friction and the diffusion are qualitatively similar to Sec. 3.3, featuring a single peak centered at the resonance $\mu_{\mathrm{L/R}} = 0 = \tilde{U}_1(X_{\mathrm{lf}}) - \tilde{U}_0(X_{\mathrm{lf}})$. As explained in Sec. 3.3, at this resonance, electron-

hole pair creation in the electrodes is possible, leading to a dissipation of energy from the system to the electrodes that manifests itself in a frictional force. As illustrated in Fig. 4.4**(a)**, this resonance lies at $X_{\mathrm{lf}} \approx -10.8$ here. We further find that the fluctuation-dissipation theorem, $D = k_{\mathrm{B}}T \cdot \gamma$, is satisfied. By comparing the curves for the two λ_{hf}, we also find that both friction and diffusion scale with λ_{hf}. For $\lambda_{\mathrm{hf}} = 150\,\mathrm{meV}$, the magnitude is comparable with the Holstein system of the same parameters; see Fig. 3.12. With strong coupling, $\lambda_{\mathrm{hf}} = 400\,\mathrm{meV}$, however, the magnitude greatly increases. The reason for this is that the electron-hole pair creation in the electrodes at $\mu_{\mathrm{L/R}} = \tilde{U}_1 - \tilde{U}_0$ can now be accompanied by the excitation and de-excitation of multiple quanta of vibration in the high-frequency mode. This enables new channels for electron-hole pair creation leading to an increase in friction. However, for weak coupling, these excitation and de-excitation processes are strongly suppressed because the Franck-Condon matrix is close to diagonal; see Fig. 3.4. Hence, the increase in friction is only minimal for weak coupling, but very significant for strong coupling of the high-frequency vibration [20, 27].

A new feature of the 1L2M model is the instantaneous excitation of the high-frequency mode, $\langle N_{\mathrm{hf}}\rangle(X_{\mathrm{lf}})$. At zero bias voltage, we find that for $X_{\mathrm{lf}} > -10.8$, the instantaneous excitation is zero, whereas for $X_{\mathrm{lf}} < -10.8$, it approaches $\langle N_{\mathrm{hf}}\rangle(X_{\mathrm{lf}}) \to (\lambda_{\mathrm{hf}}/\hbar\omega_{\mathrm{hf}})^2$. To understand this, we need to take a look at the different contributions to the vibrational excitation in the Lang-Firsov transformed system. From Eqs. (3.5) and (3.6), we find

$$\langle N_{\mathrm{hf}}\rangle = \langle a_{\mathrm{hf}}^\dagger a_{\mathrm{hf}}\rangle = \langle \tilde{a}_{\mathrm{hf}}^\dagger \tilde{a}_{\mathrm{hf}}\rangle - \frac{\lambda_{\mathrm{hf}}}{\hbar\omega_{\mathrm{hf}}}\left(\langle \tilde{a}_{\mathrm{hf}}^\dagger \tilde{d}^\dagger \tilde{d}\rangle + \langle \tilde{a}_{\mathrm{hf}} \tilde{d}^\dagger \tilde{d}\rangle\right) + \left(\frac{\lambda_{\mathrm{hf}}}{\hbar\omega_{\mathrm{hf}}}\right)^2 \langle \tilde{d}^\dagger \tilde{d}\rangle.$$

At $\Phi = 0$, the junction essentially resides in its ground state because $|\tilde{U}_1 - \tilde{U}_0| \gg k_{\mathrm{B}}T$ for most X_{lf}, and $\hbar\omega_{\mathrm{hf}} \gg k_{\mathrm{B}}T$. As depicted in Fig. 4.4**(a)**, for $X_{\mathrm{lf}} > -10.8$, we find $\tilde{U}_1 > \tilde{U}_0$, which leads to $\langle \tilde{d}^\dagger \tilde{d}\rangle \to 0$; whereas for $X_{\mathrm{lf}} < -10.8$, we have $\tilde{U}_0 > \tilde{U}_1$, leading to $\langle \tilde{d}^\dagger \tilde{d}\rangle \to 1$. Furthermore, we have $\langle \tilde{a}_{\mathrm{hf}}^\dagger \tilde{a}_{\mathrm{hf}}\rangle \approx 0$ for all X_{lf} because $\hbar\omega_{\mathrm{hf}} \gg k_{\mathrm{B}}T$; and consequently also $\langle \tilde{a}_{\mathrm{hf}}^{(\dagger)} \tilde{d}^\dagger \tilde{d}\rangle \approx 0$. This leaves only a single non-zero contribution, giving $\langle N_{\mathrm{hf}}\rangle(X_{\mathrm{lf}}) \to (\lambda_{\mathrm{hf}}/\hbar\omega_{\mathrm{hf}})^2$ for $X_{\mathrm{lf}} < -10.8$, and $\langle N_{\mathrm{hf}}\rangle(X_{\mathrm{lf}}) \to 0$ for $X_{\mathrm{lf}} > -10.8$.

Next, we consider a finite bias voltage, $\Phi = 1.5\,\mathrm{V}$, as depicted in Fig. 4.2. The quantities experience a much richer structure now. The current exhibits typical features of the Franck-Condon blockade. Unlike the Holstein model, however, we do not find a single flat plateau, but the current exhibits a series of steps in a symmetrical pattern. The instantaneous excitation of the high-frequency mode also exhibits a step pattern, which exceeds the values $(\lambda_{\mathrm{hf}}/\hbar\omega_{\mathrm{hf}})^2$, now that $\mathrm{e}\Phi > \hbar\omega_{\mathrm{hf}}$. We also find that the maximum excitation for any X_{lf} is higher for the weakly coupled vibration, as shown in the quantum studies of the Holstein model. The electronic friction also shows a rich structure. The single peak from before has split into six separate peaks in a symmetrical and equidistant order. Surprisingly, we find negative friction peaks with the weakly coupled high-frequency mode. Lastly, also the diffusion coefficient exhibits a step pattern instead of the flat plateau shape we found for the Holstein model. Unlike the electric current, the steps are not all positive going from the outside to the inside, but we also find the diffusion decreasing in certain areas. This is much more enhanced with the weakly coupled high-frequency mode, where we find a significant dip in the diffusion around its symmetry axis.

To understand the emergence of the additional steps and peaks, we must consider the various electron-hole pair creation processes that are possible. As discussed in

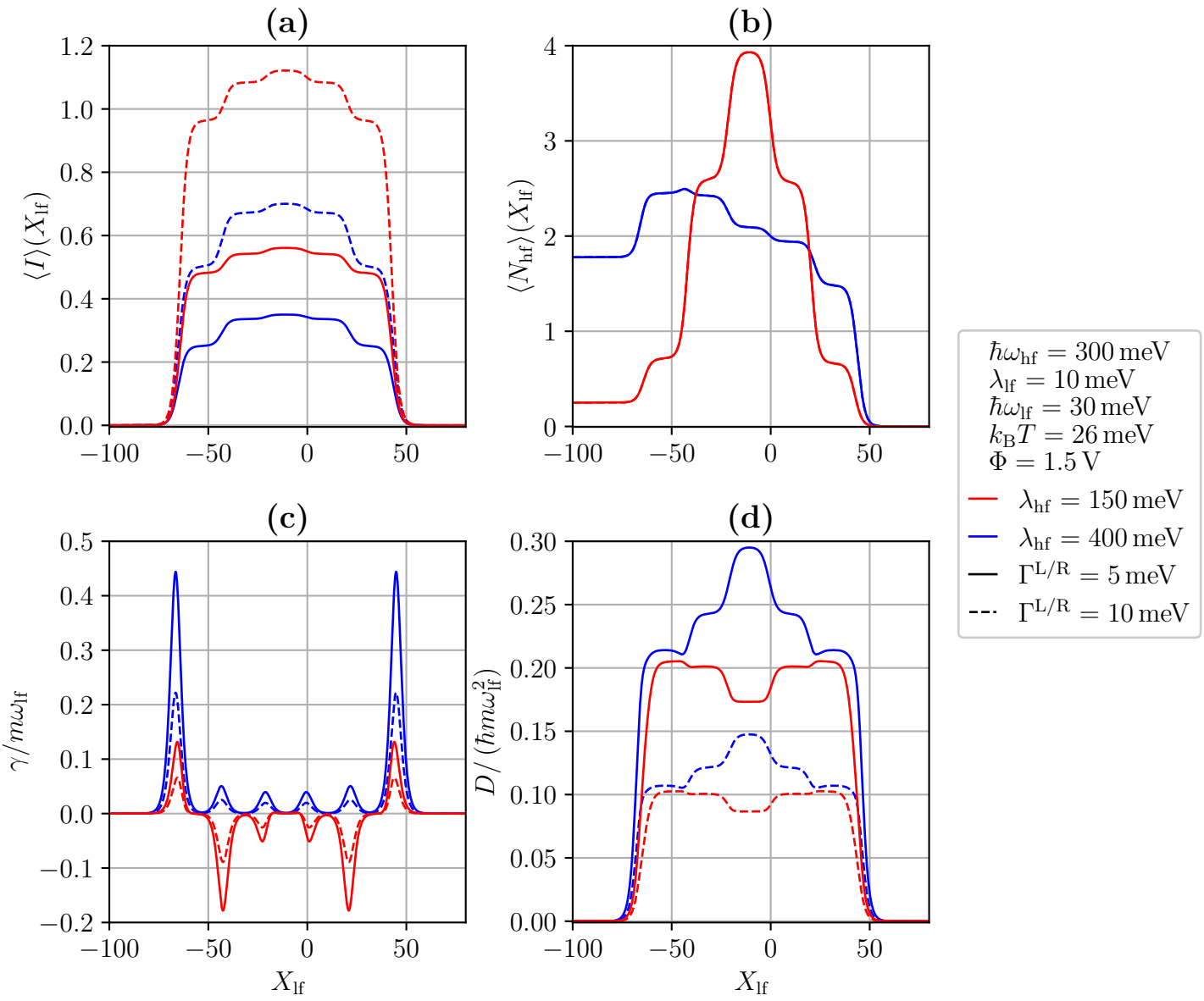

Figure 4.2: Instantaneous current, $\langle I \rangle(X_{\mathrm{lf}})$, instantaneous vibrational excitation, $\langle N_{\mathrm{hf}} \rangle(X_{\mathrm{lf}})$, and current-induced forces for a 1L2M model at non-zero bias voltage. Parameters not given in the legend: $\varepsilon_1 = 150\,\mathrm{meV}$, $N_{\mathrm{vib,hf}}$ according to Tab. 4.1.

Sec. 3.3, at finite bias voltage, there can be vibrationally induced electron-hole pair creation. For the 1L2M model in semi-classical treatment, this means that electron-hole pair creation may be accompanied by the relaxation of multiple quanta of the high-frequency vibration, $v \cdot \hbar\omega_{\mathrm{hf}}$, as depicted in Fig. 4.3. Consequently, for sufficient bias voltage, electron-hole pair creation may not only occur around the resonance $\mu_{\mathrm{L/R}} = \tilde{U}_1 - \tilde{U}_0$, but also for the additional resonances $\mu_{\mathrm{L}} = \tilde{U}_1 - \tilde{U}_0 + v \cdot \hbar\omega_{\mathrm{hf}}$ and $\mu_{\mathrm{R}} = \tilde{U}_1 - \tilde{U}_0 - v \cdot \hbar\omega$, with $v \in \mathbb{N}$. From the illustration in Fig. 4.4**(b)**, we find that these resonances lie at $X_{\mathrm{lf}} \in \{42.2, 21.0, -0.2, -21.4, -42.7, -63.9\}$, which match exactly the positions of the peaks and steps in Fig. 4.2. Explaining the different magnitude and direction of the steps and peaks is difficult, though. Comparing the behavior of current and diffusion, it seems that while every newly emerging channel of charge transport through the junction gives a positive contribution to the current, the contribution to

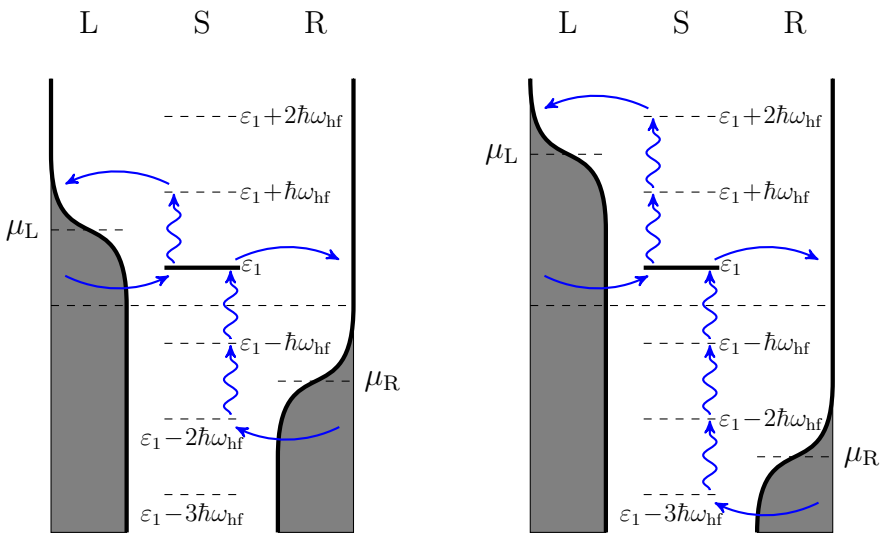

(a) $\Phi > 2\varepsilon_1/\mathrm{e}$. **(b)** $\Phi > 2(\varepsilon_1 + \hbar\omega_{\mathrm{hf}})/\mathrm{e}$.

Figure 4.3: Energy level scheme for the 1L2M model in semi-classical treatment. As illustrated in **(a)** and **(b)**, the 1L2M model exhibits vibrationally induced electron-hole pair creation. In this process, a single or multiple vibrational quanta are de-excited and the released energy serves to create an electron-hole pair in one of the electrodes.

the diffusion is negative for some. Furthermore, the vibrational excitation of the high-frequency mode with weak coupling increases strongly at the resonances for $v \in \{1, 2\}$, although the corresponding transitions are strongly suppressed in the Franck-Condon matrix. Analogously, one would expect for the weak-coupling system that the electronic friction peaks become significantly smaller towards the center due to Franck-Condon suppression. Instead, the second outermost peaks are the largest and, surprisingly, the friction even becomes negative there, turning the usually dissipative electron-hole pair creation in the electrodes into an energy harvesting process. This can and will, as we will see in the next section, strongly enhance the instability of the low-frequency vibrational mode.

Here we conclude our discussion of the current-induced forces of the 1L2M model, albeit some phenomena have remained unexplained for now. In the next section, we will look at the semi-classical dynamics that follow from these current-induced forces.

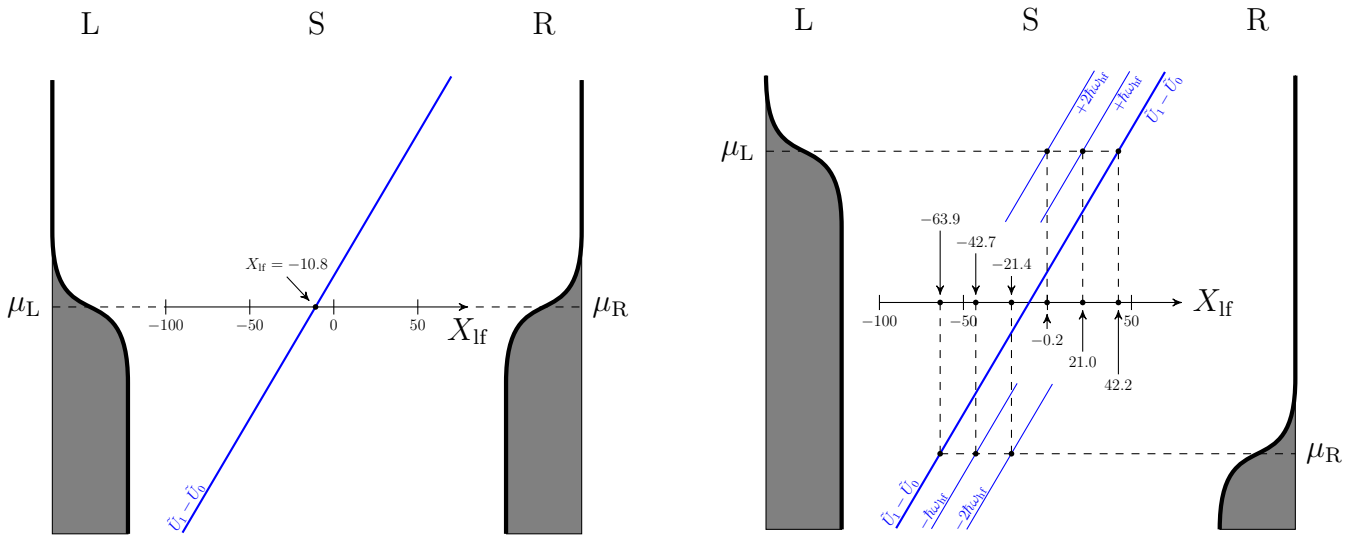

(a) $\Phi = 0.0\,\mathrm{V}$.

(b) $\Phi = 1.5\,\mathrm{V}$.

Figure 4.4: Illustration of the energy difference, $\tilde{U}_1 - \tilde{U}_0$, between the transformed charged and neutral state of the 1L2M model in semi-classical treatment. At zero bias voltage, depicted in **(a)**, the resonances of the chemical potentials with the energy difference, $\mu_{\mathrm{L/R}} = \tilde{U}_1 - \tilde{U}_0$, coincide at $X \approx -10.8$. At a bias voltage of $\Phi = 1.5\,\mathrm{V}$, illustrated in **(b)**, the resonances are split, and additional resonances emerge due to vibrationally induced electron-hole pair creation (see Fig. 4.3). We find the resonances with μ_{L} at approximately $X \in \{42.2, 21.0, -0.2\}$, and the resonances with μ_{R} at approximately $X \in \{-21.4, -42.7, -63.9\}$.

4.4 Semi-classical results

In this section, we study transport characteristics of the 1L2M model by analyzing expectation values of its most important observables, the electric current and the excitation of the two vibrational modes. Our focus will be on the stability of the junction, which is mainly characterized by the average excitation of the vibrations reached for a certain bias voltage. Herein, we also want to compare the 1L2M model with the corresponding Holstein model of the same parameters, to determine whether the addition of the second vibrational mode leads to an increase or decrease in the overall stability of the junction.

As mentioned at the beginning of this chapter, we will investigate two different regimes characterized by the electron-vibrational coupling of the high-frequency mode. For the strong-coupling regime, we look at $\lambda_{\mathrm{hf}} \in \{300\,\mathrm{meV}, 400\,\mathrm{meV}, 500\,\mathrm{meV}, 600\,\mathrm{meV}\}$, giving us good coverage of the range $\lambda_{\mathrm{hf}}/\hbar\omega_{\mathrm{hf}} = 1...2$. To calculate the current-induced forces, we need to truncate the vibrational basis of the high-frequency mode. For $\lambda_{\mathrm{hf}} = 300\,\mathrm{meV}$, the current-induced forces are converged for a bias voltage of up to $\Phi = 2\,\mathrm{V}$ by using $N_{\mathrm{vib,hf}} = 20$. For $\lambda_{\mathrm{hf}} \geq 400\,\mathrm{meV}$, $N_{\mathrm{vib,hf}} = 15$ is sufficient to reach the same convergence. In the weak-coupling regime, a larger number of basis states is required to obtain a converged result at high bias voltages because we get a much higher vibrational excitation, as we have already found in Sec. 3.2. Therefore, we limit our analysis to two values for the coupling, namely $\lambda_{\mathrm{hf}} \in \{150\,\mathrm{meV}, 200\,\mathrm{meV}\}$. For $\Phi \leq 1.5\,\mathrm{V}$, we find converged results with $N_{\mathrm{vib,hf}} = 20$; for $\Phi > 1.5\,\mathrm{V}$, we need $N_{\mathrm{vib,hf}} = 25$, which makes the computation more expensive.

	Grid spacing	Vibrational basis	Equilibration time	
	ΔX	$N_{\mathrm{vib,hf}}$	$\Gamma^{\mathrm{L/R}} = 5\,\mathrm{meV}$	$\Gamma^{\mathrm{L/R}} = 10\,\mathrm{meV}$
$\lambda_{\mathrm{hf}} = 150\,\mathrm{meV}$	0.2	20, 25 ($\Phi > 1.5\,\mathrm{V}$)	$4\,000\,\omega_{\mathrm{lf}}t$	$10\,000\,\omega_{\mathrm{lf}}t$
$\lambda_{\mathrm{hf}} = 200\,\mathrm{meV}$	0.2	20, 25 ($\Phi > 1.5\,\mathrm{V}$)	$10\,000\,\omega_{\mathrm{lf}}t$	$20\,000\,\omega_{\mathrm{lf}}t$
$\lambda_{\mathrm{hf}} = 300\,\mathrm{meV}$	0.2	20	$2\,000\,\omega_{\mathrm{lf}}t$	$2\,000\,\omega_{\mathrm{lf}}t$
$\lambda_{\mathrm{hf}} = 400\,\mathrm{meV}$	0.2	15	$2\,000\,\omega_{\mathrm{lf}}t$	$2\,000\,\omega_{\mathrm{lf}}t$
$\lambda_{\mathrm{hf}} = 500\,\mathrm{meV}$	0.2	15	$2\,000\,\omega_{\mathrm{lf}}t$	$2\,000\,\omega_{\mathrm{lf}}t$
$\lambda_{\mathrm{hf}} = 600\,\mathrm{meV}$	0.2	15	$2\,000\,\omega_{\mathrm{lf}}t$	$2\,000\,\omega_{\mathrm{lf}}t$

Table 4.1: Grid spacings and equilibration times chosen for the calculation of the semi-classical steady state of a 1L2M model with $\varepsilon_1 = 150\,\mathrm{meV}$, $\hbar\omega_{\mathrm{hf}} = 300\,\mathrm{meV}$, $\hbar\omega_{\mathrm{lf}} = 30\,\mathrm{meV}$, $\lambda_{\mathrm{lf}} = 10\,\mathrm{meV}$, and $k_{\mathrm{B}}T = 26\,\mathrm{meV}$.

In the next step, we calculate the expectation values $\langle I\rangle^{\mathrm{ss}}$, $\langle N_{\mathrm{hf}}\rangle^{\mathrm{ss}}$, and $\langle N_{\mathrm{lf}}\rangle^{\mathrm{ss}}$ following the procedure elaborated in Secs. 2.4.4 and 2.4.5, where $\langle N_{\mathrm{lf}}\rangle^{\mathrm{ss}}$ follows from Eq. (2.67). The grid spacings and equilibration times chosen for the different λ_{hf} and $\Gamma^{\mathrm{L/R}}$ are indicated in Tab. 4.1. It should be mentioned that, for the weak-coupling cases, we are able to determine the semi-classical steady state only for $\Phi \leq 1.15\,\mathrm{V}$ with $\lambda_{\mathrm{hf}} = 150\,\mathrm{meV}$, and for $\Phi \leq 1.8\,\mathrm{V}$ with $\lambda_{\mathrm{hf}} = 200\,\mathrm{meV}$, respectively. At higher bias voltages, the semi-classical trajectories exceed our pre-calculated grid, which spans $X_{\mathrm{lf}} = -720...700$ (cf. Fig. 4.2), before a steady state is reached. This indicates that at these high voltages, the low-frequency mode is highly unstable, quickly absorbing huge amounts of energy. We will discuss this in more detail in the following Sec. 4.4.2.

In the following, we analyze the resulting steady-state expectation values and compare them with the corresponding Holstein model of the same parameters.

4.4.1 Strong-coupling regime

The semi-classical steady-state expectation values of electric current, $\langle I \rangle^{\mathrm{ss}}$, and vibrational excitation, $\langle N_{\mathrm{hf}} \rangle^{\mathrm{ss}}$ and $\langle N_{\mathrm{lf}} \rangle^{\mathrm{ss}}$, for strong coupling, $\lambda_{\mathrm{hf}} \geq \hbar\omega_{\mathrm{hf}}$, are depicted in Fig. 4.5. Alongside, we also included $\langle I \rangle^{\mathrm{ss}}$ and $\langle N_{\mathrm{lf}} \rangle^{\mathrm{ss}}$ for the corresponding Holstein model without high-frequency mode, taken from Fig. 3.13.

It can be seen that the current and the excitation of the high-frequency vibration show a typical step pattern, which arises from the step features in the corresponding instantaneous quantities, $\langle I \rangle(X_{\mathrm{lf}})$ and $\langle N_{\mathrm{hf}} \rangle(X_{\mathrm{lf}})$, respectively. The steps are centered at 0.3 V, 0.9 V, and 1.5 V, respectively, corresponding to the surpassing of $\mu_{\mathrm{L}} = \varepsilon_1 + v \cdot \hbar\omega_{\mathrm{hf}}$ for $v \in \{0, 1, 2\}$, as illustrated in Fig. 4.6. We also find the typical Franck-Condon blockade in $\langle I \rangle^{\mathrm{ss}}$ and $\langle N_{\mathrm{hf}} \rangle^{\mathrm{ss}}$ for the different values of λ_{hf}, where a greater λ_{hf} leads to an increased vibrational excitation, $\langle N_{\mathrm{hf}} \rangle^{\mathrm{ss}}$, but a smaller current at a given bias voltage, due to the suppression of on-diagonal transitions $v \to v$ in the associated Franck-Condon matrix. For the current, the curve of the Holstein model can be seen as a kind of limit of the Franck-Condon blockade for $\lambda_{\mathrm{hf}} \to 0$.

The excitation of the low-frequency mode follows the exponential curve of the Holstein model for $\Phi < 0.6\,\mathrm{V}$, with no noticeable difference between the different λ_{hf}. For greater voltages, though, $\langle N_{\mathrm{lf}} \rangle^{\mathrm{ss}}$ exhibits a periodic pattern, whose period is 0.6 V in line with the distance of the steps in $\langle I \rangle^{\mathrm{ss}}$ and $\langle N_{\mathrm{hf}} \rangle^{\mathrm{ss}}$. The Holstein model, on the other hand, continues its exponential increase in vibrational excitation, indicating great instability of the Holstein junction at higher voltages. Therefore, we conclude that the introduction of the additional strongly coupled high-frequency mode contributes to the stabilization of the 1L2M junction at high bias voltage. Up to $\Phi = 2\,\mathrm{V}$, only a maximum excitation of $\langle N_{\mathrm{lf}} \rangle^{\mathrm{ss}} \approx 40$ is reached, whereas the Holstein system already exceeds $\langle N_{\mathrm{lf}} \rangle^{\mathrm{ss}} = 100$ below 1 V (see Fig. 3.13).

The mechanism underlying the stabilization effect can be understood by comparing the two vibrational excitations, $\langle N_{\mathrm{hf}} \rangle^{\mathrm{ss}}$ and $\langle N_{\mathrm{lf}} \rangle^{\mathrm{ss}}$. It can be seen that $\langle N_{\mathrm{lf}} \rangle^{\mathrm{ss}}$ exhibits local maxima at voltages in the middle between two adjacent steps in $\langle N_{\mathrm{hf}} \rangle^{\mathrm{ss}}$, and local minima right at the center of a step. From this behavior, we deduce the following. At the steps in $\langle I \rangle^{\mathrm{ss}}$ and $\langle N_{\mathrm{hf}} \rangle^{\mathrm{ss}}$, the surpassing of $\mu_{\mathrm{L}} = \varepsilon_1 + v \cdot \hbar\omega_{\mathrm{hf}}$ leads to the emergence of a new channel for the charge transport through the junction, as illustrated in Fig. 4.6. The transport of electrons by this channel is accompanied by excitation of the high-frequency mode, which consumes large amounts of energy as $\hbar\omega_{\mathrm{hf}} = 300\,\mathrm{meV}$. This energy is lost for the excitation of the low-frequency mode leading to a significant decrease of $\langle N_{\mathrm{lf}} \rangle^{\mathrm{ss}}$ with increasing voltage. We call this observation *negative differential excitation*, $\frac{\mathrm{d}}{\mathrm{d}\Phi} \langle N_{\mathrm{lf}} \rangle^{\mathrm{ss}} < 0$. The reason why the energy dissipated in the junction is distributed so unevenly between the two vibrations is the large difference in the electronic-vibrational couplings, $\lambda_{\mathrm{hf}} \gg \lambda_{\mathrm{lf}}$, which strongly favors excitation of the high-frequency mode. Only when a new channel reaches saturation, precisely in the middle of two steps, is more energy available again for excitation of the low-frequency vibration, leading to its periodic pattern. The effect is further enhanced by larger λ_{hf}, which is why we find the lowest $\langle N_{\mathrm{lf}} \rangle^{\mathrm{ss}}$ for $\lambda_{\mathrm{hf}} = 600\,\mathrm{meV}$.

The finding of this stabilization mechanism is the main physical result of this thesis. However, by which current-induced force this mechanism is mediated is still unknown to us. Up to now, we have not been able to identify any periodic conspicuity in the corresponding current-induced forces.

Lastly, we note that the different electrode couplings, $\Gamma^{\mathrm{L/R}}$, considered in **(a)** to **(c)** and **(d)** to **(f)**, respectively, do not show an influence on the stabilization mechanism.

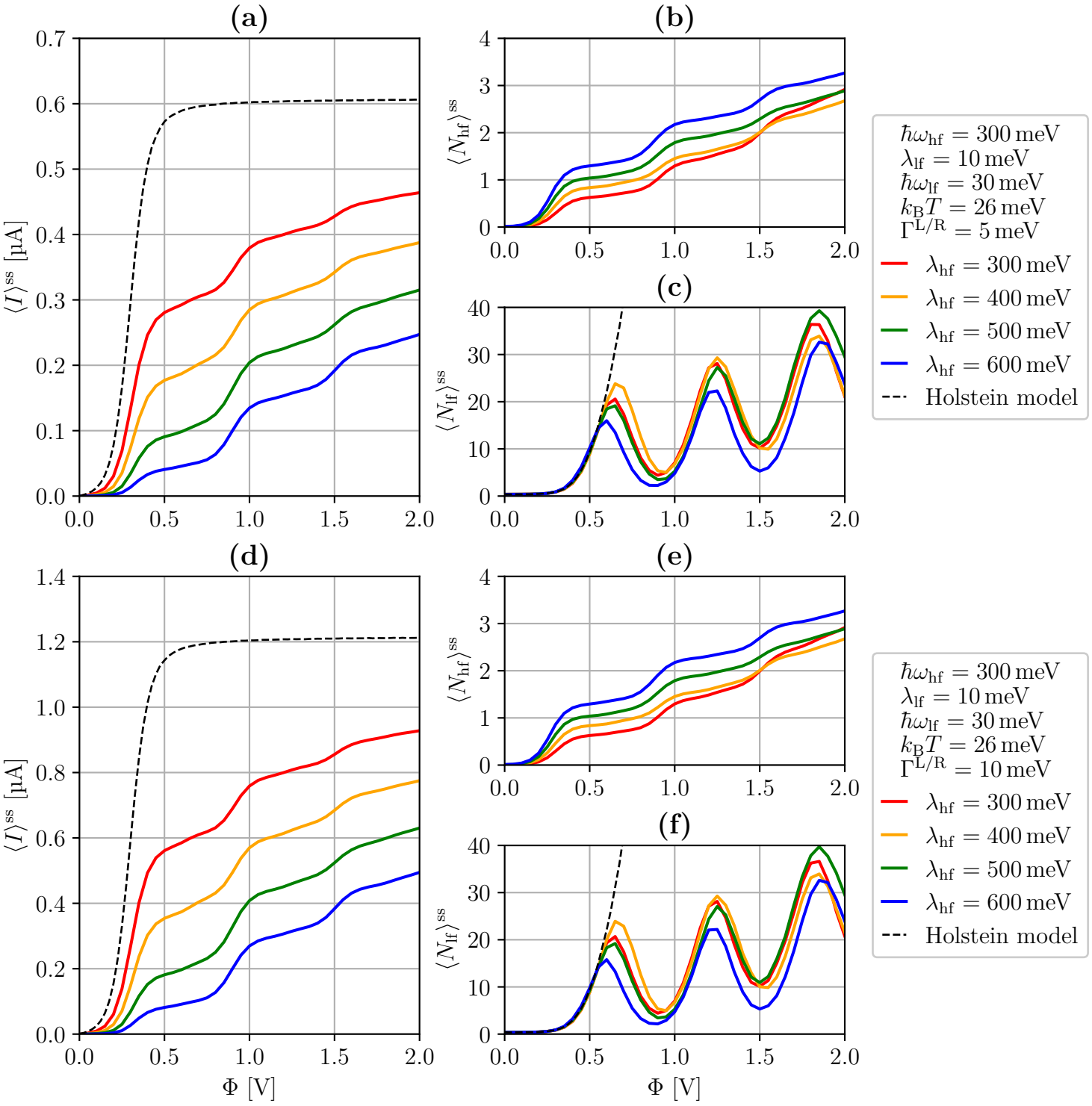

Figure 4.5: Current-voltage characteristics and average vibrational excitations of a 1L2M model in the strong-coupling regime. Parameters not given in the legend: $\varepsilon_1 = 150\,\mathrm{meV}$. The curve for the Holstein model is taken from Fig. 3.13 for $\lambda = 10\,\mathrm{meV}$.

The vibrational excitations, $\langle N_{\mathrm{hf}} \rangle^{\mathrm{ss}}$ and $\langle N_{\mathrm{lf}} \rangle^{\mathrm{ss}}$, are nearly identical in both cases. The current is proportional to $\Gamma^{\mathrm{L/R}}$, as we have found previously in Secs. 2.3, 3.2 and 3.4.

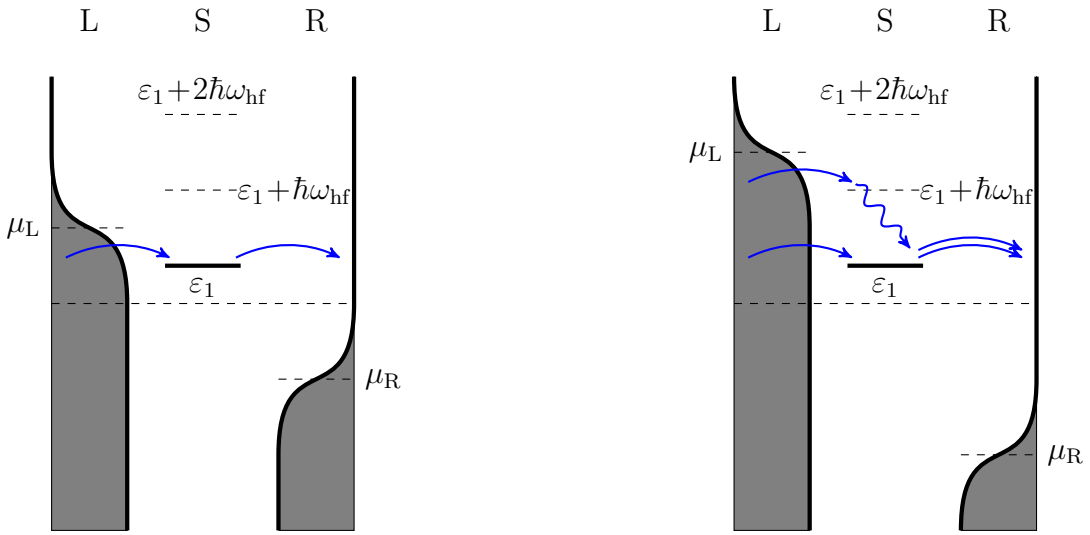

(a) $\Phi > 2\varepsilon_1/\mathrm{e}$.

(b) $\Phi > 2(\varepsilon_1 + \hbar\omega_{\mathrm{hf}})/\mathrm{e}$.

Figure 4.6: Energy level scheme for the 1L2M model in semi-classical treatment. When the bias voltage is large enough that the chemical potential of the left electrode is above the energy ε_1, as depicted in **(a)**, the first transport channel becomes available, which does not involve excitation or de-excitation of vibrational quanta. When the bias voltage is even larger such that the chemical potential of the left electrode surpasses $\varepsilon_1 + \hbar\omega_{\mathrm{hf}}$, a second transport channel becomes available, as illustrated in **(b)**, where electron transport is accompanied by the excitation of one vibrational quantum of the high-frequency mode.

4.4.2 Weak-coupling regime

For the weak-coupling regime, $\lambda_{\mathrm{hf}} < \hbar\omega_{\mathrm{hf}}$, the semi-classical steady-state expectation values of electric current, $\langle I\rangle^{\mathrm{ss}}$, and vibrational excitation, $\langle N_{\mathrm{hf}}\rangle^{\mathrm{ss}}$ and $\langle N_{\mathrm{lf}}\rangle^{\mathrm{ss}}$, are shown in Fig. 4.7. In addition, we again included $\langle I\rangle^{\mathrm{ss}}$ and $\langle N_{\mathrm{lf}}\rangle^{\mathrm{ss}}$ for the corresponding Holstein model without the high-frequency mode, taken from Fig. 3.13.

It can be seen that the electric current increases with a steep step centered at $\Phi = 0.3\,\mathrm{V}$, analogous to the strong-coupling cases considered in the previous section. This step corresponds again to the crossing of $\mu_{\mathrm{L}} = \varepsilon_1$, and is also visible in $\langle N_{\mathrm{hf}}\rangle^{\mathrm{ss}}$. For $\Phi < 0.75\,\mathrm{V}$, we further find the continuation of the Franck-Condon blockade from the last section, with the currents for the much smaller λ_{hf} now increasingly approaching the limit curve of the Holstein model, which effectively represents the limit for $\lambda_{\mathrm{hf}} \to 0$. Likewise, we find a higher $\langle N_{\mathrm{hf}}\rangle^{\mathrm{ss}}$ for larger λ_{hf} as expected, but only up to a bias voltage of $\Phi = 0.6\,\mathrm{V}$. At $\Phi = 0.9\,\mathrm{V}$, a second step corresponding to the crossing of $\mu_{\mathrm{L}} = \varepsilon_1 + \hbar\omega_{\mathrm{hf}}$ is noticeable in $\langle N_{\mathrm{hf}}\rangle^{\mathrm{ss}}$ for $\lambda_{\mathrm{hf}} = 200\,\mathrm{meV}$, but in $\langle N_{\mathrm{hf}}\rangle^{\mathrm{ss}}$ for $\lambda_{\mathrm{hf}} = 150\,\mathrm{meV}$ and in the currents, this second step can not be found. Instead of the expected increase, the current for $\lambda_{\mathrm{hf}} = 200\,\mathrm{meV}$ stays constant around $\Phi = 0.9\,\mathrm{V}$, whereas for $\lambda_{\mathrm{hf}} = 150\,\mathrm{meV}$, both $\langle I\rangle^{\mathrm{ss}}$ and $\langle N_{\mathrm{hf}}\rangle^{\mathrm{ss}}$ decrease with increasing voltage, which is usually called *negative differential resistance*, $\frac{\mathrm{d}}{\mathrm{d}\Phi}\langle I\rangle^{\mathrm{ss}} < 0$.

The excitation of the low-frequency mode follows the curve of the Holstein model for $\Phi < 0.6\,\mathrm{V}$, with no difference between the two values of λ_{hf} noticeable. For higher bias voltage, the curves exhibit greatly different behavior, though. For $\lambda_{\mathrm{hf}} = 200\,\mathrm{meV}$,

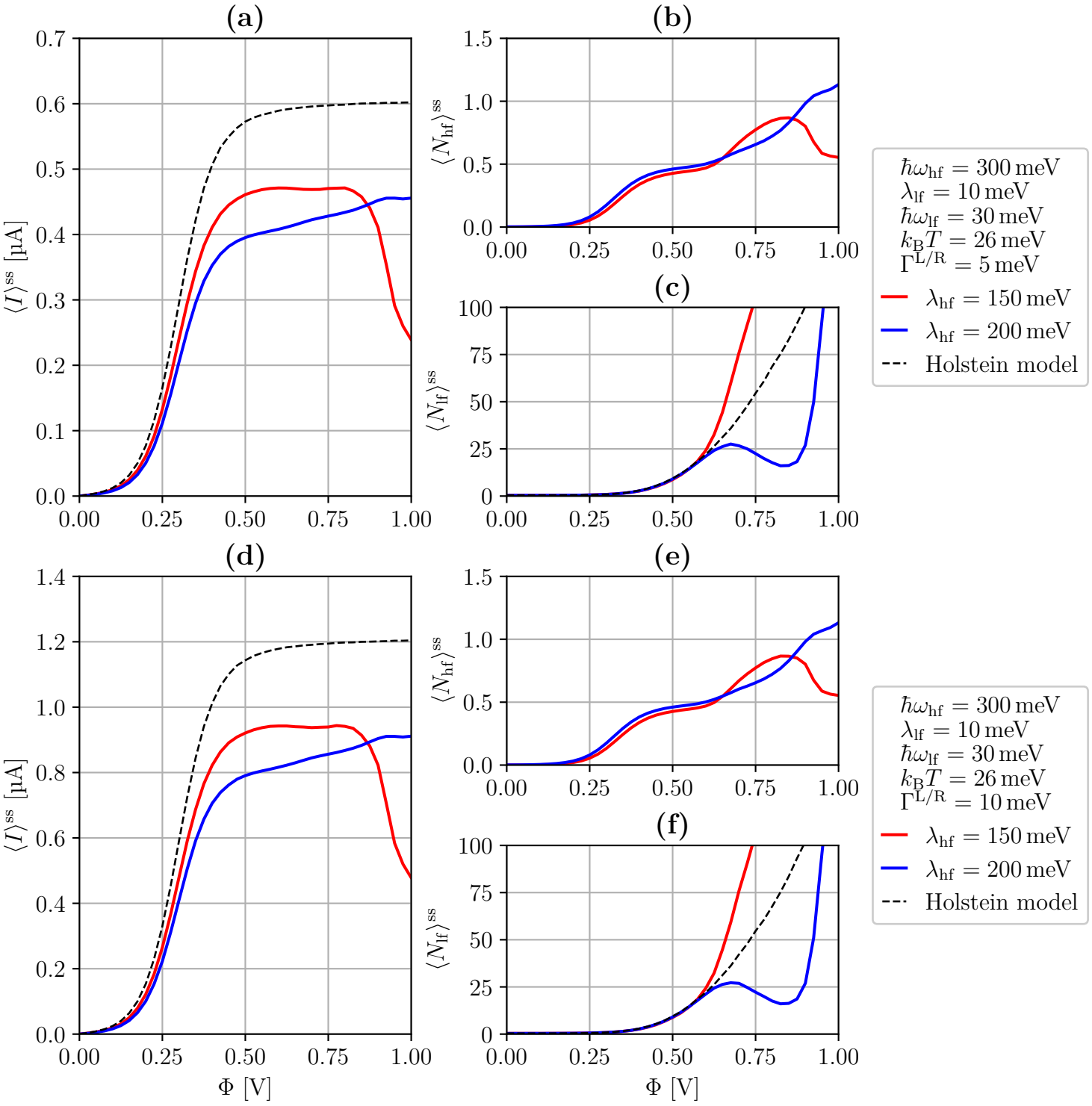

Figure 4.7: Current-voltage characteristics and average vibrational excitations of a 1L2M model in the weak-coupling regime. Parameters not given in the legend: $\varepsilon_1 = 150\,\mathrm{meV}$. The curve for the Holstein model is taken from Fig. 3.13 for $\lambda = 10\,\mathrm{meV}$.

$\langle N_{\mathrm{lf}} \rangle^{\mathrm{ss}}$ deviates downward compared to the Holstein model and exhibits a similar wave pattern as we found for the strong coupling in the previous section. The local maximum within the wave shape is approximately in the middle of the steps of $\langle N_{\mathrm{hf}} \rangle^{\mathrm{ss}}$ at 0.3 V

and 0.9 V, respectively, and the local minimum is about at the position of the step at 0.9 V. The curve for $\lambda_{\mathrm{hf}} = 150\,\mathrm{meV}$, in contrast, shows a very steep and sudden increase, deviating upward compared to the Holstein model. We, therefore, conclude that the additional high-frequency mode with $\lambda_{\mathrm{hf}} = 150\,\mathrm{meV}$ makes the low-frequency mode of the 1L2M model even more unstable than that of the Holstein model, resulting in the 1L2M system exceeding an excitation of $\langle N_{\mathrm{lf}}\rangle^{\mathrm{ss}} = 100$ already at $\Phi = 0.75\,\mathrm{V}$, which happens only at $\Phi = 0.9\,\mathrm{V}$ for the Holstein system. The additional mode with $\lambda_{\mathrm{hf}} = 200\,\mathrm{meV}$, on the other hand, stabilizes the low-frequency vibration of the 1L2M system. However, a sudden and steep increase of $\langle N_{\mathrm{lf}}\rangle^{\mathrm{ss}}$ is also seen there for $\Phi > 0.9\,\mathrm{V}$, and an excitation of $\langle N_{\mathrm{lf}}\rangle^{\mathrm{ss}} = 100$ is ultimately reached at $\Phi = 0.95\,\mathrm{V}$. So, relevant stabilization is only found in a small voltage range.

The destabilization at very weak coupling, $\lambda_{\mathrm{hf}} = 150\,\mathrm{meV}$, is to be understood as opposed to the stabilization effect for strong coupling seen in the previous section. Whereas $\langle N_{\mathrm{lf}}\rangle^{\mathrm{ss}}$ shows a very steep increase for $\Phi > 0.6\,\mathrm{V}$ with $\lambda_{\mathrm{hf}} = 150\,\mathrm{meV}$, the excitation of the high-frequency mode remains minor. Due to the weak coupling, the high-frequency mode absorbs very little of the energy dissipated in the junction. The dissipated energy is instead put into rapid excitation of the low-frequency vibration, indicating a destabilization of the junction. This rapid increase in $\langle N_{\mathrm{lf}}\rangle^{\mathrm{ss}}$ occurs right around the voltage where the present charge transport channel reaches saturation. That is, where the local maxima of $\langle N_{\mathrm{lf}}\rangle^{\mathrm{ss}}$ are located in the previous section, and in fact, also for $\lambda_{\mathrm{hf}} = 200\,\mathrm{meV}$ here. For slightly stronger coupling, $\lambda_{\mathrm{hf}} = 200\,\mathrm{meV}$, we first do find a stabilizing effect as in the last section. For bias voltages above $\Phi > 0.9\,\mathrm{V}$, however, the effect is not sufficient, and the junction shows instability as well.

To explain the negative differential resistance, $\frac{\mathrm{d}}{\mathrm{d}\Phi}\langle I\rangle^{\mathrm{ss}} < 0$, for $\Phi > 0.8\,\mathrm{V}$, we must consider Fig. 4.2 again. For very high excitation, $\langle N_{\mathrm{lf}}\rangle^{\mathrm{ss}} > 100$, the low-frequency mode spends an increasing amount of time at $|X_{\mathrm{lf}}| > 100$. At such large displacement, however, the instantaneous electric current, $\langle I\rangle(X_{\mathrm{lf}})$, is zero, as can be seen in Fig. 4.2. This is because for large displacement, $|X_{\mathrm{lf}}| > 100$, the energy difference between the charged and neutral state, $|\tilde{U}_1 - \tilde{U}_0|$, is much larger than $\mathrm{e}\Phi$; hence, the system stays in either the charged or neutral state, depending on whether $X_{\mathrm{lf}} < 0$ or $X_{\mathrm{lf}} > 0$, preventing charge transport through the junction. This leads to the negative differential resistance, which is visible for $\lambda_{\mathrm{hf}} = 150\,\mathrm{meV}$ at $\Phi > 0.8\,\mathrm{V}$. The excitation of the high-frequency mode, $\langle N_{\mathrm{hf}}\rangle^{\mathrm{ss}}$, exhibits a similar decrease because $\langle N_{\mathrm{hf}}\rangle(X_{\mathrm{lf}})$ is also smaller at $|X_{\mathrm{lf}}| > 100$ than at $|X_{\mathrm{lf}}| < 100$. It is highly questionable, though, whether the observed negative differential resistance and decrease in $\langle N_{\mathrm{hf}}\rangle^{\mathrm{ss}}$ make physical sense. In reality, the junction would probably not withstand $\langle N_{\mathrm{lf}}\rangle^{\mathrm{ss}} > 100$, but disintegrate beforehand. Furthermore, the harmonic vibrational modes considered here may not be valid models for any real molecular vibrations at such high excitation.

Finally, we also find from Fig. 4.7 that the different electrode couplings, $\Gamma^{\mathrm{L/R}}$, considered in **(a)** to **(c)** and **(d)** to **(f)**, respectively, do not show an influence on the (de-)stabilization. The vibrational excitations are nearly identical in both cases, and the current is proportional to $\Gamma^{\mathrm{L/R}}$ as previously.

Lastly, we consider the convergence problems mentioned in Sec. 4.4. For this, Fig. 4.8 depicts the mean kinetic energy, $\langle E_{\mathrm{kin}}\rangle(t)$, of a group of 100 Langevin trajectories for the system with $\lambda_{\mathrm{hf}} = 150\,\mathrm{meV}$ at the bias voltages $\Phi \in \{1.15\,\mathrm{V}, 1.20\,\mathrm{V}\}$. As mentioned in Sec. 3.4, we have utilized the time-evolution of $\langle E_{\mathrm{kin}}\rangle(t)$ of such a group of trajectories to determine the equilibration times for all our semi-classical calculations. Fig. 4.8**(a)** shows that, for $\Phi = 1.15\,\mathrm{V}$, $\langle E_{\mathrm{kin}}\rangle(t)$ equilibrates within about $2000\,\omega_{\mathrm{lf}}t$, and

(a) $\Phi = 1.15\,\mathrm{V}$.

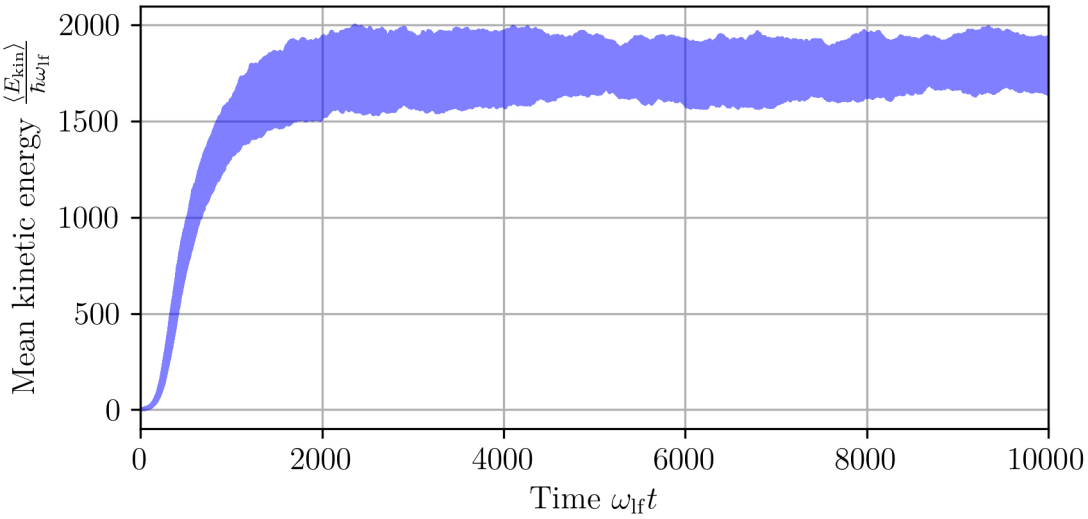

(b) $\Phi = 1.20\,\mathrm{V}$.

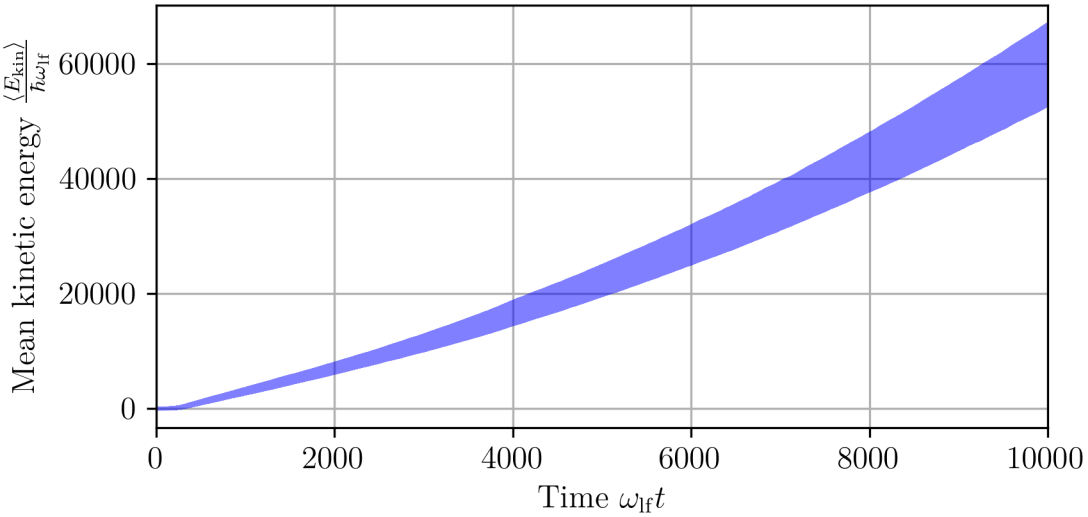

Figure 4.8: Time evolution of the mean kinetic energy of a group of 100 Langevin trajectories for a 1L2M model with $\varepsilon_1 = 150\,\mathrm{meV}$, $\hbar\omega_{\mathrm{hf}} = 300\,\mathrm{meV}$, $\lambda_{\mathrm{hf}} = 150\,\mathrm{meV}$, $\hbar\omega_{\mathrm{lf}} = 30\,\mathrm{meV}$, $\lambda_{\mathrm{lf}} = 10\,\mathrm{meV}$, and $k_{\mathrm{B}}T = 26\,\mathrm{meV}$. By comparing **(a)** and **(b)**, it can be seen that increasing the bias voltage from $\Phi = 1.15\,\mathrm{V}$ to $\Phi = 1.20\,\mathrm{V}$ leads to a huge increase in the mean kinetic energy and a loss of its convergence.

then stays between $1500\,\hbar\omega_{\mathrm{lf}} < \langle E_{\mathrm{kin}}\rangle(t) < 2000\,\hbar\omega_{\mathrm{lf}}$, indicating that the steady state is reached. Analogous behavior is found at any bias voltage, $\Phi \leq 1.15\,\mathrm{V}$. At $\Phi = 1.20\,\mathrm{V}$, on the other hand, $\langle E_{\mathrm{kin}}\rangle(t)$ shows a presumably exponential increase throughout the time period considered, as depicted in Fig. 4.8**(b)**. After $\omega_{\mathrm{lf}}t = 10\,000$, a huge mean kinetic energy of $60\,000\,\hbar\omega_{\mathrm{lf}}$ is reached. For greater $\omega_{\mathrm{lf}}t$, the displacement, X_{lf}, of many trajectories exceeds our pre-calculated grid of the current-induced forces, which spans $X_{\mathrm{lf}} = -720...700$. This is a strong indication that at $\Phi \geq 1.20\,\mathrm{V}$, there may not exist a steady state. Instead, the energy of the low-frequency vibration continues growing forever, presumably because the overall effect of the negative friction outweighs the effect of the ordinary positive friction. We find the same convergence problem for both

$\Gamma^{\mathrm{L/R}} \in \{5\,\mathrm{meV}, 10\,\mathrm{meV}\}$. Furthermore, the system with $\lambda_{\mathrm{hf}} = 200\,\mathrm{meV}$, also shows this convergence problem, but only starting from $\Phi \geq 1.80\,\mathrm{V}$. This is why we have limited Fig. 4.7 to a voltage range of $\Phi = 0...1\,\mathrm{V}$. This lack of convergence is another clear sign of vibrational instability of the considered 1L2M model with a weakly coupled high-frequency mode.

4.5 Conclusions

In this chapter, we have studied the one-level two-mode junction, consisting of one electronic level coupled to one high-frequency and one low-frequency vibrational mode, and compared it to the corresponding Holstein model without the high-frequency mode.

In the strong-coupling regime of the high-frequency mode, $\lambda_{\mathrm{hf}} > \hbar\omega_{\mathrm{hf}}$, we found that the addition of the high-frequency mode has a stabilizing effect on the low-frequency vibration. Up to $\Phi = 2\,\mathrm{V}$, only a maximum excitation of $\langle N_{\mathrm{lf}} \rangle^{\mathrm{ss}} \approx 40$ is reached in our considerations, whereas the Holstein model exceeds $\langle N_{\mathrm{lf}} \rangle^{\mathrm{ss}} = 100$ below 1 V. This stabilization works on the basis that $\lambda_{\mathrm{hf}} \gg \lambda_{\mathrm{lf}}$, which leads to a very uneven distribution of the energy dissipated in the junction, strongly favoring excitation of the high-frequency mode. Thereby, only little dissipated energy is left for the low-frequency mode, leading to significantly reduced excitation. With increasing voltage, the stabilization becomes periodically weaker and stronger, leading to *negative differential excitation* of the low-frequency mode.

In the weak-coupling regime, $\lambda_{\mathrm{hf}} < \hbar\omega_{\mathrm{hf}}$, we found that the additional high-frequency vibration shows stabilizing or destabilizing effect on the low-frequency mode depending on the exact electronic-vibrational coupling, λ_{hf}. It remains to be investigated where the boundary between the two opposite effects is situated for different λ_{hf} or $\Gamma^{\mathrm{L/R}}$. However, the observed stabilization is of relevant magnitude only in a small voltage range. We further observed negative differential resistance for very weak coupling, $\lambda_{\mathrm{hf}} = 150\,\mathrm{meV}$, at high bias voltage, where the low-frequency vibration shows instability. Though, we believe that this feature of the 1L2M model does not relate to real physical behavior, as it only occurs in the region of severe vibrational instability.

Chapter 5

Summary and Outlook

In this thesis, we have studied the transport of electrons through molecular junctions with both weak and strong electronic-vibrational coupling. To this end, we utilized the Born-Markov master equation as a tool to describe the molecular junction and the electrodes quantum-mechanically; and also the semi-classical theory of electronic friction to describe a low-frequency vibrational mode in the junction [38].

In Chapter 2, we defined our model of a molecular junction between a left and right electrode. Using the Born-Markov approximation and the additional secular approximation [31], we derived a general master equation for the model in Sec. 2.2. While this approximate master equation is limited to weak coupling between the junction and the electrodes, $\Gamma^{\mathrm{L/R}} < k_{\mathrm{B}} T_{\mathrm{L/R}}$, it does not pose any restrictions on the dynamics inside the junction, which allowed us to study both weak and strong coupling between the electronic levels and vibrational modes of the junction. In Sec. 2.4, we performed a partial Wigner transform of the reduced density operator of the molecular system to obtain a semi-classical description [37]. We further exploited the time-scale separation that is typically found between the fast electron transport dynamics and the low-frequency vibrations of the nuclei in the molecule to derive an approximate semi-classical Langevin equation for the low-frequency vibrational degrees of freedom [30, 39]. The central quantities of the Langevin equation are the current-induced forces: the mean force, a white-noise stochastic force, and the electronic friction, which gives the theory its name. The mean force is essentially equivalent to a semi-classical adiabatic approximation, and the friction and the stochastic force can be understood as the first-order correction to it. Utilizing the advanced m-BAOAB algorithm to integrate the Langevin equation [52], we elaborated a procedure to find the steady state of the junction in the semi-classical picture, allowing us to calculate steady-state transport characteristics like the average electric current, $\langle I \rangle^{\mathrm{ss}}$, and the average excitation of vibrational modes, $\langle N \rangle^{\mathrm{ss}}$.

In Chapter 3, we demonstrated the application of the semi-classical approach by considering the prominent Holstein model [20, 41, 48], which comprises a junction of one electronic level coupled to a harmonic vibrational mode. To determine for which parameter regimes of the Holstein model our semi-classical method is well suited, we considered different regimes, and compared the semi-classical treatment with a fully quantum BMME calculation. The typical time scale of the vibrational mode is given by its natural frequency, $\hbar\omega$. The time scale on which the electron transport occurs is defined by the coupling of the junction to the electrodes, $\Gamma^{\mathrm{L}} + \Gamma^{\mathrm{R}}$. The relation between these time scales gives rise to three distinct regimes. In the classical regime,

where $\hbar\omega \ll \Gamma^{\mathrm{L}} + \Gamma^{\mathrm{R}}$, the semi-classical approach was found to be accurate, and for strong electronic-vibrational coupling, $\lambda > \hbar\omega$, the semi-classical method is also clearly preferable in terms of computational effort. Surprisingly, the semi-classical calculation also delivered very accurate results in the intermediate regime, where $\hbar\omega \sim \Gamma^{\mathrm{L}} + \Gamma^{\mathrm{R}}$, as long as the electronic-vibrational coupling is weak to intermediate, $\lambda \lesssim \hbar\omega$. For stronger coupling, the time-scale separation appears to break down and the semi-classical calculation is no longer accurate at all voltages. The semi-classical method is generally less computationally expensive in this regime, though. Thus, particularly for $\lambda < \hbar\omega$, this regime is the optimal domain of application for the semi-classical approach. We also considered the quantum regime, with $\hbar\omega \gg \Gamma^{\mathrm{L}} + \Gamma^{\mathrm{R}}$. Here, the time-scale separation is clearly violated, and the semi-classical method breaks down.

A major goal in this thesis was to investigate the one-level two-mode model (1L2M model) [27], which is an extension of the Holstein model that adds a second high-frequency vibrational mode. This was accomplished in Chapter 4. In line with our findings in Chapter 3, we studied a 1L2M junction with a low-frequency mode in the intermediate regime, $\hbar\omega_{\mathrm{lf}} \sim \Gamma^{\mathrm{L}} + \Gamma^{\mathrm{R}}$, with weak electronic-vibrational coupling $\lambda_{\mathrm{lf}} < \hbar\omega_{\mathrm{lf}}$, where it can be accurately treated by the semi-classical method. The high-frequency vibration is treated quantum-mechanically alongside the electronic dynamics. For this 1L2M system, we considered two interesting regimes: the strong-coupling regime, where $\lambda_{\mathrm{hf}} > \hbar\omega_{\mathrm{hf}}$, and the weak-coupling regime, with $\lambda_{\mathrm{hf}} < \hbar\omega_{\mathrm{hf}}$. Our focus herein was to compare the vibrational stability of the low-frequency mode in semi-classical treatment with the Holstein model without a second mode. In the strong-coupling regime, we found that the addition of the high-frequency vibration exerts a strongly stabilizing effect on the low-frequency mode. This stabilization works on the basis that $\lambda_{\mathrm{hf}} \gg \lambda_{\mathrm{lf}}$, which leads to a very uneven distribution of the energy dissipated in the junction, strongly favoring excitation of the high-frequency mode. With increasing voltage, the stabilization becomes periodically weaker and stronger as new channels of electron transport through the junction become accessible. This periodicity gives rise to negative differential excitation, $\frac{\mathrm{d}}{\mathrm{d}\Phi}\langle N_{\mathrm{lf}}\rangle^{\mathrm{ss}} < 0$, of the low-frequency mode. The finding of this stabilization mechanism is the main physical result of this thesis. In the weak-coupling regime, we found that the additional high-frequency mode exerts a stabilizing or destabilizing effect on the low-frequency vibration depending on the electronic-vibrational coupling, λ_{hf}. The observed stabilization is much weaker than in the strong-coupling regime, though, and only relevant in a small voltage range.

With this summary, we close our study of vibrational instabilities in molecular junctions caused by current-induced forces. It remains for future work to further investigate the observed stabilization effect in the 1L2M model for various other parameter regimes and to seek to identify similar mechanisms in more complicated systems. Furthermore, the question, through which of the current-induced forces the found stabilization is mediated, is open to be resolved.

Appendix A

Bath correlation functions

In this section, we calculate the Fourier-transformed correlation functions defined in Eqs. (2.25) to (2.28). We start by evaluating the correlation function $G^<_{ij}(\tau) = G^{\dagger -}_{ij}(\tau)$, as defined by Eq. (2.16),

$$\begin{aligned} G^<_{ij}(\tau) &= \mathrm{tr_B}\left\{\rho^0_\mathrm{B} B^\dagger_i(t) B_j(t-\tau)\right\} \\ &= \sum_{K,K'} \sum_{k_K, k_{K'}} V_{i,k_K} V^*_{j,k_{K'}} \,\mathrm{tr_B}\left\{\rho^0_\mathrm{B} c^\dagger_{k_K}(t) c_{k_{K'}}(t-\tau)\right\}. \end{aligned}$$

By virtue of Eq. (2.11), we find

$$\mathrm{tr_B}\left\{\rho^0_\mathrm{B} c^\dagger_{k_K}(t) c_{k_{K'}}(t-\tau)\right\} = \mathrm{tr_B}\left\{\rho^0_\mathrm{B} c^\dagger_{k_K}(t) c_{k_K}(t-\tau)\right\} \cdot \delta_{K,K'} \cdot \delta_{k_K,k_{K'}},$$

thereby reducing the correlation function above to just two sums over K and k, respectively. At this point, we insert the interaction picture time evolution of the annihilation and creation operators and simplify further, remembering that $[H_K, N_K] = 0$,

$$G^<_{ij}(\tau) = \sum_K \sum_{k_K} V_{i,k_K} V^*_{j,k_K} \frac{1}{Z_K} \,\mathrm{tr}_K \left\{ e^{(H_K - \mu_K N_K)/k_\mathrm{B} T_K} c^\dagger_{k_K} e^{-\mathrm{i} H_K \tau/\hbar} c_{k_K} e^{\mathrm{i} H_K \tau/\hbar} \right\}.$$

With $e^{-\mathrm{i}H_K\tau/\hbar} c_{k_K} e^{\mathrm{i}H_K\tau/\hbar} = e^{\pm \mathrm{i}\varepsilon_{k_K}\tau/\hbar} c_{k_K}$, we are left with

$$G^<_{ij}(\tau) = \sum_K \sum_{k_K} V_{i,k_K} V^*_{j,k_K} e^{\mathrm{i}\varepsilon_{k_K}\tau/\hbar} \frac{1}{Z_K} \,\mathrm{tr}_K \left\{ e^{(H_K - \mu_K N_K)/k_\mathrm{B} T_K} c^\dagger_{k_K} c_{k_K} \right\},$$

which evaluates to

$$G^<_{ij}(\tau) = \sum_K \sum_{k_K} V_{i,k_K} V^*_{j,k_K} e^{\mathrm{i}\varepsilon_{k_K}\tau/\hbar} f^K(\varepsilon_{k_K}), \tag{A.1}$$

where f^K is the well-known Fermi function,

$$f^K(\varepsilon) := \frac{1}{e^{(\varepsilon - \mu_K)/k_\mathrm{B} T_K} + 1}. \tag{A.2}$$

Analogously, the second correlation function, $G^>_{ji}(\tau) = G^{-\dagger}_{ji}(\tau)$, evaluates to

$$G^>_{ji}(\tau) = \sum_K \sum_{k_K} V_{i,k_K} V^*_{j,k_K} e^{-\mathrm{i}\varepsilon_{k_K}\tau/\hbar} \left(1 - f^K(\varepsilon_{k_K})\right). \tag{A.3}$$

Inserting Eqs. (A.1) and (A.3) into the Fourier transforms from Eqs. (2.25) to (2.28), we get

$$
\begin{aligned}
S_{ij}^{<}(\omega) &= \sum_K \sum_{k_K} V_{i,k_K} V_{j,k_K}^* f^K(\varepsilon_{k_K}) \int_0^\infty \frac{\mathrm{d}\tau}{\hbar} \sin\Big((\varepsilon_{k_K} - \hbar\omega)\tau/\hbar\Big), \\
S_{ij}^{>}(\omega) &= \sum_K \sum_{k_K} V_{i,k_K} V_{j,k_K}^* \Big(f^K(\varepsilon_{k_K}) - 1\Big) \int_0^\infty \frac{\mathrm{d}\tau}{\hbar} \sin\Big((\varepsilon_{k_K} - \hbar\omega)\tau/\hbar\Big), \\
\gamma_{ij}^{<}(\omega) &= \sum_K \sum_{k_K} V_{i,k_K} V_{j,k_K}^* f^K(\varepsilon_{k_K}) \int_{-\infty}^\infty \frac{\mathrm{d}\tau}{\hbar} e^{\mathrm{i}(\varepsilon_{k_K} - \hbar\omega)\tau/\hbar}, \\
\gamma_{ij}^{>}(\omega) &= \sum_K \sum_{k_K} V_{i,k_K} V_{j,k_K}^* \Big(1 - f^K(\varepsilon_{k_K})\Big) \int_{-\infty}^\infty \frac{\mathrm{d}\tau}{\hbar} e^{\mathrm{i}(\varepsilon_{k_K} - \hbar\omega)\tau/\hbar}.
\end{aligned}
$$

For $\gamma_{ij}^{<}$ and $\gamma_{ij}^{>}$, the above expressions are easy to evaluate because the integrals over $\mathrm{d}\tau$ on the right each give a Dirac δ-function,

$$
\int_{-\infty}^\infty \frac{\mathrm{d}\tau}{\hbar} e^{\mathrm{i}(\varepsilon - \hbar\omega)\tau/\hbar} = 2\pi\, \delta(\varepsilon - \hbar\omega),
$$

leading to

$$
\begin{aligned}
\gamma_{ij}^{<}(\omega) &= 2\pi \sum_K \sum_{k_K} V_{i,k_K} V_{j,k_K}^* f^K(\varepsilon_{k_K}) \delta(\varepsilon_{k_K} - \hbar\omega), \\
\gamma_{ij}^{>}(\omega) &= 2\pi \sum_K \sum_{k_K} V_{i,k_K} V_{j,k_K}^* \Big(1 - f^K(\varepsilon_{k_K})\Big) \delta(\varepsilon_{k_K} - \hbar\omega).
\end{aligned}
$$

Using the identity $f(x)\delta(x-y) = f(y)\delta(x-y)$, we can rewrite these expressions to

$$
\begin{aligned}
\gamma_{ij}^{<}(\omega) &= 2\pi \sum_K \left(\sum_{k_K} V_{i,k_K} V_{j,k_K}^* \delta(\varepsilon_{k_K} - \hbar\omega) \right) f^K(\hbar\omega) \\
&= \sum_K \Gamma_{ij}^K(\omega) f^K(\hbar\omega), \\
\gamma_{ij}^{>}(\omega) &= 2\pi \sum_K \left(\sum_{k_K} V_{i,k_K} V_{j,k_K}^* \delta(\varepsilon_{k_K} - \hbar\omega) \right) \Big(1 - f^K(\hbar\omega)\Big) \\
&= \sum_K \Gamma_{ij}^K(\omega) \Big(1 - f^K(\hbar\omega)\Big),
\end{aligned}
$$

where we identified the electrode coupling functions, $\Gamma_{ij}^K(\omega)$, from Eq. (2.8). For $S_{ij}^{<}$ and $S_{ij}^{>}$, the calculation is more intricate. First, we must determine the semi-infinite integral over $\mathrm{d}\tau$, which is essentially the Fourier sine transform of the Heaviside step function. It can be written as

$$
\int_0^\infty \frac{\mathrm{d}\tau}{\hbar} \sin\Big((\varepsilon - \hbar\omega)\tau/\hbar\Big) = \mathrm{p.v.} \left(\frac{1}{\varepsilon - \hbar\omega} \right),
$$

where p.v. denotes the Cauchy principal value. With this, we get

$$
\begin{aligned}
S_{ij}^{<}(\omega) &= \sum_K \sum_{k_K} V_{i,k_K} V_{j,k_K}^* f^K(\varepsilon_{k_K}) \,\mathrm{p.v.} \left(\frac{1}{\varepsilon_{k_K} - \hbar\omega} \right), \\
S_{ij}^{>}(\omega) &= \sum_K \sum_{k_K} V_{i,k_K} V_{j,k_K}^* \Big(f^K(\varepsilon_{k_K}) - 1\Big) \,\mathrm{p.v.} \left(\frac{1}{\varepsilon_{k_K} - \hbar\omega} \right).
\end{aligned}
$$

To evaluate the Cauchy principal value, we rewrite these expressions in terms of an integral over a δ-function,

$$\begin{aligned}
S_{ij}^{<}(\omega) &= \sum_K \text{p.v.} \int_{-\infty}^{\infty} \mathrm{d}\varepsilon \sum_{k_K} V_{i,k_K} V_{j,k_K}^* \delta(\varepsilon - \varepsilon_{k_K}) \frac{f^K(\varepsilon)}{\varepsilon - \hbar\omega} \\
&= \frac{1}{2\pi} \sum_K \text{p.v.} \int_{-\infty}^{\infty} \mathrm{d}\varepsilon \, \Gamma_{ij}^K(\tfrac{\varepsilon}{\hbar}) \frac{f^K(\varepsilon)}{\varepsilon - \hbar\omega}, \\
S_{ij}^{>}(\omega) &= \sum_K \text{p.v.} \int_{-\infty}^{\infty} \mathrm{d}\varepsilon \sum_{k_K} V_{i,k_K} V_{j,k_K}^* \delta(\varepsilon - \varepsilon_{k_K}) \frac{f^K(\varepsilon) - 1}{\varepsilon - \hbar\omega} \\
&= \frac{1}{2\pi} \sum_K \text{p.v.} \int_{-\infty}^{\infty} \mathrm{d}\varepsilon \, \Gamma_{ij}^K(\tfrac{\varepsilon}{\hbar}) \frac{f^K(\varepsilon) - 1}{\varepsilon - \hbar\omega}.
\end{aligned}$$

For general $\Gamma_{ij}^K(\frac{\varepsilon}{\hbar})$, the resulting integrals cannot be solved analytically. In this thesis, however, we always work in the wideband limit, where we have a constant electrode coupling, $\Gamma_{ij}^K(\frac{\varepsilon}{\hbar}) = \Gamma_{ij}^K$. In this limit, $S_{ij}^{<}$ and $S_{ij}^{>}$ are

$$\begin{aligned}
S_{ij}^{<}(\omega) &= \sum_K \frac{\Gamma_{ij}^K}{2\pi} \text{p.v.} \int_{-\infty}^{\infty} \mathrm{d}\varepsilon \, \frac{f^K(\varepsilon)}{\varepsilon - \hbar\omega}, \\
S_{ij}^{>}(\omega) &= \sum_K \frac{\Gamma_{ij}^K}{2\pi} \text{p.v.} \int_{-\infty}^{\infty} \mathrm{d}\varepsilon \, \frac{f^K(\varepsilon) - 1}{\varepsilon - \hbar\omega},
\end{aligned}$$

and can be solved analytically. The detailed procedure can be found in Appendix B. We find the following result,

$$S_{ij}^{<}(\omega) = S_{ij}^{>}(\omega) = \sum_K \frac{\Gamma_{ij}^K}{2\pi} \operatorname{Re}\left\{ \psi_0 \left(\frac{1}{2} + \mathrm{i} \frac{\hbar\omega - \mu_K}{2\pi k_\mathrm{B} T_K} \right) \right\}.$$

Lastly, we use the wideband limit for $\gamma_{ij}^{\lessgtr}$ as well, and introduce a shorthand notation for the real part of the Digamma function,

$$\psi^K(\hbar\omega) = \frac{1}{2\pi} \operatorname{Re}\left\{ \psi_0 \left(\frac{1}{2} + \mathrm{i} \, \frac{\hbar\omega - \mu_K}{2\pi k_\mathrm{B} T_K} \right) \right\}. \tag{A.4}$$

With this, the Fourier-transformed correlation functions take the final form

$$\begin{aligned}
\gamma_{ij}^{<}(\omega) &= \sum_K \Gamma_{ij}^K \, f^K(\hbar\omega), \\
\gamma_{ij}^{>}(\omega) &= \sum_K \Gamma_{ij}^K \left(1 - f^K(\hbar\omega) \right), \\
S_{ij}^{<}(\omega) = S_{ij}^{>}(\omega) &= \sum_K \Gamma_{ij}^K \, \psi^K(\hbar\omega).
\end{aligned}$$

Appendix B

Lamb shift

In this appendix, we calculate the Fourier-transformed correlation functions $S_{ij}^{<}$ and $S_{ij}^{>}$ in the wideband limit,

$$S_{ij}^{<}(\omega) = \sum_K \frac{\Gamma_{ij}^K}{2\pi} \,\mathrm{p.v.} \int_{-\infty}^{\infty} \mathrm{d}\varepsilon \, \frac{f^K(\varepsilon)}{\varepsilon - \hbar\omega},$$
$$S_{ij}^{>}(\omega) = \sum_K \frac{\Gamma_{ij}^K}{2\pi} \,\mathrm{p.v.} \int_{-\infty}^{\infty} \mathrm{d}\varepsilon \, \frac{f^K(\varepsilon) - 1}{\varepsilon - \hbar\omega},$$

which contribute to the renormalization of the energy levels in the system via the Lamb shift Hamiltonian.

One can easily show that

$$\mathrm{p.v.} \int_{-\infty}^{\infty} \mathrm{d}\varepsilon \, \frac{1}{\varepsilon - \hbar\omega} = 0.$$

So only the integral with the Fermi function is left,

$$\mathrm{p.v.} \int_{-\infty}^{\infty} \mathrm{d}\varepsilon \, \frac{f^K(\varepsilon)}{\varepsilon - \hbar\omega}.$$

To calculate this integral, we close the integration contour by adding and subtracting the integral over a contour that encircles the upper half of the complex plane at $R \to \infty$,

$$\left(\mathrm{p.v.} \int_{-\infty}^{\infty} \mathrm{d}\varepsilon + \int_{\gamma} \mathrm{d}\varepsilon - \int_{\gamma} \mathrm{d}\varepsilon \right) \frac{f^K(\varepsilon)}{\varepsilon - \hbar\omega} = \left(\mathrm{p.v.} \oint \mathrm{d}\varepsilon - \int_{\gamma} \mathrm{d}\varepsilon \right) \frac{f^K(\varepsilon)}{\varepsilon - \hbar\omega}.$$

The closed contour integral can now be evaluated using the residue theorem, where we have to consider all poles of the integrand in the upper half of the complex plane. The Fermi function $f^K(\varepsilon)$ has simple poles at $\varepsilon_n = \mu_K + (2n+1)\pi \mathrm{i} k_\mathrm{B} T_K$, where those for $n \geq 0$ lie in the upper half of the complex plane. The $1/(\varepsilon - \hbar\omega)$ term has one simple pole at $\varepsilon = \hbar\omega$, which lies precisely on the contour. In the principal value integration,

we thus have to consider $\frac{1}{2}$ times its residue. In total, we find

$$\begin{aligned}\left(\text{p.v.}\oint \mathrm{d}\varepsilon - \int_\gamma \mathrm{d}\varepsilon\right)\frac{f^K(\varepsilon)}{\varepsilon-\hbar\omega} &= \pi\mathrm{i}\,\mathrm{Res}_{\varepsilon=\hbar\omega}\left(\frac{1}{\varepsilon-\hbar\omega}\right)\frac{1}{e^{(\hbar\omega-\mu_K)/k_\mathrm{B}T_K}+1}\\ &\quad + 2\pi\mathrm{i}\sum_{n=0}^{\infty}\mathrm{Res}_{\varepsilon=\mu_K+(2n+1)\pi\mathrm{i}k_\mathrm{B}T_K}\left(\frac{1}{e^{(\varepsilon-\mu_K)/k_\mathrm{B}T_K}+1}\right)\\ &\qquad\cdot\frac{1}{\mu_K+(2n+1)\pi\mathrm{i}k_\mathrm{B}T_K-\hbar\omega}\\ &\quad - \int_\gamma \mathrm{d}\varepsilon\frac{1}{e^{(\varepsilon-\mu_K)/k_\mathrm{B}T_K}+1}\cdot\frac{1}{\varepsilon-\hbar\omega}.\end{aligned} \tag{B.1}$$

Now, let us calculate this expression term by term.

We start by evaluating the third term in Eq. (B.1), which we still need to integrate. First, we parametrize the integration contour as $(\varepsilon-\hbar\omega) =: Re^{\mathrm{i}\varphi}$ with $R\to\infty$ and $\mathrm{d}\varepsilon/(\varepsilon-\hbar\omega) = \mathrm{i}\cdot\mathrm{d}\varphi$, leading to

$$\int_\gamma \mathrm{d}\varepsilon\frac{1}{e^{(\varepsilon-\mu_K)/k_\mathrm{B}T_K}+1}\cdot\frac{1}{\varepsilon-\hbar\omega} = \mathrm{i}\lim_{R\to\infty}\int_0^\pi \mathrm{d}\varphi\frac{1}{e^{(Re^{\mathrm{i}\varphi}-\mu_K)/k_\mathrm{B}T_K}+1}.$$

In the next step, we take the $\lim_{R\to\infty}$ into the integral and note that

$$\begin{aligned}\lim_{R\to\infty}\frac{1}{e^{(Re^{\mathrm{i}\varphi}-\mu_K)/k_\mathrm{B}T_K}+1} &= \lim_{R\to\infty}\frac{1}{e^{R\cos(\varphi)/k_\mathrm{B}T_K}e^{R\mathrm{i}\sin(\varphi)/k_\mathrm{B}T_K}e^{-\mu_K/k_\mathrm{B}T_K}+1}\\ &\qquad\qquad\left|\lim_{R\to\infty}e^{R\cos(\varphi)/k_\mathrm{B}T_K} = \begin{cases}\infty, & 0\le\varphi<\pi/2\\ 0, & \pi/2<\varphi\le\pi\end{cases}\right.\\ &= \begin{cases}0, & 0\le\varphi<\pi/2\\ 1, & \pi/2<\varphi\le\pi\end{cases}\\ &= \Theta\left(\varphi-\frac{\pi}{2}\right).\end{aligned}$$

With this, the remaining integral is trivially solved, and we get

$$\int_\gamma \mathrm{d}\varepsilon\frac{1}{e^{(\varepsilon-\mu_K)/k_\mathrm{B}T_K}+1}\cdot\frac{1}{\varepsilon-\hbar\omega} = \mathrm{i}\int_0^\pi \mathrm{d}\varphi\,\Theta\left(\varphi-\frac{\pi}{2}\right) = \frac{\pi\mathrm{i}}{2}. \tag{B.2}$$

Next, we take care of the residue terms. In the first term, we find

$$\pi\mathrm{i}\,\mathrm{Res}_{\varepsilon=\hbar\omega}\left(\frac{1}{\varepsilon-\hbar\omega}\right)\frac{1}{e^{(\hbar\omega-\mu_K)/k_\mathrm{B}T_K}+1} = \pi\mathrm{i}\cdot\frac{1}{e^{(\hbar\omega-\mu_K)/k_\mathrm{B}T_K}+1}. \tag{B.3}$$

For later simplification, we rewrite the Fermi function as a hyperbolic tangent as follows,

$$\begin{aligned}\frac{1}{e^z+1} &= \frac{1}{2}\cdot\left(\frac{2}{e^z+1}-1+1\right) = \frac{1}{2}\cdot\left(\frac{2-e^z-1}{e^z+1}+1\right)\\ &= \frac{1}{2}\cdot\left(\frac{1-e^z}{e^z+1}+1\right) = \frac{1}{2}\cdot\left(\frac{e^{-z/2}-e^{z/2}}{e^{z/2}+e^{-z/2}}+1\right)\\ &= \frac{1}{2}\cdot\left(1-\frac{e^{z/2}-e^{-z/2}}{e^{z/2}+e^{-z/2}}\right) = \frac{1}{2}\cdot\left(1-\frac{\sinh(z/2)}{\cosh(z/2)}\right)\\ &= \frac{1}{2}\cdot\left(1-\tanh(z/2)\right)\end{aligned}$$

Using Eq. (6.3.12) from [56], which reads

$$\frac{1}{2}\tanh(z/2) = \frac{1}{\pi}\,\mathrm{Im}\left\{\psi_0\left(\frac{1}{2}+\frac{\mathrm{i}z}{2\pi}\right)\right\}, \tag{B.4}$$

we can rewrite the Fermi function further as the imaginary part of the Digamma function $\psi_0(z)$, which is defined as the logarithmic derivative of the Gamma function, that is $\psi_0(z) = \frac{\mathrm{d}}{\mathrm{d}z}\ln\Gamma(z)$. Taken together, we find

$$\pi\mathrm{i}\,\mathrm{Res}_{\varepsilon=\hbar\omega}\left(\frac{1}{\varepsilon-\hbar\omega}\right)\frac{1}{e^{(\hbar\omega-\mu_K)/k_\mathrm{B}T_K}+1} = \frac{\pi\mathrm{i}}{2} - \mathrm{i}\,\mathrm{Im}\left\{\psi_0\left(\frac{1}{2}+\mathrm{i}\frac{\hbar\omega-\mu_K}{2\pi k_\mathrm{B}T_K}\right)\right\}. \tag{B.5}$$

Lastly, we calculate the Fermi function's residues from Eq. (B.1). We find that

$$\mathrm{Res}_{\varepsilon=\mu_K+(2n+1)\pi\mathrm{i}k_\mathrm{B}T_K}\left(\frac{1}{e^{(\varepsilon-\mu_K)/k_\mathrm{B}T_K}+1}\right) = -k_\mathrm{B}T_K, \quad \forall n.$$

Simplifying the remaining fraction, we end up with

$$\begin{aligned}
&2\pi\mathrm{i}\sum_{n=0}^{\infty}\mathrm{Res}_{\varepsilon=\mu_K+(2n+1)\pi\mathrm{i}k_\mathrm{B}T_K}\left(\frac{1}{e^{(\varepsilon-\mu_K)/k_\mathrm{B}T_K}+1}\right)\cdot\frac{1}{\mu_K+(2n+1)\pi\mathrm{i}k_\mathrm{B}T_K-\hbar\omega}\\
&= -\sum_{n=0}^{\infty}\frac{2\pi\mathrm{i}k_\mathrm{B}T_K}{\mu_K+(2n+1)\pi\mathrm{i}k_\mathrm{B}T_K-\hbar\omega} = -\sum_{n=0}^{\infty}\frac{1}{n+\frac{1}{2}+\mathrm{i}\frac{\hbar\omega-\mu_K}{2\pi k_\mathrm{B}T_K}} \to \infty.
\end{aligned}$$

Looking at the last representation of this term, it becomes clear that it is a divergent harmonic series. To find out if we can regularize this divergence, we need to look back at the BMME in Eq. (2.30). $S_{ij}^{<}$ and $S_{ij}^{>}$, enter the BMME only through the Lamb shift Hamiltonian, defined in Eq. (2.29). Hence, they contribute only to the coherent part of the system's dynamics. However, this means that only the differences of the self-energies are relevant for the dynamics, since a constant *quasi-energy* offset in their values only affects the global phase of the system. We can therefore try to regularize the difference between two such divergences. Using the shorthand notation

$z := \frac{1}{2} + \mathrm{i}\frac{\hbar\omega - \mu_K}{2\pi k_\mathrm{B} T_K}$, we write

$$
\begin{aligned}
&-\sum_{n=0}^{\infty} \frac{1}{n+z_1} - \left(-\sum_{n=0}^{\infty} \frac{1}{n+z_2}\right) \\
&= \lim_{N\to\infty} \left(-\sum_{n=0}^{N} \frac{1}{n+z_1} + \sum_{n=0}^{N} \frac{1}{n+z_2}\right) \\
&= \lim_{N\to\infty} \sum_{n=0}^{N} \left(-\frac{1}{n+z_1} + \frac{1}{n+z_2}\right) \\
&= \lim_{N\to\infty} \sum_{n=1}^{N} \left(-\frac{1}{n+z_1-1} + \frac{1}{n+z_2-1}\right) \\
&= \lim_{N\to\infty} \sum_{n=1}^{N} \left(-\frac{1}{n+z_1-1} + \frac{1}{n+z_2-1} + \frac{1}{n} - \frac{1}{n}\right) \\
&= \lim_{N\to\infty} \left[\sum_{n=1}^{N} \left(\frac{1}{n} - \frac{1}{n+z_1-1}\right) - \sum_{n=1}^{N} \left(\frac{1}{n} - \frac{1}{n+z_2-1}\right)\right] \\
&= \sum_{n=1}^{\infty} \left(\frac{1}{n} - \frac{1}{n+z_1-1}\right) - \sum_{n=1}^{\infty} \left(\frac{1}{n} - \frac{1}{n+z_2-1}\right) \\
&= \left[\sum_{n=1}^{\infty} \left(\frac{1}{n} - \frac{1}{n+z_1-1}\right) - \gamma\right] - \left[\sum_{n=1}^{\infty} \left(\frac{1}{n} - \frac{1}{n+z_2-1}\right) - \gamma\right] \\
&= \psi_0(z_1) - \psi_0(z_2),
\end{aligned}
$$

where γ is the *Euler-Mascheroni* constant, and we have used Eq. (6.3.16) from [56] in the last row. From this calculation, we find that the difference of two such divergent series is indeed finite and can be represented by the difference of two Digamma functions $\psi_0(z)$. In this sense, we can state that the divergent series is regularized by the digamma function,

$$
-\sum_{n=0}^{\infty} \frac{1}{n + \frac{1}{2} + \mathrm{i}\frac{\hbar\omega - \mu_K}{2\pi k_\mathrm{B} T_K}} \overset{\text{reg.}}{=} \psi_0\left(\frac{1}{2} + \mathrm{i}\frac{\hbar\omega - \mu_K}{2\pi k_\mathrm{B} T_K}\right). \tag{B.6}
$$

Now, we combine the three terms from Eqs. (B.2), (B.5) and (B.6) to obtain the final result,

$$
\begin{aligned}
\text{p.v.} \int_{-\infty}^{\infty} \mathrm{d}\varepsilon\, \frac{f^K(\varepsilon)}{\varepsilon - \hbar\omega} &= \overbrace{\frac{\pi\mathrm{i}}{2} - \mathrm{i}\,\mathrm{Im}\left\{\psi_0\left(\frac{1}{2} + \mathrm{i}\frac{\hbar\omega - \mu_K}{2\pi k_\mathrm{B} T_K}\right)\right\}}^{\text{Eq. (B.5)}} + \overbrace{\psi_0\left(\frac{1}{2} + \mathrm{i}\frac{\hbar\omega - \mu_K}{2\pi k_\mathrm{B} T_K}\right)}^{\text{Eq. (B.6)}} - \overbrace{\frac{\pi\mathrm{i}}{2}}^{\text{Eq. (B.2)}} \\
&= \mathrm{Re}\left\{\psi_0\left(\frac{1}{2} + \mathrm{i}\frac{\hbar\omega - \mu_K}{2\pi k_\mathrm{B} T_K}\right)\right\}.
\end{aligned}
$$

With this principal value integral, we get the following result for $S_{ij}^{<}$ and $S_{ij}^{>}$ in the wideband limit,

$$
S_{ij}^{<}(\omega) = S_{ij}^{>}(\omega) = \sum_K \frac{\Gamma_{ij}^K}{2\pi}\, \mathrm{Re}\left\{\psi_0\left(\frac{1}{2} + \mathrm{i}\frac{\hbar\omega - \mu_K}{2\pi k_\mathrm{B} T_K}\right)\right\}.
$$

Appendix C

Electric current

In this appendix, we evaluate the time derivative of the fermionic number operator of the system, $\frac{\mathrm{d}}{\mathrm{d}t}\langle N_\mathrm{S}\rangle_t$, which is required to find a system-internal representation of the current from the left and right electrodes, $\langle I_\mathrm{L}\rangle_t$ and $\langle I_\mathrm{R}\rangle_t$. Since $N_\mathrm{S} = \sum_i n_i = \sum_i d_i^\dagger d_i$ acts solely on the system Hilbert space, we find its expectation value directly from $\rho_\mathrm{S}(t)$,

$$\frac{\mathrm{d}}{\mathrm{d}t}\langle N_\mathrm{S}\rangle_t = \mathrm{tr}_\mathrm{S}\left\{N_\mathrm{S}\dot{\rho}_\mathrm{S}(t)\right\},$$

The following derivation turns out to be easier if we use Eq. (2.17) for $\dot{\rho}_\mathrm{S}(t)$ instead of the final BMME from Eq. (2.30), and apply the secular approximation explicitly again,

$$\begin{aligned}\frac{\mathrm{d}}{\mathrm{d}t}\langle N_\mathrm{S}\rangle_t = -\frac{1}{\hbar}\sum_{ij\sigma}\int_0^\infty \frac{\mathrm{d}\tau}{\hbar}\,\mathrm{tr}_\mathrm{S}\Big\{N_\mathrm{S}(t)\Big(&G_{ij}^{\bar{\sigma}\sigma}(\tau)d_i^\sigma(t)d_j^{\bar{\sigma}}(t-\tau)\rho_\mathrm{S,I}(t)\\ &- G_{ji}^{\sigma\bar{\sigma}}(-\tau)d_i^\sigma(t)\rho_\mathrm{S,I}(t)d_j^{\bar{\sigma}}(t-\tau)\\ &- G_{ij}^{\bar{\sigma}\sigma}(\tau)d_j^{\bar{\sigma}}(t-\tau)\rho_\mathrm{S,I}(t)d_i^\sigma(t)\\ &+ G_{ji}^{\sigma\bar{\sigma}}(-\tau)\rho_\mathrm{S,I}(t)d_j^{\bar{\sigma}}(t-\tau)d_i^\sigma(t)\Big)\Big\}.\end{aligned}$$

To simplify this expression, we write out the number operator $N_\mathrm{S}(t) = \sum_k n_k(t)$, which is now time-dependent because we switched to the interaction picture,

$$\begin{aligned}\frac{\mathrm{d}}{\mathrm{d}t}\langle N_\mathrm{S}\rangle_t = -\frac{1}{\hbar}\sum_{ijk\sigma}\int_0^\infty \frac{\mathrm{d}\tau}{\hbar}\,\mathrm{tr}_\mathrm{S}\Big\{&G_{ij}^{\bar{\sigma}\sigma}(\tau)n_k(t)d_i^\sigma(t)d_j^{\bar{\sigma}}(t-\tau)\rho_\mathrm{S,I}(t)\\ &- G_{ji}^{\sigma\bar{\sigma}}(-\tau)n_k(t)d_i^\sigma(t)\rho_\mathrm{S,I}(t)d_j^{\bar{\sigma}}(t-\tau)\\ &- G_{ij}^{\bar{\sigma}\sigma}(\tau)n_k(t)d_j^{\bar{\sigma}}(t-\tau)\rho_\mathrm{S,I}(t)d_i^\sigma(t)\\ &+ G_{ji}^{\sigma\bar{\sigma}}(-\tau)n_k(t)\rho_\mathrm{S,I}(t)d_j^{\bar{\sigma}}(t-\tau)d_i^\sigma(t)\Big\}.\end{aligned}$$

Using the cyclic property of the trace and the fact that $[n_k(t), d_i^{(\dagger)}(t)] = 0$ for $i \neq k$, we find that all terms with $i \neq k$ vanish, and the sum over k disappears,

$$\begin{aligned}\frac{\mathrm{d}}{\mathrm{d}t}\langle N_\mathrm{S}\rangle_t = -\frac{1}{\hbar}\sum_{ij\sigma}\int_0^\infty \frac{\mathrm{d}\tau}{\hbar}\,\mathrm{tr}_\mathrm{S}\Big\{&G_{ij}^{\bar{\sigma}\sigma}(\tau)n_i(t)d_i^\sigma(t)d_j^{\bar{\sigma}}(t-\tau)\rho_\mathrm{S,I}(t)\\ &- G_{ji}^{\sigma\bar{\sigma}}(-\tau)n_i(t)d_i^\sigma(t)\rho_\mathrm{S,I}(t)d_j^{\bar{\sigma}}(t-\tau)\\ &- G_{ij}^{\bar{\sigma}\sigma}(\tau)n_i(t)d_j^{\bar{\sigma}}(t-\tau)\rho_\mathrm{S,I}(t)d_i^\sigma(t)\\ &+ G_{ji}^{\sigma\bar{\sigma}}(-\tau)n_i(t)\rho_\mathrm{S,I}(t)d_j^{\bar{\sigma}}(t-\tau)d_i^\sigma(t)\Big\}.\end{aligned}$$

Furthermore, because $n_i(t)d_i^\sigma(t) = d_i^\dagger(t)\cdot\delta_{\sigma\dagger}$ and $d_i^\sigma(t)n_i(t) = d_i(t)\cdot\delta_{\sigma-}$, we also remove the sum over σ,

$$\begin{aligned}\frac{\mathrm{d}}{\mathrm{d}t}\langle N_\mathrm{S}\rangle_t = -\frac{1}{\hbar}\sum_{ij}\int_0^\infty \frac{\mathrm{d}\tau}{\hbar}\,\mathrm{tr}_\mathrm{S}\Big\{ & G_{ij}^{>}(\tau)d_i^\dagger(t)d_j(t-\tau)\rho_{\mathrm{S,I}}(t) \\ & - G_{ji}^{<}(-\tau)d_i^\dagger(t)\rho_{\mathrm{S,I}}(t)d_j(t-\tau) \\ & - G_{ij}^{<}(\tau)d_j^\dagger(t-\tau)\rho_{\mathrm{S,I}}(t)d_i(t) \\ & + G_{ji}^{>}(-\tau)\rho_{\mathrm{S,I}}(t)d_j^\dagger(t-\tau)d_i(t)\Big\},\end{aligned}$$

where we used $G_{ij}^{\dagger -}(\tau) = G_{ij}^{<}(\tau)$ and $G_{ij}^{-\dagger}(\tau) = G_{ij}^{>}(\tau)$ from Eq. (2.24). In the next step, we insert the frequency expansion from Eq. (2.18) for the creation and annihilation operators,

$$\begin{aligned}\frac{\mathrm{d}}{\mathrm{d}t}\langle N_\mathrm{S}\rangle_t = -\frac{1}{\hbar}\sum_{ij}\sum_{\omega\omega'}e^{-\mathrm{i}(\omega+\omega')t}\int_0^\infty \frac{\mathrm{d}\tau}{\hbar}e^{\mathrm{i}\omega'\tau}\,\mathrm{tr}_\mathrm{S}\Big\{ & G_{ij}^{>}(\tau)d_i^\dagger(\omega)d_j(\omega')\rho_{\mathrm{S,I}}(t) \\ & - G_{ji}^{<}(-\tau)d_i^\dagger(\omega)\rho_{\mathrm{S,I}}(t)d_j(\omega') \\ & - G_{ij}^{<}(\tau)d_j^\dagger(\omega')\rho_{\mathrm{S,I}}(t)d_i(\omega) \\ & + G_{ji}^{>}(-\tau)\rho_{\mathrm{S,I}}(t)d_j^\dagger(\omega')d_i(\omega)\Big\},\end{aligned}$$

and apply the rotating-wave approximation,

$$\begin{aligned}\frac{\mathrm{d}}{\mathrm{d}t}\langle N_\mathrm{S}\rangle_t = -\frac{1}{\hbar}\sum_{ij}\sum_{\omega}\int_0^\infty \frac{\mathrm{d}\tau}{\hbar}e^{-\mathrm{i}\omega\tau}\,\mathrm{tr}_\mathrm{S}\Big\{ & G_{ij}^{>}(\tau)d_i^\dagger(\omega)d_j(-\omega)\rho_{\mathrm{S,I}}(t) \\ & - G_{ji}^{<}(-\tau)d_i^\dagger(\omega)\rho_{\mathrm{S,I}}(t)d_j(-\omega) \\ & - G_{ij}^{<}(\tau)d_j^\dagger(-\omega)\rho_{\mathrm{S,I}}(t)d_i(\omega) \\ & + G_{ji}^{>}(-\tau)\rho_{\mathrm{S,I}}(t)d_j^\dagger(-\omega)d_i(\omega)\Big\}.\end{aligned}$$

By virtue of $d_j^{\bar\sigma}(-\omega) = [d_i^\sigma(\omega)]^\dagger$, we get

$$\begin{aligned}\frac{\mathrm{d}}{\mathrm{d}t}\langle N_\mathrm{S}\rangle_t = -\frac{1}{\hbar}\sum_{ij\omega}\mathrm{tr}_\mathrm{S}\Big\{ & \Big[d_i(\omega_k)\Big]^\dagger d_j(\omega_k)\rho_{\mathrm{S,I}}(t)\Big[\tilde G_{ij}^{>}(\omega)\Big]^* \\ & - \Big[d_i(\omega_k)\Big]^\dagger \rho_{\mathrm{S,I}}(t)d_j(\omega_k)\Big[\tilde G_{ij}^{<}(\omega)\Big]^* \\ & - \Big[d_j(\omega_k)\Big]^\dagger \rho_{\mathrm{S,I}}(t)d_i(\omega_k)\tilde G_{ij}^{<}(\omega) \\ & + \rho_{\mathrm{S,I}}(t)\Big[d_j(\omega_k)\Big]^\dagger d_i(\omega_k)\tilde G_{ij}^{>}(\omega)\Big\}.\end{aligned}$$

To write this in a more compact form, we exchange the indices i and j in the first two terms and group similar terms together using the cyclic property of the trace again,

$$\begin{aligned}\frac{\mathrm{d}}{\mathrm{d}t}\langle N_\mathrm{S}\rangle_t = \frac{1}{\hbar}\sum_{ij\omega}\mathrm{tr}_\mathrm{S}\Big\{ & d_i(\omega)\Big[d_j(\omega)\Big]^\dagger\rho_{\mathrm{S,I}}(t)\Big(\tilde G_{ij}^{<}(\omega) + \Big[\tilde G_{ji}^{<}(\omega)\Big]^*\Big) \\ & - \Big[d_j(\omega)\Big]^\dagger d_i(\omega)\rho_{\mathrm{S,I}}(t)\Big(\tilde G_{ij}^{>}(\omega) + \Big[\tilde G_{ji}^{>}(\omega)\Big]^*\Big)\Big\}.\end{aligned}$$

At this point, we translate the equation back into the Schrödinger picture. In doing so, we obtain an additional coherent term $-\frac{1}{\hbar}\,\mathrm{tr_S}\left\{N_\mathrm{S}\,[H_\mathrm{S},\rho_\mathrm{S}(t)]\right\}$, which vanishes, as a short calculation shows. Furthermore, we rewrite the sums of the one-sided Fourier-transformed correlation functions according to Eqs. (2.27) and (2.28),

$$\begin{aligned}\frac{\mathrm{d}}{\mathrm{d}t}\langle N_\mathrm{S}\rangle_t = \frac{1}{\hbar}\sum_{ij\omega}\mathrm{tr_S}\Big\{&d_i(\omega)\Big[d_j(\omega)\Big]^\dagger\rho_\mathrm{S}(t)\gamma_{ij}^<(\omega)\\ &-\Big[d_j(\omega)\Big]^\dagger d_i(\omega)\rho_\mathrm{S}(t)\gamma_{ij}^>(\omega)\Big\}.\end{aligned}$$

This is precisely Eq. (2.39). For the final result for the electric currents, $\langle I_\mathrm{L}\rangle_t$ and $\langle I_\mathrm{R}\rangle_t$, see Eq. (2.42) in Sec. 2.2.3.

Appendix D

Bath relaxation time

In this appendix, we determine the typical time scale, $\tau_{\mathrm{relax},K}$, on which the electrode K relaxes to its local equilibrium state after an interaction with the nanosystem. In other words, we seek to find the time scale on which the correlations functions, $G_{ij}^{\lessgtr}(\tau)$, defined in Eq. (2.24), decay to zero. From Eqs. (A.1) and (A.3) in Appendix A, we find the functional forms of $G_{ij}^{\lessgtr}$ for our model in the general case, that is, without applying the wideband limit. To obtain $G_{ij}^{\lessgtr}$ in the wideband limit, we start from their Fourier transforms in the wideband limit, given as $\gamma_{ij}^{\lessgtr}(\omega)$ in Eqs. (2.32) and (2.33), and apply the inverse Fourier transform,

$$G_{ij}^{<}(\tau) = \frac{\hbar}{2\pi}\int_{-\infty}^{\infty} \mathrm{d}\omega\, \gamma_{ij}^{<}(\omega)\, e^{\mathrm{i}\omega\tau},$$
$$G_{ji}^{>}(-\tau) = \frac{\hbar}{2\pi}\int_{-\infty}^{\infty} \mathrm{d}\omega\, \gamma_{ij}^{>}(\omega)\, e^{\mathrm{i}\omega\tau}.$$

Inserting Eq. (2.32) in the expression for $G_{ij}^{<}$, we get

$$G_{ij}^{<}(\tau) = \frac{\hbar}{2\pi}\sum_K \Gamma_{ij}^K \int_{-\infty}^{\infty} \mathrm{d}\omega\, f^K(\hbar\omega)\, e^{\mathrm{i}\omega\tau}.$$

To calculate this integral, we close the integration contour by adding and subtracting the integral over a contour that encircles the upper half of the complex plane at $R \to \infty$ if $\tau > 0$, or which encircles the lower half of the complex plane if $\tau < 0$, respectively,

$$\left(\int_{-\infty}^{\infty} \mathrm{d}\omega + \int_{\gamma} \mathrm{d}\omega - \int_{\gamma} \mathrm{d}\omega\right) f^K(\hbar\omega)\, e^{\mathrm{i}\omega\tau} = \left(\oint \mathrm{d}\omega - \int_{\gamma} \mathrm{d}\omega\right) f^K(\hbar\omega)\, e^{\mathrm{i}\omega\tau}.$$

It is easy to see that the additional integration contours at $R \to \infty$ vanish because $e^{\mathrm{i}\omega\tau} \to 0$ as $\mathrm{Im}\{\omega\} \to \infty$ if $\tau > 0$, and $e^{\mathrm{i}\omega\tau} \to 0$ as $\mathrm{Im}\{\omega\} \to -\infty$ if $\tau < 0$. So we are left with a closed integration path that encircles the upper half of the complex plane in mathematically positive direction if $\tau > 0$, or which encircles the lower half of the complex plane in mathematically negative direction if $\tau < 0$,

$$\int_{-\infty}^{\infty} \mathrm{d}\omega\, f^K(\hbar\omega)\, e^{\mathrm{i}\omega\tau} = \begin{cases} \oint \mathrm{d}\omega\, f^K(\hbar\omega)\, e^{\mathrm{i}\omega\tau} & \tau > 0, \\ \oint \mathrm{d}\omega\, f^K(\hbar\omega)\, e^{\mathrm{i}\omega\tau} & \tau < 0. \end{cases}$$

We evaluate the closed contour integral using the residue theorem similar to Appendix B. The Fermi function $f^K(\hbar\omega)$ has simple poles at $\hbar\omega_n = \mu_K + (2n+1)\pi \mathrm{i} k_\mathrm{B} T_K$, where those for $n \geq 0$ lie in the upper half of the complex plane, and those with $n < 0$ in the lower half. The complex exponential function, $e^{\mathrm{i}\omega\tau}$, has no relevant poles. Thus, we get

$$\int_{-\infty}^{\infty} \mathrm{d}\omega\, f^K(\hbar\omega)\, e^{\mathrm{i}\omega\tau} = 2\pi\mathrm{i} \begin{cases} \sum\limits_{n=0}^{\infty} \mathrm{Res}_{\omega=\omega_n}\left(f^K(\hbar\omega)\right) \cdot e^{\mathrm{i}\tau\omega_n} & \tau > 0, \\ -\sum\limits_{n=-1}^{-\infty} \mathrm{Res}_{\omega=\omega_n}\left(f^K(\hbar\omega)\right) \cdot e^{\mathrm{i}\tau\omega_n} & \tau < 0. \end{cases}$$

As mentioned in Appendix B, the residues of the Fermi function evaluate to $-k_\mathrm{B}T_K$ for all n. With this, we find

$$\int_{-\infty}^{\infty} \mathrm{d}\omega\, f^K(\hbar\omega)\, e^{\mathrm{i}\omega\tau} = -2\pi\mathrm{i} k_\mathrm{B} T_K \,\mathrm{sgn}(\tau) \sum_{n\in 2\mathbb{N}+1} e^{\mathrm{i}|\tau|\mu_K/\hbar} e^{-|\tau|n\pi k_\mathrm{B} T_K/\hbar},$$

where the sum goes over all odd numbers, $n \in 2\mathbb{N}+1$. Now, for the typical time scale, on which this resulting expression decays for $|\tau| \to \infty$, only the smallest frequency, for $n = 1$, is relevant,

$$\int_{-\infty}^{\infty} \mathrm{d}\omega\, f^K(\hbar\omega)\, e^{\mathrm{i}\omega\tau} \overset{|\tau|\to\infty}{\sim} e^{-|\tau|\pi k_\mathrm{B} T_K/\hbar}.$$

In total, we find for $G_{ij}^<$ in the wideband limit,

$$G_{ij}^<(\tau) \overset{|\tau|\to\infty}{\sim} \sum_K e^{-|\tau|\pi k_\mathrm{B} T_K/\hbar} = \sum_K e^{-|\tau|/\tau_{\mathrm{relax},K}},$$

where we defined the relaxation time scale,

$$\tau_{\mathrm{relax},K} = \frac{\hbar}{\pi k_\mathrm{B} T_K}. \tag{D.1}$$

For $G_{ji}^>$, the calculation is similar and leads to the same decay behavior in the wideband limit,

$$G_{ji}^>(-\tau) \overset{|\tau|\to\infty}{\sim} \sum_K e^{-|\tau|\pi k_\mathrm{B} T_K/\hbar} = \sum_K e^{-|\tau|/\tau_{\mathrm{relax},K}}.$$

Appendix E

Steady state of the Anderson impurity model

In this section, we give the expression for the steady-state solution of the diagonal elements, $\rho_{ii} := \langle i|\rho_{\mathrm{S}}(t)|i\rangle$, for the Anderson impurity model. By requiring $\dot{\rho}_{ii} = 0$ in Eq. (2.44) and solving the resulting linear system of equations, we find

$$
\begin{aligned}
\rho_{00}^{\mathrm{ss}} &= \frac{1}{Z}\Big[\Big(\gamma^{<}(\varepsilon_\uparrow + U) + \gamma^{>}(\varepsilon_\downarrow)\Big)\,\gamma^{>}(\varepsilon_\uparrow)\,\gamma^{>}(\varepsilon_\downarrow + U) \\
&\quad + \Big(\gamma^{<}(\varepsilon_\downarrow + U) + \gamma^{>}(\varepsilon_\uparrow)\Big)\,\gamma^{>}(\varepsilon_\downarrow)\,\gamma^{>}(\varepsilon_\uparrow + U)\Big], \\
\rho_{\uparrow\uparrow}^{\mathrm{ss}} &= \frac{1}{Z}\Big[\gamma^{<}(\varepsilon_\downarrow)\,\gamma^{<}(\varepsilon_\uparrow + U)\,\gamma^{>}(\varepsilon_\downarrow + U) + \gamma^{<}(\varepsilon_\uparrow)\,\gamma^{>}(\varepsilon_\downarrow)\,\gamma^{>}(\varepsilon_\uparrow + U) \\
&\quad + \Big(\gamma^{<}(\varepsilon_\uparrow + U) + \gamma^{>}(\varepsilon_\downarrow)\Big)\,\gamma^{<}(\varepsilon_\uparrow)\,\gamma^{>}(\varepsilon_\downarrow + U)\Big], \\
\rho_{\downarrow\downarrow}^{\mathrm{ss}} &= \frac{1}{Z}\Big[\gamma^{<}(\varepsilon_\uparrow)\,\gamma^{<}(\varepsilon_\downarrow + U)\,\gamma^{>}(\varepsilon_\uparrow + U) + \gamma^{<}(\varepsilon_\downarrow)\,\gamma^{>}(\varepsilon_\uparrow)\,\gamma^{>}(\varepsilon_\downarrow + U) \\
&\quad + \Big(\gamma^{<}(\varepsilon_\downarrow + U) + \gamma^{>}(\varepsilon_\uparrow)\Big)\,\gamma^{<}(\varepsilon_\downarrow)\,\gamma^{>}(\varepsilon_\uparrow + U)\Big], \\
\rho_{\uparrow\downarrow\uparrow\downarrow}^{\mathrm{ss}} &= \frac{1}{Z}\Big[\Big(\gamma^{<}(\varepsilon_\uparrow + U) + \gamma^{>}(\varepsilon_\downarrow)\Big)\,\gamma^{<}(\varepsilon_\uparrow)\,\gamma^{<}(\varepsilon_\downarrow + U) \\
&\quad + \Big(\gamma^{<}(\varepsilon_\downarrow + U) + \gamma^{>}(\varepsilon_\uparrow)\Big)\,\gamma^{<}(\varepsilon_\downarrow)\,\gamma^{<}(\varepsilon_\uparrow + U)\Big], \\
Z &= \gamma^{<}(\varepsilon_\uparrow)\Big[\gamma^{>}(\varepsilon_\downarrow)\Big(\gamma^{<}(\varepsilon_\downarrow + U) + \gamma^{>}(\varepsilon_\downarrow + U) + \gamma^{>}(\varepsilon_\uparrow + U)\Big) \\
&\qquad + \gamma^{<}(\varepsilon_\uparrow + U)\Big(\gamma^{<}(\varepsilon_\downarrow + U) + \gamma^{>}(\varepsilon_\downarrow + U)\Big) + \gamma^{<}(\varepsilon_\downarrow + U)\,\gamma^{>}(\varepsilon_\uparrow + U)\Big] \\
&\quad + \gamma^{<}(\varepsilon_\downarrow)\Big[\gamma^{>}(\varepsilon_\uparrow)\Big(\gamma^{<}(\varepsilon_\uparrow + U) + \gamma^{>}(\varepsilon_\uparrow + U) + \gamma^{>}(\varepsilon_\downarrow + U)\Big) \\
&\qquad + \gamma^{<}(\varepsilon_\downarrow + U)\Big(\gamma^{<}(\varepsilon_\uparrow + U) + \gamma^{>}(\varepsilon_\uparrow + U)\Big) + \gamma^{<}(\varepsilon_\uparrow + U)\,\gamma^{>}(\varepsilon_\downarrow + U)\Big] \\
&\quad + \gamma^{>}(\varepsilon_\uparrow)\,\gamma^{>}(\varepsilon_\downarrow + U)\Big(\gamma^{<}(\varepsilon_\uparrow + U) + \gamma^{>}(\varepsilon_\downarrow)\Big) \\
&\quad + \gamma^{>}(\varepsilon_\downarrow)\,\gamma^{>}(\varepsilon_\uparrow + U)\Big(\gamma^{<}(\varepsilon_\downarrow + U) + \gamma^{>}(\varepsilon_\uparrow)\Big).
\end{aligned}
\tag{E.1}
$$

For the simplest case, $\varepsilon_\uparrow = \varepsilon_\downarrow =: \varepsilon$, this solution collapses to

$$\begin{aligned}
\rho^{\mathrm{ss}}_{00} &= \frac{1}{Z'}\gamma^{>}(\varepsilon)\,\gamma^{>}(\varepsilon+U),\\
\rho^{\mathrm{ss}}_{\uparrow\uparrow} &= \frac{1}{Z'}\gamma^{<}(\varepsilon)\,\gamma^{>}(\varepsilon+U) = \rho^{\mathrm{ss}}_{\downarrow\downarrow},\\
\rho^{\mathrm{ss}}_{\Updownarrow\Updownarrow} &= \frac{1}{Z'}\gamma^{<}(\varepsilon)\,\gamma^{<}(\varepsilon+U),\\
Z' &= \gamma^{<}(\varepsilon)\,\gamma^{<}(\varepsilon+U) + 2\,\gamma^{<}(\varepsilon)\,\gamma^{>}(\varepsilon+U) + \gamma^{>}(\varepsilon)\,\gamma^{>}(\varepsilon+U).
\end{aligned}$$

Bibliography

[1] *Sieg der Mikrosekunde*, Der Spiegel (1965).

[2] D. Langford and C. Morgan, *Facts and Fallacies: A Book of Definitive Mistakes and Misguided Predictions*, New edition (Corgi, London, 1982).

[3] E. A. Weiss, *Information Sougth on 'Only a Few Computers are Needed' Statement*, Communications of the ACM **28**, 1 (1985).

[4] G. E. Moore, *Cramming more components onto integrated circuits, Reprinted from Electronics, volume 38, number 8, April 19, 1965, pp.114 ff.* IEEE Solid-State Circuits Society Newsletter **11**, 33 (2006).

[5] G. E. Moore, *Progress in digital integrated electronics [Technical literaiture, Copyright 1975 IEEE. Reprinted, with permission. Technical Digest. International Electron Devices Meeting, IEEE, 1975, pp. 11-13.]* IEEE Solid-State Circuits Society Newsletter **11**, 36 (2006).

[6] M. M. Waldrop, *The chips are down for Moore's law*, Nature **530**, 144 (2016).

[7] A. von Hippel, *Molecular Engineering*, Science **123**, 315 (1956).

[8] A. Aviram and M. A. Ratner, *Molecular rectifiers*, Chemical Physics Letters **29**, 277 (1974).

[9] R. M. Metzger et al., *Unimolecular Electrical Rectification in Hexadecylquinolinium Tricyanoquinodimethanide*, Journal of the American Chemical Society **119**, 10455 (1997).

[10] S. Roth et al., *Molecular rectifiers and transistors based on π-conjugated materials*, Synthetic Metals **94**, 105 (1998).

[11] D. Xiang, X. Wang, C. Jia, T. Lee, and X. Guo, *Molecular-Scale Electronics: From Concept to Function*, Chemical Reviews **116**, 4318 (2016).

[12] B. C. Stipe, M. A. Rezaei, and W. Ho, *Single-Molecule Vibrational Spectroscopy and Microscopy*, Science **280**, 1732 (1998).

[13] M. A. Reed, C. Zhou, C. J. Muller, T. P. Burgin, and J. M. Tour, *Conductance of a Molecular Junction*, Science **278**, 252 (1997).

[14] T. Yelin et al., *Atomically Wired Molecular Junctions: Connecting a Single Organic Molecule by Chains of Metal Atoms*, Nano Letters **13**, 1956 (2013).

[15] J. M. Krans, C. J. Muller, I. K. Yanson, T. C. M. Govaert, R. Hesper, and J. M. van Ruitenbeek, *One-atom point contacts*, Physical Review B **48**, 14721 (1993).

[16] A. I. Yanson, G. R. Bollinger, H. E. van den Brom, N. Agraït, and J. M. van Ruitenbeek, *Formation and manipulation of a metallic wire of single gold atoms*, Nature **395**, 783 (1998).

[17] H. Ohnishi, Y. Kondo, and K. Takayanagi, *Quantized conductance through individual rows of suspended gold atoms*, Nature **395**, 780 (1998).

[18] C. Benesch, M. F. Rode, M. Čížek, R. Härtle, O. Rubio-Pons, M. Thoss, and A. L. Sobolewski, *Switching the Conductance of a Single Molecule by Photoinduced Hydrogen Transfer*, The Journal of Physical Chemistry C **113**, 10315 (2009).

[19] C. Hofmeister, P. B. Coto, and M. Thoss, *Controlling the conductance of molecular junctions using proton transfer reactions: A theoretical model study*, The Journal of Chemical Physics **146**, 092317 (2017).

[20] R. Härtle and M. Thoss, *Resonant electron transport in single-molecule junctions: Vibrational excitation, rectification, negative differential resistance, and local cooling*, Physical Review B **83**, 115414 (2011).

[21] R. Gupta, J. A. Fereiro, A. Bayat, A. Pritam, M. Zharnikov, and P. C. Mondal, *Nanoscale molecular rectifiers*, Nature Reviews Chemistry **7**, 106 (2023).

[22] S. A. Wolf, A. Y. Chtchelkanova, and D. M. Treger, *Spintronics—A retrospective and perspective*, IBM Journal of Research and Development **50**, 101 (2006).

[23] G. Guillaud, J. Simon, and J. P. Germain, *Metallophthalocyanines: Gas sensors, resistors and field effect transistors*, Coordination Chemistry Reviews **178-180**, 1433 (1998).

[24] C. W. Fuller et al., *Molecular electronics sensors on a scalable semiconductor chip: A platform for single-molecule measurement of binding kinetics and enzyme activity*, Proceedings of the National Academy of Sciences **119**, e2112812119 (2022).

[25] T. N. Todorov, *Local heating in ballistic atomic-scale contacts*, Philosophical Magazine B **77**, 965 (1998).

[26] J.-T. Lü, M. Brandbyge, and P. Hedegård, *Blowing the Fuse: Berry's Phase and Runaway Vibrations in Molecular Conductors*, Nano Letters **10**, 1657 (2010).

[27] S. L. Rudge, Y. Ke, and M. Thoss, *Current-induced forces in nanosystems: A hierarchical equations of motion approach*, Physical Review B **107**, 115416 (2023).

[28] M. Thoss and F. Evers, *Perspective: Theory of quantum transport in molecular junctions*, The Journal of Chemical Physics **148**, 030901 (2018).

[29] T. Frederiksen, M. Paulsson, M. Brandbyge, and A.-P. Jauho, *Inelastic transport theory from first principles: Methodology and application to nanoscale devices*, Physical Review B **75**, 205413 (2007).

[30] W. Dou and J. E. Subotnik, *A many-body states picture of electronic friction: The case of multiple orbitals and multiple electronic states*, The Journal of Chemical Physics **145**, 054102 (2016).

[31] H.-P. Breuer and F. Petruccione, *The Theory of Open Quantum Systems* (Oxford University Press, 2007).

[32] Y. Tanimura and R. Kubo, *Time Evolution of a Quantum System in Contact with a Nearly Gaussian-Markoffian Noise Bath*, Journal of the Physical Society of Japan **58**, 101 (1989).

[33] C. Schinabeck, A. Erpenbeck, R. Härtle, and M. Thoss, *Hierarchical quantum master equation approach to electronic-vibrational coupling in nonequilibrium transport through nanosystems*, Physical Review B **94**, 201407 (2016).

[34] A. P. Horsfield, D. R. Bowler, and A. J. Fisher, *Open-boundary Ehrenfest molecular dynamics: towards a model of current induced heating in nanowires*, Journal of Physics: Condensed Matter **16**, L65 (2004).

[35] A. Erpenbeck, C. Schinabeck, U. Peskin, and M. Thoss, *Current-induced bond rupture in single-molecule junctions*, Physical Review B **97**, 235452 (2018).

[36] W. Dou, A. Nitzan, and J. E. Subotnik, *Frictional effects near a metal surface*, The Journal of Chemical Physics **143**, 054103 (2015).

[37] R. Kapral and G. Ciccotti, *Mixed quantum-classical dynamics*, The Journal of Chemical Physics **110**, 8919 (1999).

[38] M. Head-Gordon and J. C. Tully, *Molecular dynamics with electronic frictions*, The Journal of Chemical Physics **103**, 10137 (1995).

[39] W. Dou, G. Miao, and J. E. Subotnik, *Born-Oppenheimer Dynamics, Electronic Friction, and the Inclusion of Electron-Electron Interactions*, Physical Review Letters **119**, 046001 (2017).

[40] W. Dou and J. E. Subotnik, *Perspective: How to understand electronic friction*, The Journal of Chemical Physics **148**, 230901 (2018).

[41] T. Holstein, *Studies of polaron motion: Part I. The molecular-crystal model*, Annals of Physics **8**, 325 (1959).

[42] OpenClipart-Vectors, *Koffein Molekül Chemische Struktur - Kostenlose Vektorgrafik auf Pixabay*, `https://pixabay.com/de/vectors/koffein-molek%c3%bcl-chemische-struktur-148821/` (visited on 06/11/2023).

[43] C. Cohen-Tannoudji, B. Diu, and F. Laloe, *Quantum Mechanics, Volume I: Basic Concepts, Tools, and Applications*, 2nd ed. (Wiley-VCH, 2020).

[44] R. Dümcke and H. Spohn, *The proper form of the generator in the weak coupling limit*, Zeitschrift für Physik B Condensed Matter **34**, 419 (1979).

[45] M. Am-Shallem, A. Levy, I. Schaefer, and R. Kosloff, *Three approaches for representing Lindblad dynamics by a matrix-vector notation*, 2015, arXiv:`1510.08634 [quant-ph]`.

[46] *scipy.linalg.solve — SciPy v1.11.0 Manual*, `https://docs.scipy.org/doc/scipy/reference/generated/scipy.linalg.solve.html` (visited on 06/28/2023).

[47] *scipy.linalg.lstsq — SciPy v1.11.0 Manual*, `https://docs.scipy.org/doc/scipy/reference/generated/scipy.linalg.lstsq.html` (visited on 06/28/2023).

[48] E. Scheer and J. C. Cuevas, *Molecular Electronics: An Introduction to Theory and Experiment*, 2nd ed. (World Scientific Publishing Company, 2017).

[49] *CODATA Value: electron mass in u*, `https://physics.nist.gov/cgi-bin/cuu/Value?meu` (visited on 05/03/2023).

[50] H. Risken, *The Fokker-Planck Equation, Methods of Solution and Applications* (Springer, 1984).

[51] V. Balakrishnan, *Elements of Nonequilibrium Statistical Mechanics* (Springer, 2021).

[52] M. Sachs, B. Leimkuhler, and V. Danos, *Langevin Dynamics with Variable Coefficients and Nonconservative Forces: From Stationary States to Numerical Methods*, Entropy **19**, 647 (2017).

[53] I. Lang and Y. Firsov, *Kinetic Theory of Semiconductors with Low Mobility*, Soviet Journal of Experimental and Theoretical Physics **16**, 1301 (1963).

[54] J. Koch and F. von Oppen, *Franck-Condon Blockade and Giant Fano Factors in Transport through Single Molecules*, Physical Review Letters **94**, 206804 (2005).

[55] F. Chen, K. Miwa, and M. Galperin, *Electronic friction in interacting systems*, The Journal of Chemical Physics **150**, 174101 (2019).

[56] M. Abramowitz and I. A. Stegun, *Handbook of Mathematical Functions with Formulas, Graphs and Mathematical Tables*, Tenth Printing (United States Department of Commerce, National Bureau of Standards, 1972).

Eigenständigkeitserklärung

Erklärung gemäß der geltenden Prüfungsordnung:

Hiermit versichere ich, dass

1. ich die eingereichte Masterarbeit selbständig verfasst habe,
2. ich keine anderen als die angegebenen Quellen und Hilfsmittel benutzt und alle wörtlich oder sinngemäß aus anderen Werken übernommenen Inhalte als solche kenntlich gemacht habe, und
3. die eingereichte Masterarbeit weder vollständig noch in wesentlichen Teilen Gegenstand eines anderen Prüfungsverfahrens war oder ist.

Ort, Datum	Unterschrift